

REPORT DOCUMENTATION PAGE

Form Approved
OMB No. 0704-0188

Public reporting burden for this collection of information is estimated to average 1 hour per response, including the time for reviewing instructions, searching existing data sources, gathering and maintaining the data needed, and completing and reviewing the collection of information. Send comments regarding this burden estimate or any other aspect of this collection of information, including suggestions for reducing this burden, to Washington Headquarters Services, Directorate for Information Operations and Reports, 1215 Jefferson Davis Highway, Suite 1204 Arlington, VA 22202-4302 and to the Office of Management and Budget, Paperwork Reduction Project (0704-0188), Washington, DC 20503.

1. AGENCY USE ONLY (Leave blank)		2. REPORT DATE April 29, 1996	3. REPORT TYPE AND DATES COVERED Final Report : Mar 93-Mar 96
4. TITLE AND SUBTITLE Investigation of High-Temperature Eutectic-Based Microcomposites			5. FUNDING NUMBERS FQ8671-9500154 2306/AS
6. AUTHOR(S) B.P. Bewlay, H.A. Lipsitt, M.R. Jackson and J.A. Sutliff			
7. PERFORMING ORGANIZATION NAME(S) AND ADDRESS(ES) General Electric Company Corporate Research and Development Center Schenectady, NY 12301			AFOSR-TR-96 0360
9. SPONSORING / MONITORING AGENCY NAME(S) AND ADDRESS(ES) AFOSR/ 110 Duncan Avenue Suite B115 BOLLING AFB, DC 20332-0001			10. SPONSORING / MONITORING AGENCY REPORT NUMBER F49620-93-C-0007
11. SUPPLEMENTARY NOTES			
12a. DISTRIBUTION / AVAILABILITY STATEMENT APPROVED FOR PUBLIC RELEASE; DISTRIBUTION UNLIMITED			12b. DISTRIBUTION CODE 19960726 073
13. ABSTRACT (Maximum 200 words) The present report describes an investigation of high temperature directionally solidified eutectic-based microcomposites. The principal topics of the present report are the results of the investigations of the third year of this project. Details of earlier investigations have been described in the first and second year annual reports, and published in the open literature. This report describes the results in four areas. First, an advanced niobium-silicide based composite which shows an attractive balance of high and low temperature properties, such as fracture toughness, tensile strength, creep performance and oxidation behavior are described. The density-reduced stress rupture behavior of this composite showed an improvement over current generation advanced Ni-based superalloys. Second, recent studies of toughening mechanisms in composites generated from ternary Nb-Ti-Si alloys are described. Fracture toughness values of >20 MPa√m have been measured in as-DS composites. Third, the microtexture of the silicide and metallic phases in a ternary Nb-Ti-Si alloy composite have been investigated using the electron back scattering pattern technique for electron diffraction in the SEM. Microtexture measurements were performed to examine the relationship between texture and mechanical properties. Finally, the recent data relating to the ternary Nb-Ti-Si phase diagram is described.			
14. SUBJECT TERMS			15. NUMBER OF PAGES 54
			16. PRICE CODE
17. SECURITY CLASSIFICATION OF REPORT UNCLASSIFIED	18. SECURITY CLASSIFICATION OF THIS PAGE UNCLASSIFIED	19. SECURITY CLASSIFICATION OF ABSTRACT UNCLASSIFIED	20. LIMITATION OF ABSTRACT U

GENERAL INSTRUCTIONS FOR COMPLETING SF 298

The Report Documentation Page (RDP) is used in announcing and cataloging reports. It is important that this information be consistent with the rest of the report, particularly the cover and title page. Instructions for filling in each block of the form follow. It is important to *stay within the lines* to meet optical scanning requirements.

Block 1. Agency Use Only (Leave blank).

Block 2. Report Date. Full publication date including day, month, and year, if available (e.g. 1 Jan 88). Must cite at least the year.

Block 3. Type of Report and Dates Covered. State whether report is interim, final, etc. If applicable, enter inclusive report dates (e.g. 10 Jun 87 - 30 Jun 88).

Block 4. Title and Subtitle. A title is taken from the part of the report that provides the most meaningful and complete information. When a report is prepared in more than one volume, repeat the primary title, add volume number, and include subtitle for the specific volume. On classified documents enter the title classification in parentheses.

Block 5. Funding Numbers. To include contract and grant numbers; may include program element number(s), project number(s), task number(s), and work unit number(s). Use the following labels:

C - Contract	PR - Project
G - Grant	TA - Task
PE - Program Element	WU - Work Unit Accession No.

Block 6. Author(s). Name(s) of person(s) responsible for writing the report, performing the research, or credited with the content of the report. If editor or compiler, this should follow the name(s).

Block 7. Performing Organization Name(s) and Address(es). Self-explanatory.

Block 8. Performing Organization Report Number. Enter the unique alphanumeric report number(s) assigned by the organization performing the report.

Block 9. Sponsoring/Monitoring Agency Name(s) and Address(es). Self-explanatory.

Block 10. Sponsoring/Monitoring Agency Report Number. (If known)

Block 11. Supplementary Notes. Enter information not included elsewhere such as: Prepared in cooperation with...; Trans. of...; To be published in.... When a report is revised, include a statement whether the new report supersedes or supplements the older report.

Block 12a. Distribution/Availability Statement. Denotes public availability or limitations. Cite any availability to the public. Enter additional limitations or special markings in all capitals (e.g. NOFORN, REL, ITAR).

DOD - See DoDD 5230.24, "Distribution Statements on Technical Documents."

DOE - See authorities.

NASA - See Handbook NHB 2200.2.

NTIS - Leave blank.

Block 12b. Distribution Code.

DOD - Leave blank.

DOE - Enter DOE distribution categories from the Standard Distribution for Unclassified Scientific and Technical Reports.

NASA - Leave blank.

NTIS - Leave blank.

Block 13. Abstract. Include a brief (*Maximum 200 words*) factual summary of the most significant information contained in the report.

Block 14. Subject Terms. Keywords or phrases identifying major subjects in the report.

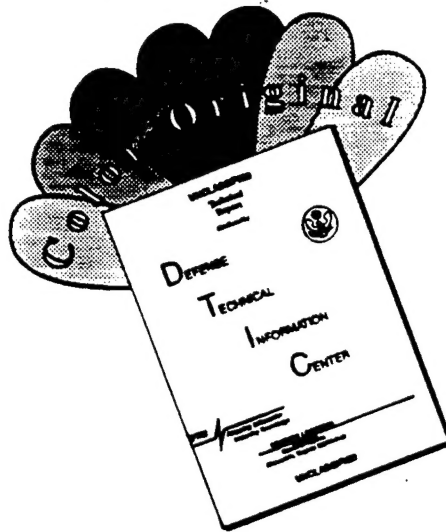
Block 15. Number of Pages. Enter the total number of pages.

Block 16. Price Code. Enter appropriate price code (*NTIS only*).

Blocks 17. - 19. Security Classifications. Self-explanatory. Enter U.S. Security Classification in accordance with U.S. Security Regulations (i.e., UNCLASSIFIED). If form contains classified information, stamp classification on the top and bottom of the page.

Block 20. Limitation of Abstract. This block must be completed to assign a limitation to the abstract. Enter either UL (unlimited) or SAR (same as report). An entry in this block is necessary if the abstract is to be limited. If blank, the abstract is assumed to be unlimited.

DISCLAIMER NOTICE



THIS DOCUMENT IS BEST QUALITY AVAILABLE. THE COPY FURNISHED TO DTIC CONTAINED A SIGNIFICANT NUMBER OF COLOR PAGES WHICH DO NOT REPRODUCE LEGIBLY ON BLACK AND WHITE MICROFICHE.

Contents

1.	Executive Summary	1
2.	Objectives	2
3.	Accomplishments and Progress	3
3.1	Investigations of the Balance of Mechanical and Environmental Properties of a Multi-Element Niobium-Niobium Silicide Based In-Situ Composite	3
3.1.1	Introduction	3
3.1.2	Experimental	
3.1.2.1	Directional Solidification	3
3.1.2.2	Mechanical Properties	3
3.1.2.3	Oxidation Testing	4
3.1.3	Results and Discussion	4
3.1.3.1	Microstructures and Phase Chemistries	4
3.1.3.2	Mechanical Properties	5
3.1.3.3	Oxidation Behavior	13
3.1.4	Summary	14
3.1.5	References for Section 3.1	14
3.2	Fracture Behavior of Ternary Alloy Nb-Ti-Si In Situ Composites	16
3.2.1	Introduction	16
3.2.2	Experimental	16
3.2.3	Results and Discussion	17
3.2.4	Conclusions	24
3.2.5	References for Section 3.2	25
3.3	Orientation Imaging of a Nb-33Ti-16Si DS In Situ Composite	26
3.3.1	Introduction	26
3.3.2	Results and Discussion	26
3.3.3	Conclusions	26
3.3.4	References for Section 3.3	26
3.4	Ternary Phase Equilibria in the Nb-Ti-Si Ternary System	29
3.4.1	Introduction	29
3.4.2	Background on Nb-Ti-Si Phase Equilibria	30
3.4.3	Experimental	30
3.4.4	Results and Discussion	32
3.4.5	Conclusions	45
3.4.6	References for Section 3.4	45
4.	Future Work	46
5.	Publications and Presentations	47
5.1	1996 Publications	47
5.2	1995 Publications	47
5.3	1994 Publications	48
5.4	Presentations	48
6.	Personnel Qualifications	49
6.1	Program Organization	49
6.2	Personnel Qualifications	49
7.	Acknowledgments	51

List of Figures

3.1.1	Micrographs of the longitudinal section of the DS Nb-24.7Ti-16Si-8.2Hf-2Cr-1.9Al composite (MASC)	5
3.1.2	Typical scanning electron micrographs of (a) the longitudinal, and (b) the transverse sections of a DS Nb-33Ti-16Si composite consisting of Nb(Ti,Si) and (Nb,Ti) ₃ Si	6
3.1.3	Microprobe scans perpendicular to the growth direction showing the Nb, Hf, Ti, and Si concentration profiles perpendicular to the dendrites	7
3.1.4	R-curve behavior of the DS MAS	7
3.1.5	Fracture surfaces of the Nb-Ti-Hf-Cr-Al-Si composite	8
3.1.6	Tensile strength of the Nb-Ti-Hf-Cr-Al-Si composite as a function of temperature showing the improvement of high-temperature strength over Laves phase-based composites with similar intermetallic volume fractions	9
3.1.7	Comparison of secondary creep rates of the complex DS silicide-based composite at 1100 °C with the compressive creep behavior of monolithic Nb ₅ Si ₃ and with Nb-Nb ₅ Si ₃ binary composites	9
3.1.8	Stress rupture behavior of the DS MASC is compared to that of second- and third-generation single crystal Ni-based superalloys [4] in Larson-Miller plots (C=20) where the temperature-time parameter is plotted against (a) rupture stress or (b) rupture stress/material density	11
3.1.9	Measurements of (a) room temperature elastic modulus and (b) linear thermal expansion from 23 °C to 1250 °C	12
3.1.10	Oxidation behavior of the DS MASC, together with other similar silicide-based composites with volume fractions of silicide in the range 30-70%	13
3.1.11	Material losses in oxidation of Nb-based Ti-modified silicide composites are comparable to less oxidation-resistant Ni-based superalloys, such as IN738	14
3.2.1	Schematic diagram of the projection of the liquidus surface of the metal-rich end of the Nb-Ti-Si ternary phase diagram	16
3.2.2	Typical microstructures (BSE images) of (a) the longitudinal section, and (b) the transverse section of a DS hypoeutectic Nb-33Ti-16Si Nb(Ti,Si)-(Nb,Ti) ₃ Si composite	18
3.2.3	Typical microstructures (BSE images) of (a) the longitudinal section of a DS hypereutectic Nb-27Ti-22Si composite, and (b) the transverse section of a DS hypereutectic Nb-21Ti-22Si composite	19
3.2.4	Fracture toughness of the ternary Nb-Ti-Si composites	20
3.2.5	R-curve behavior of a DS Nb-33Ti-20Si composites	21
3.2.6	Fracture surfaces of DS Nb-27Ti-12Si composite	22
3.2.7	Fracture surfaces of the DS Nb-40Ti-20Si composite	23
3.3.1	Scanning electron micrograph (BSE) of DS Nb-Ti-Si alloy, showing the sub-region analyzed using automated-EBSP	27
3.3.2	Orientation images for (a) the (Nb,Ti) phase and (b) the (Nb,Ti) ₃ Si phase	27
3.3.3	Macrotexture data as (a) Nb inverse pole figure of growth direction, (b) Nb {100} pole figure, and (c) (Nb,Ti) ₃ Si pole figure	28
3.4.1	Schematic diagram of the proposed Nb-Ti-Si ternary phase diagram for compositions between 0 and 37.5%Si	29
3.4.2	(a) Schematic diagram showing the projection of the liquidus surface for Option 1, (b) schematic diagram showing the projection of the liquidus surface for Option 1, and (c) actual compositions and constituent phases of the ternary phase diagram (the binary points are from previous studies)	31

3.4.3	Typical microstructures of the (a) longitudinal and (b) transverse sections of a DS Nb-27Ti-16Si alloy	34
3.4.4	Typical microstructures of the transverse section of a DS Nb-21Ti-12Si alloy	35
3.4.5	Typical microstructures of the transverse section of a DS Nb-44Ti-12Si alloy	35
3.4.6	Typical microstructures of the (a) longitudinal and (b) transverse sections of a DS Nb-27Ti-22Si alloy	37
3.4.6	(c) Microprobe scans perpendicular to the growth direction showing the Nb, Ti, and Si concentration profiles perpendicular to the dendrites	38
3.4.7	Typical microstructure of the induction melted Nb-32.5Ti-35Si alloy	39
3.4.8	Typical microstructure of the induction melted Nb-60Ti-30Si alloy	40
3.4.9	Typical microstructure of the transverse section of a DS Nb-75Ti-10Si alloy	41
3.4.10	Typical microstructures of the transverse section of a DS Nb-75Ti-20Si alloy, at low (a) and high (b) magnifications, showing the primary $\text{Ti}(\text{Nb})_5\text{Si}_3$ faceted dendrites, and inter-dendritic eutectic $(\text{Ti,Nb})\text{-Ti}(\text{Nb})_5\text{Si}_3$	42
3.4.11	Typical microstructure of the transverse section of a DS Nb-75Ti-15Si alloy	43
3.4.12	Typical microstructure of the transverse section of a DS Nb-70Ti-20Si alloy	44

List of Tables

3.1.1	Composition ranges observed in the individual phases of the DS MASC (atom %)	6
3.1.2	Tensile strength of the MASC as a function of temperature	9
3.1.3	Tensile creep data (rupture life, secondary creep rates, and strain to failure) of the MASC at 1000 and 1100 °C	10
3.2.1	Ternary alloy compositions together with DS composite volume fractions and dendrite arm diameters	17
3.2.2	Room temperature fracture toughness of DS ternary Nb-Ti-Si in-situ composites	20
3.2.3	The effect of test temperatures of -196 and 500 °C on the fracture toughness of DS ternary Nb-Ti-Si composites	24
3.4.1	Alloy compositions and constituent phases of the ternary Nb-Ti-Si alloys investigated	33
3.4.2	Microprobe analyses of (Nb,Ti) , $(\text{Nb,Ti})_3\text{Si}$, and $\text{Nb}(\text{Ti})_5\text{Si}_3$ phase composition ranges for the Nb-27Ti-22Si composite	38

1. Executive Summary

The present report describes an investigation of high-temperature directionally solidified (DS) eutectic-based microcomposites. The principal topics of the present report are the results of the investigations that have been conducted in the third year of this project. Details of earlier investigations have been described in the first and second year annual reports, and have been presented at conferences and published in the open literature.

This report describes the technical findings in four areas:

1. An advanced niobium-silicide based composite which shows an attractive balance of high- and low-temperature properties, such as fracture toughness, tensile strength, creep performance, and oxidation behavior.
2. Toughening mechanisms in composites generated from ternary Nb-Ti-Si alloys. The fracture behavior of these composites has been studied using monotonic loading experiments and R-curve measurements. Fracture toughness values of $>15 \text{ MPa}\sqrt{\text{m}}$ have been measured in as-DS composites.
3. Microtextures of the silicide and metallic phases of an in-situ composite generated from a ternary Nb-Ti-Si alloy, which has been investigated using the electron back scattering pattern (EBSP) technique for electron diffraction in the scanning electron microscope. Microtexture measurements were performed in order to investigate the relationship between texture and mechanical properties. These results will be reviewed.
4. The most recent data relating to the ternary Nb-Ti-Si phase diagram.

The composites that have been investigated consist of high-strength, Nb-based M_3Si and $\text{M}_5(\text{Si},\text{Al})_3$ silicides together with a modest-strength, high-toughness Nb-based metallic phase with a volume fraction of $\sim 50\%$. In the DS condition, the best of these composites can have a room-temperature fracture toughness of greater than $20 \text{ MPa}\sqrt{\text{m}}$, which is a substantial improvement over monolithic intermetallics. High-temperature tensile strength and creep behavior have also been examined in selected silicide-based composites; tensile strengths of $>350 \text{ MPa}$ at 1200°C and creep rupture lives of >500 hours at 1100°C (100 MPa) have been measured.

The creep rupture behavior of composites directionally solidified from the advanced Nb-Ti-Hf-Cr-Al-Si alloy that was investigated, is similar to that of an advanced-generation single-crystal Ni-based superalloy, CMSX10. After accounting for the reduced density of the composite in comparison with CMSX10, the density-reduced stress rupture behavior of this composite showed improvement of several Larson-Miller parameters over current-generation advanced Ni-based superalloys. In addition, creep data on binary Nb-16%Si composites in the DS condition have been investigated and indicate an order of magnitude reduction in the creep rate in comparison with the equivalent extruded material. The reduced creep rate in the DS composite could be caused by either a larger silicide grain size or a composite texture.

This project has been a collaborative effort by a team of researchers from General Electric Corporate Research and Development and Wright State University. The findings of these studies have been presented regularly at international conferences and published in the open literature, as detailed in Section 5 of this report.

2. Objectives

The principal objective of this research has been to investigate toughening mechanisms in high-strength directionally solidified microcomposites with melting temperatures between 1600 and 2100 °C. These composites consist of silicides, such as Nb₃Si and Nb₅Si₃, and are toughened by a Nb-based solid solution. Composites investigated have been directionally solidified from model binary Nb-Si, ternary Nb-Ti-Si alloys, and higher order alloys containing Nb, Si, Ti, Hf, Al, and

Cr. Although room-temperature toughness has been the principal topic of the present investigation, the ultimate application of this effort is in high-temperature materials, and for this reason only systems with melting temperature above 1600 °C have been studied. In those systems that have shown the most promising fracture toughness, high-temperature properties, such as tensile strength and creep behavior, have also been investigated.

3. Accomplishments and Progress

3.1 Investigations of the Balance of Mechanical and Environmental Properties of a Multi-Element Niobium-Niobium Silicide Based In-Situ Composite

3.1.1 Introduction

Nb-Si in-situ composites, which consist of a Nb-based solid solution with Nb₃Si and/or Nb₅Si₃ silicides, have been shown to have great potential as high-temperature structural materials because of their attractive balance of high- and low-temperature mechanical properties [1-9]. Unfortunately, the composites from binary Nb-Si alloys have very poor oxidation resistance, and generally, elements that are added to these composites to improve oxidation resistance compromise their high-temperature mechanical properties [4]. The present section describes an analogous in-situ composite generated from a more complex Nb-Ti-Hf-Si-Al-Cr alloy; this composite offers an improved balance of mechanical properties and oxidation resistance.

This composite consists of high-strength, high-melting-temperature Nb-based silicides together with a high-melting-temperature, modest-strength, high-toughness Nb-based metallic phase. The composition of the alloy that was directionally solidified to generate this composite was Nb-24.7Ti-8.2Hf-2.0Cr-1.9Al-16.0Si (all compositions are given in atom per cent). Throughout the present section this composite will be referred to as the metal and silicide composite (MASC). This composition was based on the binary Nb-16%Si composition [7-10]; Ti and Hf were added to improve the oxidation resistance [11]. Subramanian et al. [4] and Jackson et al. [11] reported that the oxidation resistances of both the single-phase silicide and metallic phases were improved by partial substitution of Ti for Nb. Cr and Al also improve the oxidation resistance of both the metallic and silicide phases [12]. Ti was also added to improve the intrinsic ductility of the metallic phase (and therefore potentially the composite toughness). Ti additions have the disadvantage of reducing the alloy melting temperature, and thus the strengths of these Ti-modified monolithic metals make them more suitable for sheet structures in engines, rather than for airfoils [11,12]. Hf is added because it is a strong solid solution strengthener of the Nb-based metallic phase [11]. All elements partition to varying degrees between the different phases of the composite [2], and this was taken into consideration in designing the alloy from which the present composite was derived.

The present section describes microstructures, phase chemistries, mechanical properties and oxidation behavior of the MASC. Creep rupture properties and oxidation data are compared with those of the most recent Ni-based superalloys. Those mechanical property measurements which are discussed include room temperature fracture toughness, R-curve measurements, tensile strength from room temperature to 1200 °C, and tensile creep data at 1100 °C. The thermal expansion and modulus of elasticity of the composite were also measured at temperatures from room temperature to 1200 °C.

3.1.2 Experimental

3.1.2.1 Directional Solidification

Alloys from which the in-situ composite samples were generated were prepared using high purity (99.99%) elements and were induction levitation melted in a segmented water-cooled copper crucible [10,13]. The melting temperature of the alloy from which the MASC was generated was 1760 °C, as measured using a 2-wavelength optical pyrometer which was calibrated against 99.9% pure Ti. Induction levitation melting and directional solidification were performed under an atmosphere of ultrahigh-purity argon in order to prevent contamination with interstitials. Samples (~10 mm diameter and ~75 mm long) were directionally solidified by the Czochralski method at constant rates of 5 mm/min. The process has been described in further detail elsewhere [10,13]. Conventional microscopy and electron beam microprobe analysis were performed to characterize phase chemistries.

3.1.2.2 Mechanical Properties

Fracture Toughness Measurements

Single-edge notched bending specimens (SENB) for fracture toughness measurements were prepared by electro-discharge machining (EDM) so that their longitudinal axis was parallel to the growth direction. The SENBs were then surface ground to the finished dimensions (nominally 33 mm × 6 mm × 3 mm) to remove the EDM re-cast layer. The bars were notched at their midpoints using a 50 µm wire and EDM.

Fracture toughness measurements were performed using monotonic loading and four point bending using a cross-head speed of $4.2 \times 10^{-3} \text{ mms}^{-1}$. The procedures provided by ASTM standard E-399 [14] were employed, the only point of deviation from ASTM E-399 being the omission of fatigue pre-cracking. For this reason, the toughness values for monotonic loading experiments are reported as K_{Ic} rather than K_{Ic} . R-curve measurements were also performed on additional samples following the ASTM standard E-561-94. [15]. R-Curve measurements were performed in four point bending, but with a slower cross-head speed of $2.5 \times 10^{-4} \text{ mm/s}$, in displacement control mode. The crack opening displacement (COD) was monitored using an Instron double cantilever beam type COD gage. After each loading increment, the crack length on the outside of the specimen was also measured when the crack was fully arrested using an optical microscope mounted on the cross-head.

Tensile and Creep Rupture Testing

Tensile testing was performed in a vacuum of $\sim 10^{-4}$ Torr using a 2 mm diameter gauge, a 10.7 mm long uniform diameter button-head tensile specimen, and an initial strain rate of $8 \times 10^{-4} \text{ s}^{-1}$. The tensile specimens were prepared by surface grinding of the as-DS samples so that the growth direction was parallel to the axis of the tensile bar. The improved toughness of the DS composite allowed centerless grinding of the tensile testing samples.

Modulus and Expansion Measurements

Dynamic elastic moduli were measured in air at room temperature and in an atmosphere of flowing argon at 100 °C temperature intervals up to 1200 °C. The samples were machined by first EDM'ing and then centerless grinding to final dimensions. The sample was machined so that the longitudinal axis was parallel to the growth direction, the sample being nominally 2.5 mm in diameter and 25 mm in length. Sample weights and dimensions were measured, and a transducer connecting rod of a Ni-W alloy was welded to the end of the sample. Longitudinal ultrasonic waves were passed from the connecting rod along the sample axis and were reflected at the far end of the sample. The modulus was calculated based on the velocity of the wave through the sample.

The thermal expansion behavior of the MASC from room temperature to 1250 °C was measured in a flowing argon atmosphere using a differential dilatometer.

This measurement was performed on a 25 mm long pin with a square cross section of 2.5 mm on a side. The sample was machined by first EDM'ing to the approximate dimensions and then centerless grinding to final dimensions, so that the longitudinal axis of the sample was parallel to the growth direction. A standard sample of high-purity alumina was run in tandem with the MASC sample, so that the axial expansion could be determined. The standard and the MASC were heated at a rate of 10 °C/min in the dilatometer capsule, which was inserted into a furnace with MoSi₂ heating elements. The standard and the sample lengths were measured at a sampling rate of several times per second, with the measurement and temperature recorded whenever the sample length changed from the previous measurement. Similar data were taken during cooling, but the constant cooling rate of 10 °C/minute could only be maintained to temperatures of about 800 °C, where forced cooling would be required to maintain the cooling rate. Only data determined on heating, and not cooling, are reported.

3.1.2.3 Oxidation Testing

Isothermal oxidation tests were performed at 1000, 1200, and 1400 °C, in a static air MoSi₂-resistance heated furnace. Periodic removal from the furnace (at 1, 2, 4, 25, 50, 100, 150, and 200 hours, or until the test was terminated because of visual observation of gross material loss) was performed to determine weight change per unit area. The samples were machined by first EDM'ing and then centerless grinding to final dimensions, so that the longitudinal axis was parallel to the growth direction, the sample being nominally 2.5 mm in diameter and 25 mm in length. Metallography was performed at the termination of testing to estimate by interpolation or extrapolation the approximate material loss after 100 hours of exposure.

3.1.3. Results and Discussion

3.1.3.1 Microstructures and Phase Chemistries

Figure 3.1.1 shows a typical scanning electron micrograph (backscatter electron (BSE) imaging) of a longitudinal section of the composite microstructure. It contained both metallic and M₃Si intermetallic dendrites, a small amount of an M₅Si₃ intermetallic, and an interdendritic eutectic of M₃Si intermetallic and metal (where M represents Nb, Ti, and Hf). In this regard it is entirely analogous to hypereutectic binary Nb-Si and ternary Nb-Ti-Si composites reported previously [16]. However, in the alloy design for the MASC, no M₅Si₃

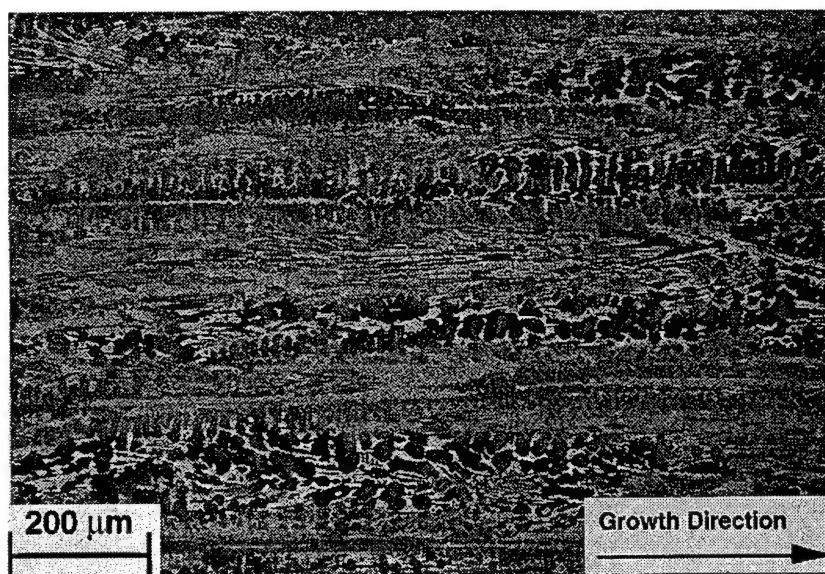


Figure 3.1.1. Micrographs of the longitudinal section of the DS Nb-24.7Ti-16Si-8.2Hf-2Cr-1.9Al composite (MASC).

was expected. A typical microstructure of a ternary composite is shown in Figure 3.1.2; it consists of interpenetrating dendrites of the composite phases, with dendrite cross-sections on the order of 5 to 50 μm wide. The M_3Si dendrites possessed the distinctive faceted morphology that has been reported previously in the binary hypereutectic binary Nb-Si alloys and the ternary Nb-Ti-Si composites [10,16]. However, in the case of the MASC, Hf segregation results in only small differences in the average atomic weight of the different phases, so it is difficult to obtain significant contrast between them using BSE imaging. The metallic and intermetallic dendrites of the MASC were aligned with the growth direction. The volume fraction of the metallic phase was 54%. The average dendrite size of the metallic phase, including the secondary arms, was $\sim 24 \mu\text{m}$.

Phase Chemistries

Electron microprobe analysis confirmed that the composite consisted of three phases:

- A metallic phase containing Nb, Ti, Hf, Si, Al and Cr
- An M_3Si silicide phase
- An $\text{M}_5(\text{Si},\text{Al})_3$ type phase

The composition ranges observed in the three phases are shown in Table 3.1.1. The Si concentrations of the M_3Si and M_5Si_3 silicides were close to the stoichiometric values.

Figure 3.1.3 shows a typical electron microprobe scan perpendicular to the composite growth direction. The

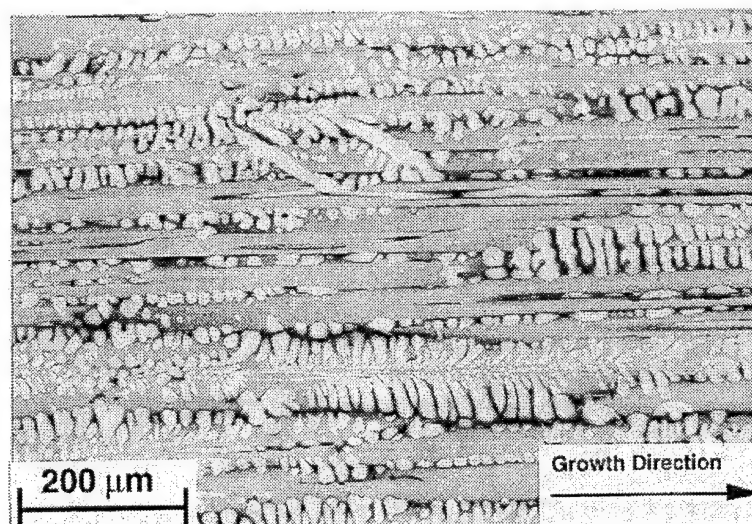
Ti concentration profile was approximately uniform across the dendrites perpendicular to the growth direction, but there was some reduction in the Ti concentration in the interdendritic regions. There was strong Hf segregation from the metallic phase to the $\text{M}_5(\text{Si},\text{Al})_3$ and M_3Si silicides. The Hf partitioning results observed were 5% Hf in the metallic phase, 8% Hf in M_3Si , and 12.5% Hf in $\text{M}_5(\text{Si},\text{Al})_3$. The bulk Hf composition in the alloy was nominally 8.2%. The Nb:Ti ratio was $\sim 2:1$ in the metallic phase. In the $\text{M}_5(\text{Si},\text{Al})_3$, the Nb:Ti:Hf:Si ratio was 2:2:1:3. Very low concentrations of Al and Cr were observed in both the M_3Si and $\text{M}_5(\text{Si},\text{Al})_3$ silicides.

3.1.3.2 Mechanical Properties

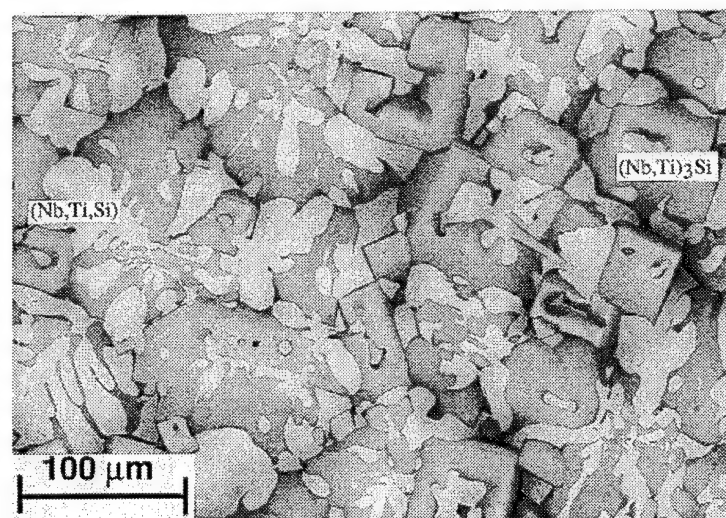
Fracture Toughness

Room-temperature fracture toughness values of K_{Ic} of 18.2-23.3 $\text{MPa}\sqrt{\text{m}}$ were measured for monotonic loading. Similar values of K_{Ic} were obtained from R-curve measurements. These are higher levels of fracture toughness than those reported previously in DS intermetallic-based composites. R-curve measurements are shown in Figure 3.1.4, together with lines of stress intensity versus crack length at constant load. Typically, the initiation toughness values for the MASC were 7 to 13 $\text{MPa}\sqrt{\text{m}}$, and the K_{Ic} values were 19-22 $\text{MPa}\sqrt{\text{m}}$. The variation in stress intensity for crack initiation may have been dependent upon the position of the notch tip with respect to the intermetallic or metallic phase.

Examination of the data after R-curve measurements indicates that the composite clearly exhibited R-curve



(a)



(b)

Figure 3.1.2. Typical scanning electron micrographs of (a) the longitudinal, and (b) the transverse sections of a DS Nb-33Ti-16Si composite consisting of Nb(Ti,Si) and (Nb,Ti)₃Si. The structure consists of non-faceted Nb(Ti,Si) dendrites, which is the lighter phase in these BSE micrographs, together with large-scale (~ 50 μm) faceted (Nb,Ti)₃Si dendrites.

Table 3.1.1. Composition ranges observed in the individual phases of the DS MASC (atom %).

Metal Solid Solution					
Nb	Ti	Hf	Si	Al	Cr
58–61	27.2–29.4	5.0–5.3	0.9–1.3	2.5–3.0	2.8–3.9
M ₃ Si Solid Solution					
Nb	Ti	Hf	Si	Al	Cr
48.3–49.0	18.2	7.8	24.7–25.4	0.1	0.13–0.16
M ₅ Si ₃ Solid Solution					
Nb	Ti	Hf	Si	Al	Cr
25.5–27.9	22.2–23.2	12.5–12.9	35.4–37.5	1.0–1.5	0.35–0.5

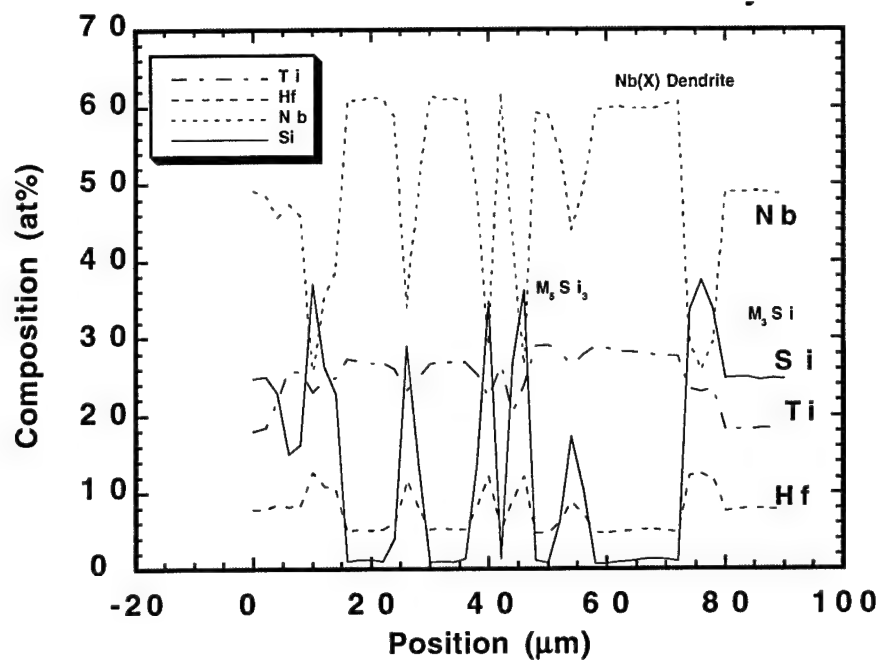


Figure 3.1.3. Microprobe scans perpendicular to the growth direction showing the Nb, Hf, Ti, and Si concentration profiles perpendicular to the dendrites.

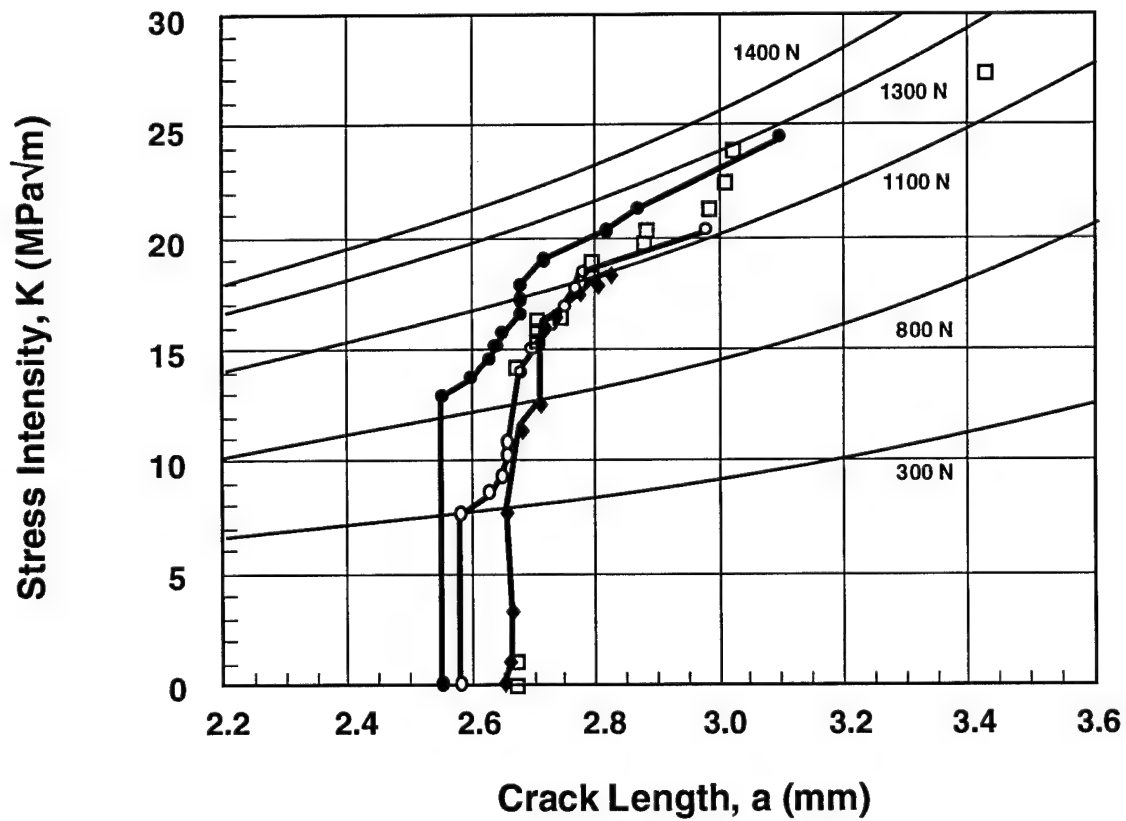
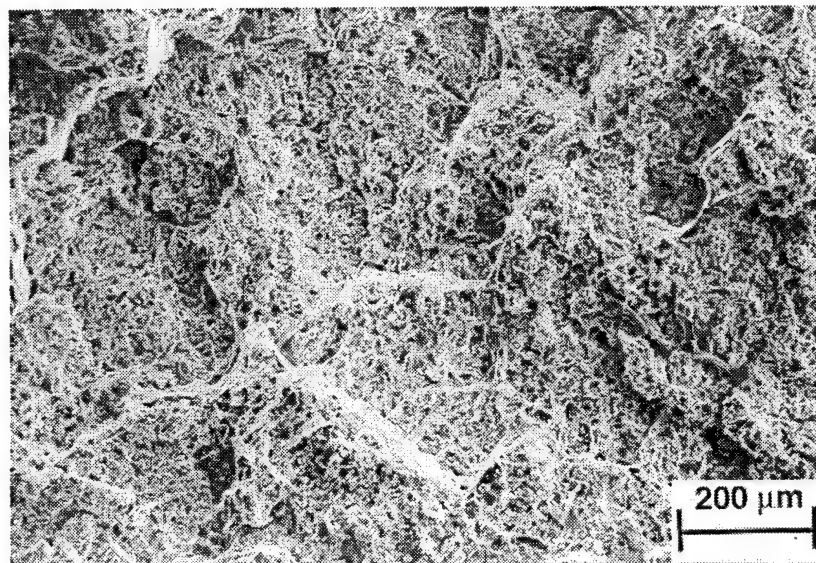


Figure 3.1.4. R-curve behavior of the DS MASC.

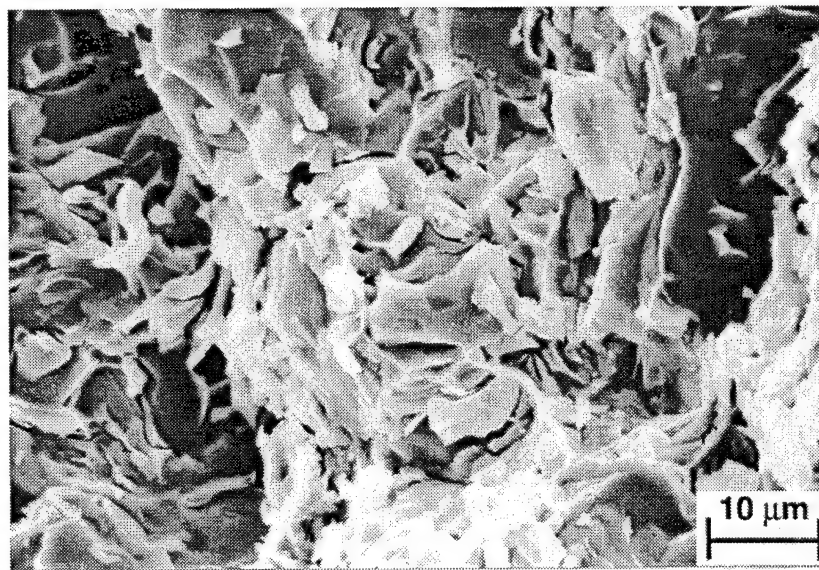
behavior, the resistance to crack growth increased with increasing crack length. The measured R-curves extend beyond the point of instability because the test was performed using displacement control rather than load control. These R-curve fracture toughness measurements were consistent with those from the monotonic loading experiments. These R-curves are similar to those reported previously in binary Nb-10%Si in-situ composites that have displayed a K_{IC} of $>20 \text{ MPa}\sqrt{\text{m}}$ in

the single and double extruded conditions [8].

Figure 3.1.5 shows fracture surfaces of the DS MASC. The fracture surfaces were similar for both monotonic loading experiments and R-curve measurements. The fracture surfaces were highly convoluted and consistent with a high work of fracture. The higher magnification fractograph shows that metallic dendrites failed in a ductile manner, and were pulled out of the matrix. The metallic phase between the silicide dendrites was



(a)



(b)

Figure 3.1.5. Fracture surfaces of the Nb-Ti-Hf-Cr-Al-Si composite.

also pulled to a chisel point, and microcracking of the silicide matrix was observed. All of the M_3Si and M_5Si_3 intermetallic dendrites failed by cleavage. This suggests that the majority of the toughness is provided by the metallic phase, although microcracking and interface debonding may also make significant toughening contributions.

The crack path was also examined in a partially fractured bar that was unloaded prior to unstable crack growth. Crack deflection and crack multiplication were evident. The fracture path shows distinct offsetting of the crack path and lateral crack propagation parallel to the directional solidification direction where the crack intersected the intermetallic dendrites. Thus, the intermetallic dendrites do play an important role in toughening the composite. At higher magnifications crack bridging and crack blunting were observed.

High-Temperature Strength

The composite tensile stress is shown as a function of temperature in Figure 3.1.6 and Table 3.1.2. The tensile fracture stress was ~ 750 MPa at room temperature and 370 MPa at 1200 °C. At 1200 °C the scatter in the yield stress was ~ 20 MPa. However, several hundred MPa scatter was observed in the room temperature fracture stress measurements; this is probably due to the flaw sensitivity of the fracture stress of this composite at room temperature. At 1200 °C an elongation of 19% was measured, indicating significant plastic deformation of both the metallic and silicide phases. Monolithic alloys of similar compositions to the metallic

phase of the composite have a yield strength of less than 55 MPa at 1200 °C [12]. Thus, the composite possesses substantially improved tensile properties. In comparison with monolithic intermetallics, the strength retention of this composite at elevated temperatures is very encouraging. At room temperature, the metallic phase provides the composite with improved toughness, whereas at elevated temperatures (>1000 °C) the silicide phases maintain its strength. The volume fraction of silicide in the above composite can be increased to improve the high-temperature strength and oxidation resistance, but this may compromise the attractive room-temperature toughness.

Density-normalized bending strength/temperature data have been reported previously for Nb-42.5Ti-15Si, Nb-40Ti-15Si-5Al [14], and binary Nb-10Si composites [6]. The binary Nb-10Si composite showed bending strength levels at 1200 °C, similar to the tensile strengths reported in Nb-Ti-Hf-Cr-Al-Si alloy compos-

Table 3.1.2. Tensile strength of the MASC as a function of temperature.

Temperature (°C)	Fracture Strength (MPa)
25	770
700	590
1000	429
1100	425
1200	370

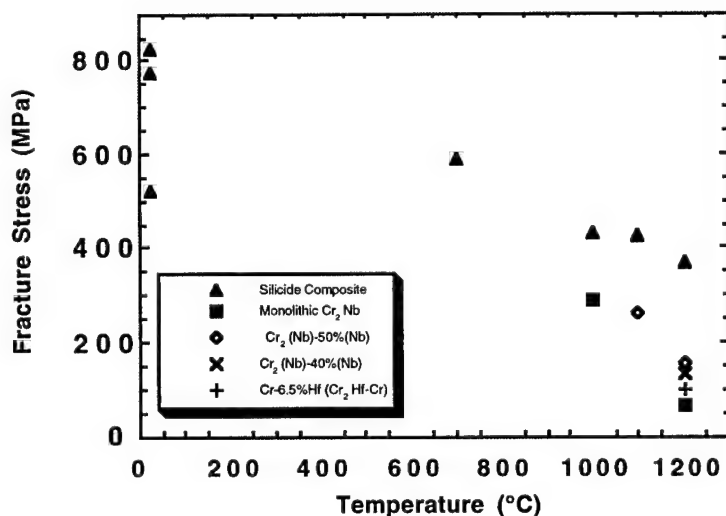


Figure 3.1.6. Tensile strength of the Nb-Ti-Hf-Cr-Al-Si composite as a function of temperature showing the improvement of high-temperature strength over Laves phase-based composites with similar intermetallic volume fractions.

ites (350 MPa) [6]. However, the reductions in the high-temperature strength levels displayed in ternary Nb-Ti-Si and quaternary Nb-Ti-Si-Al are not experienced by the MASC. This suggests that Hf additions can have a powerful effect on both high-temperature strength and oxidation resistance. Details of the strengthening mechanism are the subject of further research.

Creep Rupture Behavior

Figure 3.1.7 compares the secondary creep rates of the MASC with those of a range of high-temperature alloys, including Ni-base PWA1480, Mo TZM, and monolithic commercial Nb-based alloys (B-66 and C129Y). Tensile creep data of the MASC are shown in Table 3.1.3. The composite creep rates are more than an order of magnitude lower than those of B-66 and C129Y. The secondary

tensile creep rates at 1100 °C and 105 and 140 MPa are similar to the compressive creep rates measured in binary Nb-16%Si composites at 1200 °C [3, 17, 18]. The stress sensitivity of the creep rate in the MASC is substantially lower than for Mo TZM.

The creep rupture behavior of the Nb-Ti-Hf-Cr-Al-Si composite is shown in the Larson-Miller plot in Figure 3.1.8(a), and is compared to a current generation single crystal Ni-based superalloy, CMSX4, and an advanced generation single-crystal Ni-based superalloy, CMSX10 [2]. At 1100 °C and 105 MPa, the rupture life was greater than 500 hours. Stresses higher than 105 MPa led to shorter rupture times at either 1000 or 1100 °C. The stress rupture behavior is also shown in Figure 3.1.8(b), accounting for the reduced density of the composite in comparison with CMSX4 and

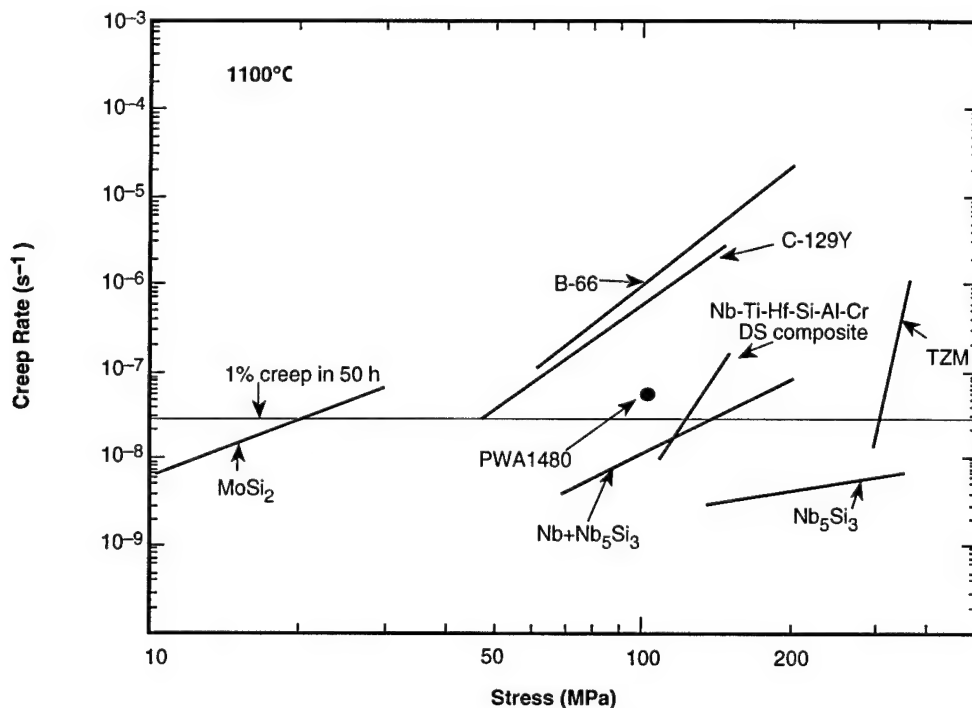


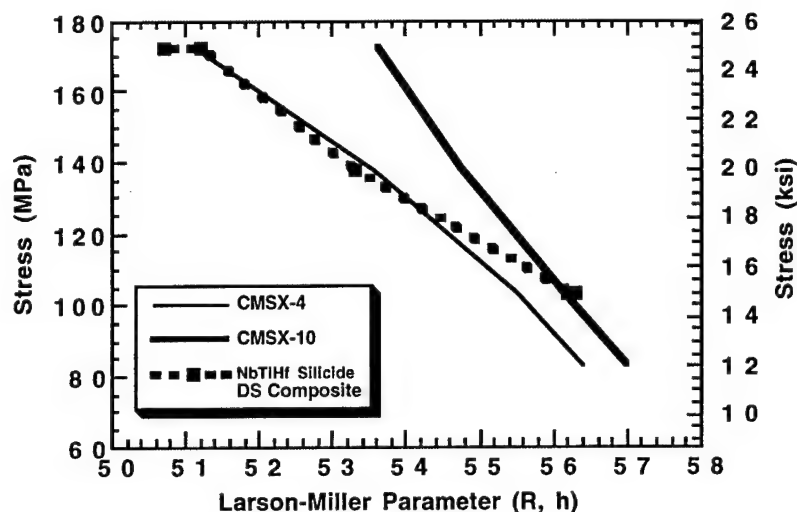
Figure 3.1.7. Comparison of secondary creep rates of the complex DS silicide-based composite at 1100 °C with the compressive creep behavior of monolithic Nb₅Si₃ and with Nb-Nb₅Si₃ binary composites [17]. Compressive creep behavior of several commercial high-temperature alloys is included. Creep to 1% strain in 50 hours is indicated by the horizontal line.

Table 3.1.3. Tensile creep data (rupture life, secondary creep rates, and strain to failure) of the MASC at 1000 and 1100 °C.

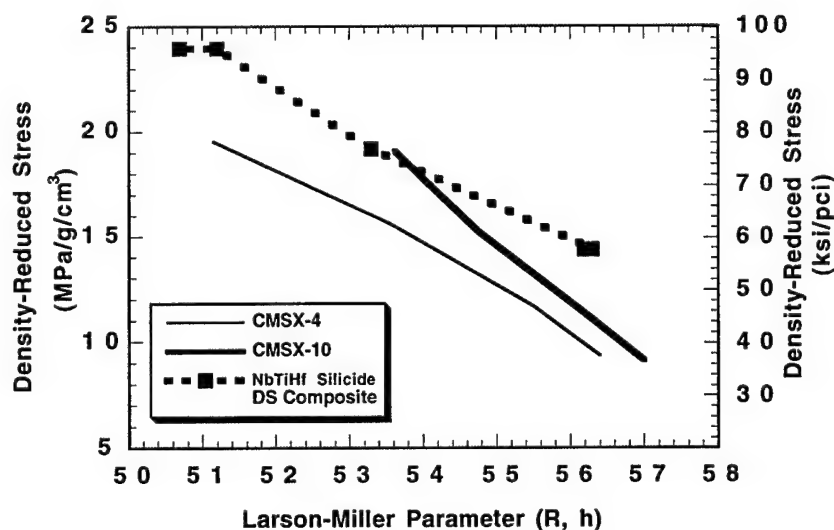
Temperature : Stress (°C) : (MPa)	Rupture Life (hours)	Creep Rate (s ⁻¹)	ε _f (%)
1100 : 140	35	1.7x10 ⁻⁷	7
1100 : 105	584, 524	9.3x10 ⁻⁹	9.1, 11
1000 : 175	129, 212	2.9x10 ⁻⁸	4.5, 6.0

CMSX10. Figure 3.1.8(b) illustrates the increase in specific rupture performance that results from the substantial reduction in density of the MASC compared to the third-generation single crystal superalloy. In summary, the stress rupture behavior of the MASC is similar to that of advanced single-crystal Ni-based superal-

loys under similar test conditions, and thus, after accounting for the lower density of the MASC, the creep behavior is very promising. In addition, to date only a small range of such composites has been evaluated. The rupture behavior that will be required for future applications will be well beyond any behavior observed



(a)



(b)

Figure 3.1.8. Stress rupture behavior of the DS MASC is compared to that of second- and third-generation single crystal Ni-based superalloys [4] in Larson-Miller plots ($C=20$) where the temperature-time parameter is plotted against (a) rupture stress or (b) rupture stress/material density. Stress rupture testing was performed in argon.

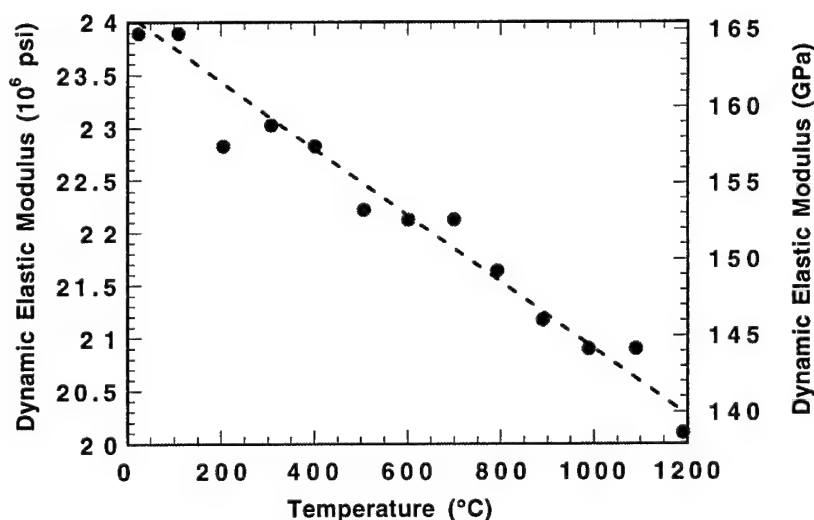
thus far. Current estimates are that ultimately an 80-fold increase over current rupture lives may be required for successful application of the intermetallic-based composites.

Physical Properties

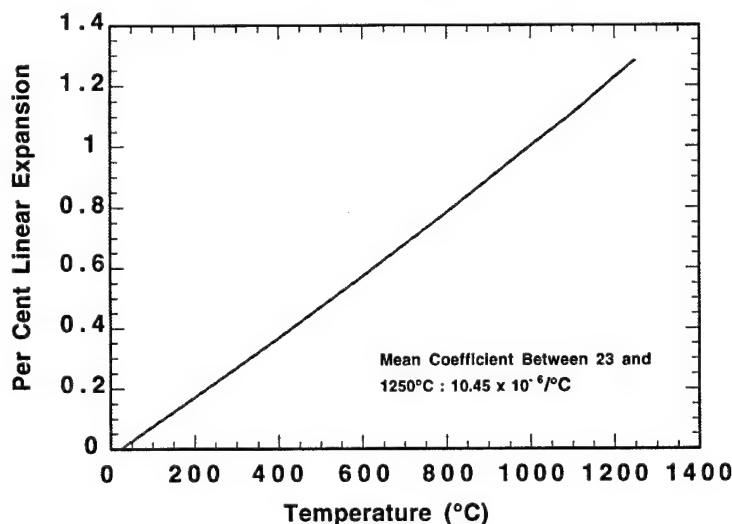
The modulus at room temperature was 165 GPa, and it decreased approximately linearly with increasing temperature to 140 GPa at 1200 °C, as shown in Figure 3.1.9(a). In comparison, monolithic Nb₅Si₃ has been reported to have a modulus of 170-210 GPa at room temperature. Thus, the modulus value of 140 GPa for the composite at 1200 °C is very promising. Typical

modulus values for a third-generation Ni-based superalloy at 1100 °C are 75-83 GPa in the <001> and 210 GPa in the <111>. The specific modulus of the composite at 1200 °C is probably greater than that of Ni-based superalloys, but the anisotropy of the composite modulus needs to be investigated in further detail.

The total expansion to 1250 °C is shown in Figure 3.1.9(b). The thermal expansion of the composite is approximately linear over this temperature range with a coefficient of $10.45 \times 10^{-6}/^{\circ}\text{C}$. Previously monolithic binary Nb₅Si₃ and ternary (Nb, Ti)₅Si₃ silicides were reported to have expansion coefficients of $\sim 9.0 \times 10^{-6}/^{\circ}\text{C}$ over this temperature range [11]. Typically, the ther-



(a)



(b)

Figure 3.1.9. Measurements of (a) room temperature elastic modulus and (b) linear thermal expansion from 23 °C to 1250 °C.

mal expansion of a monolithic alloy of a similar composition to the metal phase of this composite is $\sim 9.4 \times 10^{-6}/^{\circ}\text{C}$.

These results suggest that the expansion mismatch between the metal and the intermetallics over this temperature range is relatively small. Thus, it is expected that the thermal ratcheting between the phases will be negligible, and the interface between composite phases will not suffer excess stress during thermal cycling.

3.1.3.3 Oxidation Behavior

Oxidation behavior at 1000 and 1200 °C has been investigated for a number of Nb-based intermetallics and refractory metal intermetallic composites [2]. The oxidation behavior of the MASC at 1200 °C is shown in Figure 3.1.10. Subramanian, et al. [4] have reported similar oxidation performance for several ternary and quaternary silicide-based composites. The oxidation behavior of the MASC was also compared with the oxidation behavior of similar arc-cast silicides with volume fractions of metal ranging from 30 to 70%. On the basis of oxidation performance, increasing the silicide volume fraction to 70% is highly beneficial. Pack-siliciding of the DS material also leads to a further improvement in the oxidation behavior. These oxidation data at 1200 °C show a substantial improvement over that of binary Nb-Nb₅Si₃ composites [2], but the oxidation resistance of this composite requires further

improvement. No pesting-type behavior (oxidation resistance dependent on stress and the defect content of the test sample) was observed in any of these oxidation tests. At 1400 °C and above, oxidation is catastrophic.

A comparison of oxidation performance for the DS MASC and Ni-based superalloys is shown in Figure 3.1.11. The Laves refractory metal in-situ composites were better than the silicide MASC shown. The DS MASC shows material losses at rates intermediate between the rapid losses of an older superalloy like IN 738 and the improved oxidation behavior of third-generation single crystal superalloys. The horizontal dashed arrow in Figure 3.1.11 indicates the goal behavior for the present study, where component surface temperatures may be 1370 °C. This goal is derived from current superalloy capabilities. If superalloys can survive with surface temperatures of 1150 °C, then the rate of metal loss for the best superalloys at that temperature, $\sim 25 \mu\text{m}/100$ hours, is a reasonable goal for the refractory metal in-situ composites at their maximum surface temperature. Even if the goal of $<25 \mu\text{m}$ loss/100 h at 1370 °C is met, the refractory metal in-situ composites will need protective coatings, just as do today's superalloys.

3.1.4. Summary

The present study describes a very high-temperature refractory metal-silicide composite system which has

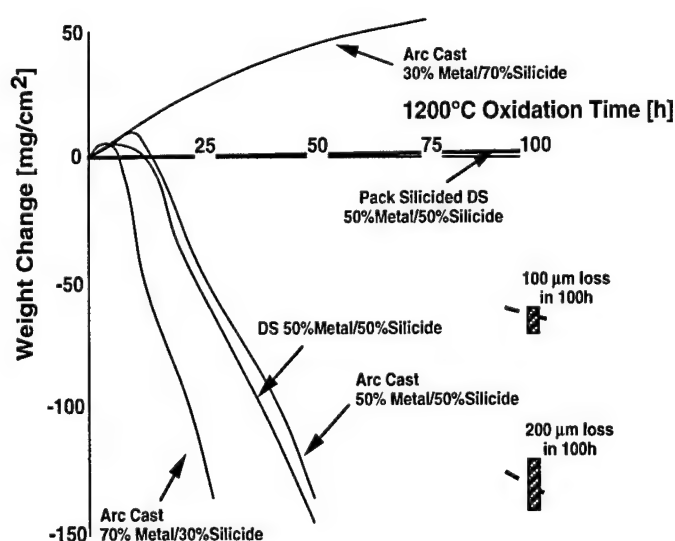


Figure 3.1.10. Oxidation behavior of the DS MASC, together with other similar silicide-based composites with volume fractions of silicide in the range 30-70%.

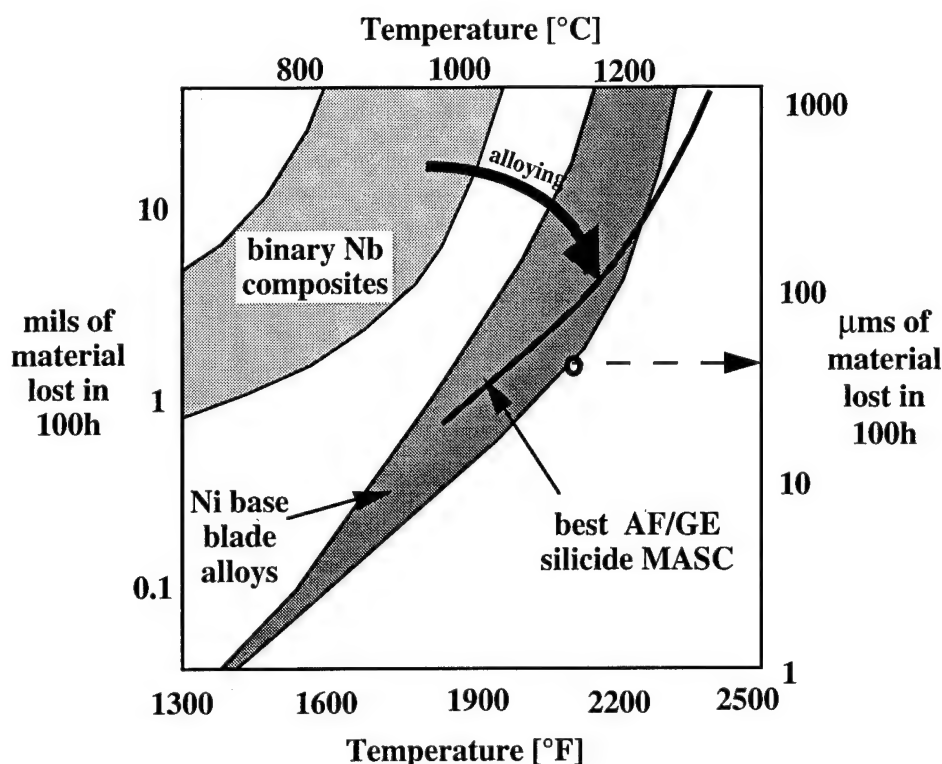


Figure 3.1.11 Material losses in oxidation of Nb-based Ti-modified silicide composites are comparable to less oxidation-resistant Ni-based superalloys, such as IN738.

improved high-temperature properties over the most advanced single crystal Ni-base alloys. This composite combines high-strength, low-toughness silicides with a lower-strength, high-toughness Nb-based metallic phase in order to generate a composite that has improved high-temperature and low-temperature mechanical properties. Room-temperature fracture toughness values of $>20 \text{ MPa}\sqrt{\text{m}}$ were measured with a tensile strength of $>350 \text{ MPa}$ at 1200°C . The stress rupture behavior of the MASC is similar to that of advanced single crystal Ni-based superalloys under similar test conditions, and thus, after accounting for the lower density of the MASC, there is an increase in the stress rupture behavior of more than one Larson-Miller parameter. The density is approximately 25% less than that of third-generation single-crystal superalloys. The composite has an elastic modulus of $\sim 140 \text{ GPa}$ at 1200°C .

Both the metallic and silicide phases are designed for improved high-temperature environmental resistance; however, further improvements in the high-temperature oxidation resistance are required. The DS MASC shows material losses at rates intermediate between the rapid losses of an older superalloy like IN 738 and

the improved oxidation behavior of third-generation single crystal superalloys, without any pesting behavior.

3.1.5 References for Section 3.1

- [1] R.W. Buckman, Jr., "Alloying of Refractory Metals," in *Alloying*, ed. J.L. Walter, M.R. Jackson, and C.T. Sims, ASM International, Metals Park, Ohio 1988, pp. 419-445.
- [2] M.R. Jackson, B.P. Bewlay, R.G. Rowe, D.W. Skelly, and H.A. Lipsitt, *J. of Metals* 48 (1), (1996), p. 33.
- [3] P.R. Subramanian, M.G. Mendiratta, and D.M. Dimiduk, *J. of Metals* 48 (1), (1996), p. 33.
- [4] P.R. Subramanian, M.G. Mendiratta, and D.M. Dimiduk, *Mat. Res. Soc. Symp. Proc.*, 322 (1994), pp. 491-502.
- [5] D.M. Dimiduk, M.G. Mendiratta and P.R. Subramanian, in *Structural Intermetallics*, Eds. R. Darolia, J.J. Lewandowski, C.T. Liu, P.L. Martin, D.B. Miracle, and M.V. Nathal, TMS Publications, Warrendale, Pa., (1993), pp. 619-630.

- [6] M.G. Mendiratta, J.J. Lewandowski and D.M. Dimiduk, *Metall. Trans.* 22A (1991), pp. 1573-1581.
- [7] M.G. Mendiratta and D.M. Dimiduk, *Metall. Trans. A* 24A (1993), pp. 501-504.
- [8] J.D. Rigney, P.R. Singh and J.J. Lewandowski, *Mat. Res. Soc. Symp. Proc.* 322 (1994), pp. 502-509.
- [9] I. Weiss, M. Thirukkonda, and R. Srinivasan, *Mat. Res. Soc. Symp. Proc.* 322 (1994), pp. 377-386.
- [10] B.P. Bewlay, H.A. Lipsitt, W.J. Reeder, M.R. Jackson, and J.A. Sutliff, in *Processing and Fabrication of Advanced Materials for High Temperature Applications III*, Ed. V.A. Ravi, T.S. Srivatsan, and J.J. Moore (TMS Publications, Warrendale, PA, 1993) pp. 547-565.
- [11] M.R. Jackson, R.G. Rowe, and D.W. Skelly, Annual Report, *WRDC Contract # F33615-91-C-5613*, (1994).
- [12] M.R. Jackson and K.D. Jones, in *Refractory Metals Extraction, Processing and Applications*, Eds. K.C. Liddell, D.R. Sadoway and R.G. Bautista (TMS Publications, Warrendale, PA, 1991) pp. 310-320.
- [13] K-M. Chang, B.P. Bewlay, J. A. Sutliff, and M.R. Jackson, *J. of Metals* 44 (6), (1992), p. 59.
- [14] "Standard Test Method for Plane-Strain Fracture Toughness of Metallic Materials," ASTM STP E-399, American Society for Testing and Materials, July 1983, pp. 488-512.
- [15] "Standard Practice for R-Curve Determination," ASTM STPE 561-94, American Society for Testing and Materials, Philadelphia, 1994.
- [16] B.P. Bewlay, M.R. Jackson, W.J. Reeder, and H.A. Lipsitt, MRS Proceedings on *High Temperature Ordered Intermetallic Alloys VI*, 1994, Vol. 364, pp. 943-948.
- [17] P.R. Subramanian, M.G. Mendiratta, G. A. Henshall, and M. J. Strum, MRS Symposium on *High Temperature Ordered Intermetallic Alloys VI*, 1994, Vol. 364, pp. 937-942.
- [18] P.R. Subramanian, T.A. Parthasarathy, M.G. Mendiratta, and D.M. Dimiduk, *Scripta Met.* 32(8), pp. 1227-1232, 1995.

3.2 Fracture Behavior of Ternary Alloy Nb-Ti-Si In Situ Composites

3.2.1 Introduction

The addition of Ti to binary Nb-Si based two-phase in-situ composites is very attractive because Ti reduces oxygen embrittlement and the metal recession rates of the constituent phases during exposure at elevated temperatures [1,2]. The addition of Ti to binary Nb-Si based composites also has an important effect on toughness [1-6]. The aim of the present study is to describe the effect of Ti additions to DS Nb-Nb₃Si composites on the microstructure and fracture toughness. Ti additions also have an important effect on the phase equilibria; this topic is discussed in more detail in Section 3.4.

In the present study ternary Nb-Ti-Si alloys with Ti concentrations from 21 to 45%, and Si concentrations from 10 to 25%, were directionally solidified to generate aligned two- and three-phase composites containing a Nb solid solution with Nb₃Si and Nb₅Si₃ silicides. This section focuses on the fracture behavior of these DS composites. The effect of Nb:Ti ratio (at constant Si concentration) on the room temperature fracture toughness is examined. The effect of Si concentration at a constant equal Nb:Ti ratio is also discussed, since this has an important effect on the volume fraction of metallic phase in the composite. The effect of test temperatures of -196 and 500 °C on the fracture toughness is also described. The room temperature fracture toughness measurements of Nb-Ti-Si ternary alloys are compared with binary Nb-Si alloys of similar Si concentrations and volume fractions. In the present section, the Nb₅Si₃ with Ti in solid solution is referred to as Nb(Ti)₅Si₃, and the Ti₅Si₃ with Nb in solid solution is referred to as Ti(Nb)₅Si₃. The Nb₃Si with Ti in solid solution is referred to as (Nb,Ti)₃Si, and simi-

larly, the Nb with Ti and Si in solution is referred to as Nb(Ti, Si).

A schematic diagram of the projection of the liquidus surface of the metal-rich end of the Nb-Ti-Si phase diagram is shown in Figure 3.2.1 [3,5,6]. The first important feature is the eutectic trough from the Nb-Si binary at Nb-18.2Si and 1880 °C. This eutectic trough descends towards the Ti-Ti₅Si₃ eutectic with increasing Ti concentration. The second important feature is the L+Nb(Ti)₅Si₃ → (Nb,Ti)₃Si peritectic ridge on the hypereutectic side of the eutectic valley. Both of these features dominate the microstructures of the Nb-Ti-Si composites generated in this study. The Nb-Ti-Si phase equilibria are discussed in more detail subsequently in Section 3.4. The ranges of hypo and hypereutectic compositions investigated are shown in Figure 3.2.1.

3.2.2 Experimental

Composites were directionally solidified using the procedure described previously in more detail in Section 3.1. The starting alloys were prepared by triple melting high-purity elements (>99.9%) in the segmented water-cooled copper crucible prior to directional solidification. The compositions reported are those of the starting alloys.

Bending bars were prepared by EDM for fracture toughness testing using both monotonic loading and R-curve measurements. Room temperature fracture testing was performed as described in Section 3.1. Elevated temperature (500 °C) and low temperature (-196 °C) fracture toughness tests were performed using three-point bending, as described by Rigney et al. [7]. In the case of the measurements at -196 and 500 °C, fracture tough-

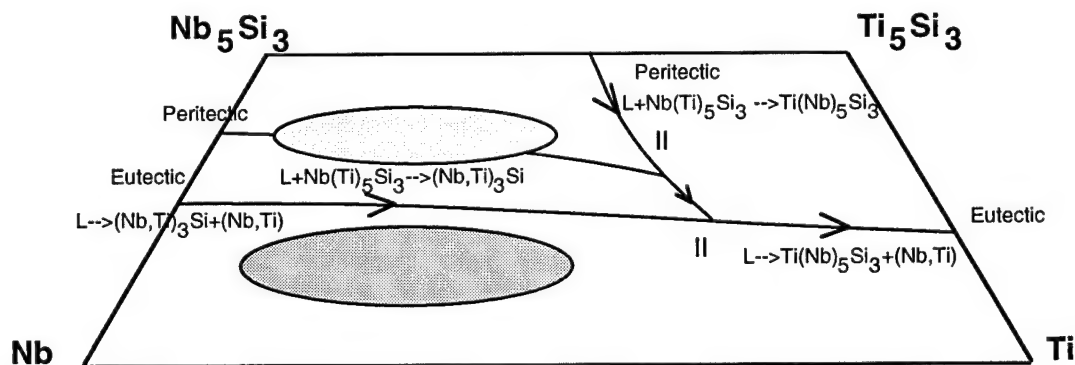


Figure 3.2.1 Schematic diagram of the projection of the liquidus surface of the metal-rich end of the Nb-Ti-Si ternary phase diagram. The composition ranges of the hypo and hypereutectic alloys that were directionally solidified are shown.

ness measurements are reported as K_Q rather than K_{IC} because ASTM 399 could not be followed rigorously.

3.2.3 Results and Discussion

Microstructures of Ternary Alloys

The compositions of the alloys from which the composites were directionally solidified are listed in Table 3.2.1. Ternary Nb-Ti-Si alloys with Si concentrations of 10-16% and Ti concentrations of 21-45% were all on the metal-rich side of the eutectic valley, so that the primary solidification phase was Nb(Ti, Si) dendrites, together with large-scale (Nb,Ti)₃Si dendrites. Microstructures of the longitudinal and transverse sections of the Nb-33Ti-16Si composition are shown in Figure 3.2.2 (a) and (b). These were typical of compositions from the hypoeutectic side of the valley. The microstructures consisted of non-faceted Nb(Ti, Si) dendrites, which are the lighter phase in these BSE micrographs, together with large scale (40-80 μ m) faceted gray (Nb,Ti)₃Si dendrites; both the non-faceted metal dendrites and faceted (Nb,Ti)₃Si dendrites were generally aligned with the growth direction, although the aspect ratios of the phases were sensitive to composition. The volume fractions of Nb(Ti, Si) and (Nb,Ti)₃Si are also shown in Table 3.2.1.

Ternary alloys with Si concentrations of 19-25% and Ti concentrations of 21-40% were on the Si-rich side of the eutectic valley and they therefore experienced the peritectic reaction, $L + \text{Nb}(\text{Ti})_5\text{Si}_3 \rightarrow (\text{Nb, Ti})_3\text{Si}$. Typical microstructures of the DS Nb-27Ti-22Si composite are shown in Figure 3.2.3(a) and (b); composites from this alloy range possessed three phases. First, there was a small volume fraction of primary Nb(Ti)₅Si₃ dendrites at the cores of the silicide dendrites; the

Nb(Ti)₅Si₃ appeared as the dark phase in Figure 3.2.3(a) and (b). Second, there were faceted (Nb,Ti)₃Si dendrites; these were the gray phase in Figure 3.2.3. Third, there were metal-rich Nb(Ti, Si) dendrites between the (Nb,Ti)₃Si dendrites; the Nb(Ti, Si) was the lightest phase in the BSE images. The longitudinal section showed aligned Nb(Ti, Si) and (Nb,Ti)₃Si dendrites, with primary Nb(Ti)₅Si₃ at the cores of the (Nb,Ti)₃Si dendrites. These microstructures are analogous to those which have been reported previously in hypereutectic binary DS Nb-Si composites [3].

Essentially all the hypereutectic compositions listed in Table 3.2.1 possessed at least a small volume fraction of Nb(Ti)₅Si₃ and not just (Nb,Ti)₃Si. This situation arises because of the proximity of the peritectic ridge to the eutectic valley, and as a result, most hypereutectic compositions experienced the peritectic reaction.

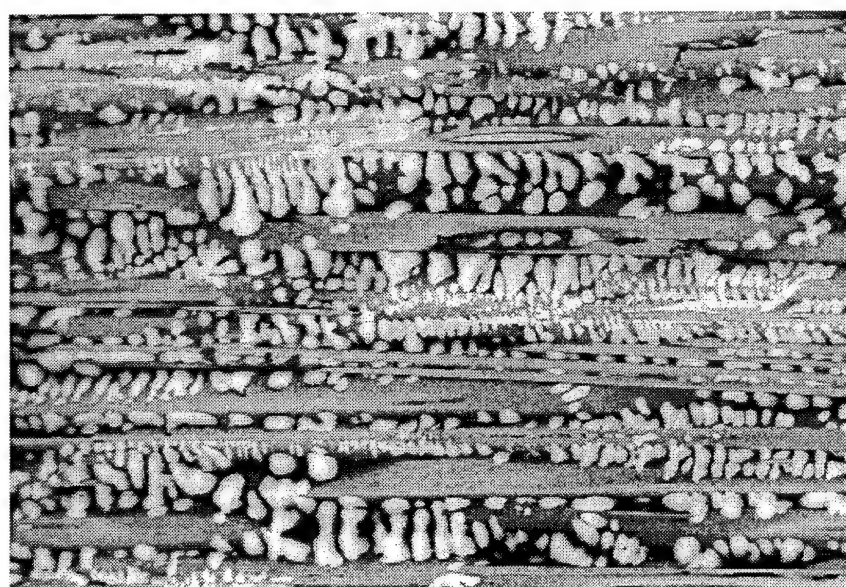
The BSE images in Figures 3.2.2 and 3.2.3 showed strong dark contrast in the inter-dendritic regions of both the hypo and hypereutectic Nb-Ti-Si alloys. This could have been due to either the presence of a silicide (e.g., Nb(Ti)₅Si₃ or Ti(Nb)₅Si₃) or segregation of either Ti or Si to the inter-dendritic regions. Energy dispersive spectrometry and electron microprobe analyses indicated that this contrast was due to local Ti enrichment of the edges of the (Nb,Ti)₃Si dendrites. Electron microprobe analysis measurements of the phases are described subsequently in Section 3.4.

Room Temperature Fracture Toughness: Effect of Nb:Ti Ratio

Room temperature fracture toughness measurements of the DS Nb-Ti-Si composites are shown in Table 3.2.2 and Figure 3.2.4. Generally, Ti additions increase the

Table 3.2.1 Ternary alloy compositions together with DS composite volume fractions and dendrite arm diameters.

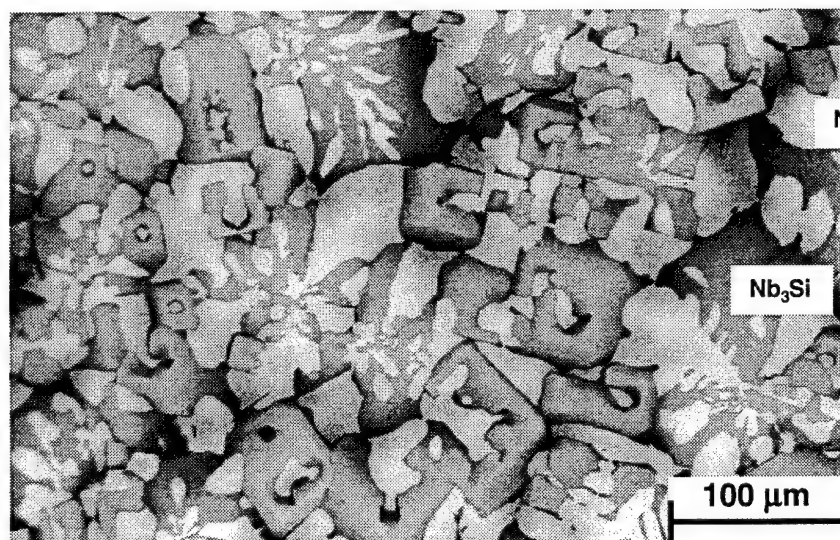
Composition	Volume Fractions		Nb(Ti,Si) Dendrite arm diameter (μ m)
	Nb(Ti,Si)%	Nb(Ti,Si) ₃ Si %	
Nb-21%Ti-12%Si	54.3	45.7	22
Nb-21%Ti-16%Si	34.5	66.5	—
Nb-21%Ti-22%Si	23.3	76.7 (3:1 and 5:3)	5.6
Nb-27%Ti-12%Si	48.5	51.5	15
Nb-27%Ti-16%Si	41.3	58.7	—
Nb-32.3%Ti-19.2%Si	27.3	72.7 (3:1 and 5:3)	—
Nb-33%Ti-16%Si	37.4	62.6	15
Nb-42.5%Ti-15%Si	36.6	63.4	10
Nb-37.5%Ti-25%Si	18.9	81.1 (3:1 and 5:3)	—



Growth Direction

200 μm

(a)



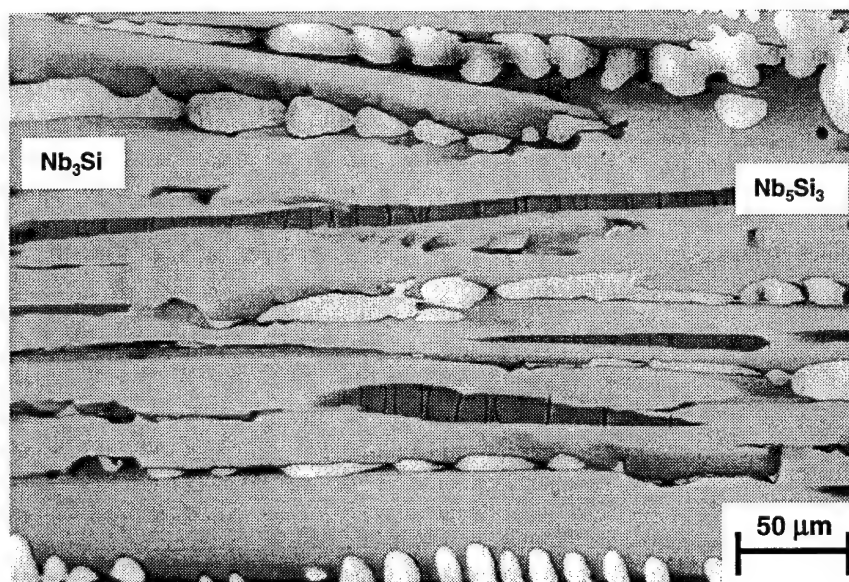
Nb(Ti,Si)

Nb₃Si

100 μm

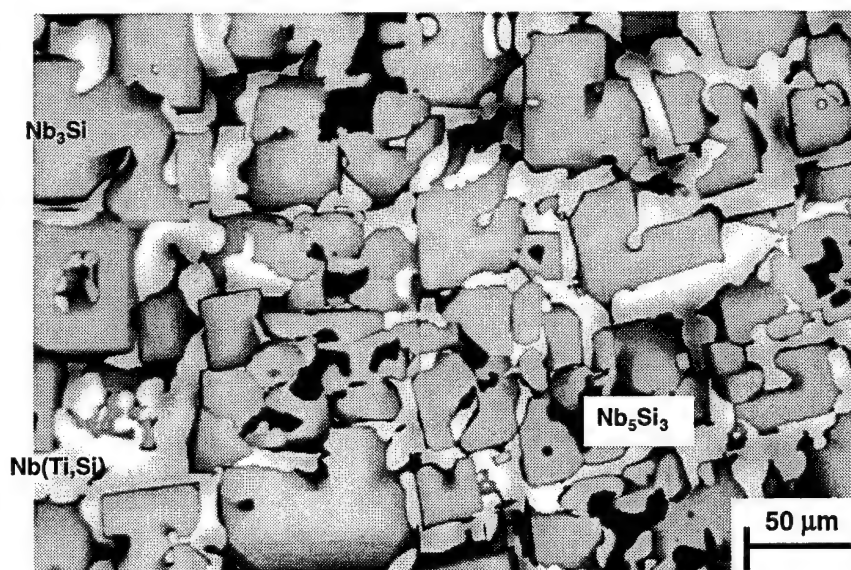
(b)

Figure 3.2.2 Typical microstructures (BSE images) of (a) the longitudinal section, and (b) the transverse section of a DS hypoeutectic Nb-33Ti-16Si Nb(Ti,Si)-(Nb,Ti)₃Si composite.



Growth Direction

(a)



(b)

Figure 3.2.3 Typical microstructures (BSE images) of (a) the longitudinal section of a DS hypereutectic Nb-27Ti-22Si composite, and (b) the transverse section of a DS hypereutectic Nb-21Ti-22Si composite. These composites contain Nb(Ti,Si) (white phase), (Nb,Ti)₃Si (gray phase), and a small volume fraction of Nb(Ti)₅Si₃ (dark phase).

Table 3.2.2. Room temperature fracture toughness of DS ternary Nb-Ti-Si in-situ composites.

Composition (at%)	Constituent Phases	Fracture Toughness (MPa√m): Monotonic Loading, K_q	Fracture Toughness (MPa√m): R-Curve Measurements, K_{Ic}
Nb-33Ti-16Si	Nb(Ti,Si), (Nb,Ti) ₃ Si	11.1	17.5
Nb-27Ti-16Si	Nb(Ti,Si), (Nb,Ti) ₃ Si	11.7	—
Nb-27Ti-12Si	Nb(Ti,Si), (Nb,Ti) ₃ Si	9.8	13.8
Nb-27Ti-22Si	Nb(Ti,Si), (Nb,Ti) ₃ Si, Nb(Ti) ₅ Si ₃	—	12.8
Nb-21Ti-16Si	Nb(Ti,Si), (Nb,Ti) ₃ Si	11.6	15.0
Nb-21Ti-12Si	Nb(Ti,Si), (Nb,Ti) ₃ Si	10.6	16.0
Nb-21Ti-22Si	Nb(Ti,Si), (Nb,Ti) ₃ Si, Nb(Ti) ₅ Si ₃	12.1	13.7, 12.0
Nb-32Ti-19Si	Nb(Ti,Si), (Nb,Ti) ₃ Si, Nb(Ti) ₅ Si ₃	12.4	—
Nb-33Ti-20Si	Nb(Ti,Si), (Nb,Ti) ₃ Si, Nb(Ti) ₅ Si ₃	10.8	15.0
Nb-37.5Ti-25Si	Nb(Ti,Si), (Nb,Ti) ₃ Si, Nb(Ti) ₅ Si ₃	—	10.4
Nb-40Ti-20Si	Nb(Ti,Si), (Nb,Ti) ₃ Si, Nb(Ti) ₅ Si ₃	14.3	12.2
Nb-42.5Ti-15Si	Nb(Ti,Si), (Nb,Ti) ₃ Si	12.3	—
Nb-45Ti-10Si	Nb(Ti,Si), (Nb,Ti) ₃ Si	—	16.0
Nb-10Si	Nb(Si), Nb ₃ Si	14.2	—
Nb-12Si	Nb(Si), Nb ₃ Si	11.2	6.5
Nb-16Si	Nb(Si), Nb ₃ Si	7.8	—
Nb-20Si	Nb(Si), Nb ₃ Si, Nb ₅ Si ₃	7.1	—
Nb-22Si	Nb(Si), Nb ₃ Si, Nb ₅ Si ₃	8.5	—

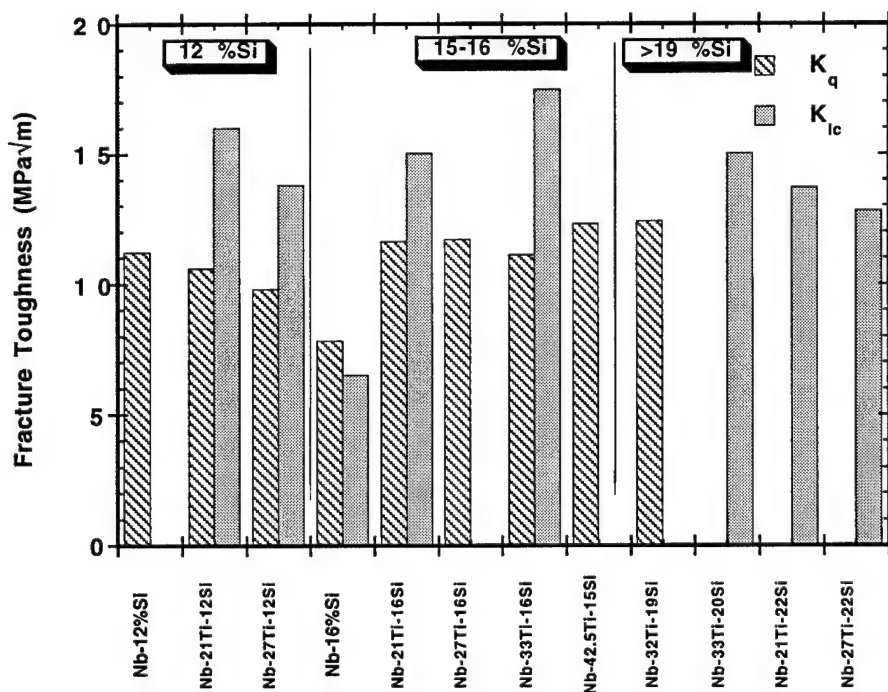


Figure 3.2.4 Fracture toughness of the ternary Nb-Ti-Si composites.

toughness of the DS composites over the Nb-Si binary composites of the same Si concentration. For example, the toughness data of the Nb-33Ti-16Si, Nb-27Ti-16Si, and Nb-21Ti-16Si alloys are ~50% greater than that of the binary Nb-16%Si composite. However, there is no systematic increase of fracture toughness with increasing Ti concentration. The toughness of the composite with 33%Ti is essentially the same as that with 21%Ti. This suggests that there may be a threshold Ti concentration above which the Ti additions have no further effect on the fracture toughness. Over the range of Ti concentrations examined further additions do not lead to further toughness improvements. These data suggest that this threshold composition is less than 21%Ti. Composites from alloys with reduced Ti concentrations (with as little as 3%Ti) are under investigation and will be reported separately. The toughness improvement effected by Ti additions was also observed in the ternary alloys with 20 and 22%Si. However, for the 12%Si compositions the ternary and binary fracture toughness measurements were similar.

Figure 3.2.5 shows R-curves from the DS Nb-21Ti-12Si and the DS Nb-21Ti-22Si composites. This behavior is typical of the form of most of the R-curves of the ternary compositions. All the ternary composites exhibited R-curve behavior. There appears to be a lack of sensitivity of crack propagation to the Si concentration. The K_{IC} values from R-curve measurements are included in Table 3.2.2. Generally, the K_{IC} values from the R-curves are slightly higher than K_Q values from the monotonic loading experiments.

There are three possible reasons for the toughness in-

crease generated by the addition of Ti to the binary Nb-Si composites. First, whereas in the binary alloy composites the metallic phase exists as a combination of fine-scale eutectic and large-scale dendritic morphologies, in the Nb-Ti-Si alloys the metallic phase exists only as large-scale Nb(Ti, Si) dendrites. Thus, the same volume fraction of metallic phase may provide more toughening in the case of the ternary alloy. This could also explain the Si concentration sensitivity of the toughening increment effected by Ti, because at 12%Si the large volume fraction of primary metal dendrites would make the composite less sensitive to the effect of Ti due to the scale of the microstructure. Second, the Ti-modified metallic phase may have greater intrinsic toughness than the Nb(Si) in the binary composite. Third, fractography indicated that a larger volume fraction of the metal dendrites failed in a ductile manner in the Nb-Ti-Si composites (essentially 100%) than in the binary Nb-Si composites [7].

Room Temperature Fracture Toughness: Effect of Si concentration

Table 3.2.2 indicates that increasing the Si concentration from 12 to 22% has little effect on the fracture toughness. For example, for the 21%Ti compositions, increasing the Si concentration had little effect on the K_Q and K_{IC} values: the K_Q values were 10.6, 11.6, and 12.0 for the 12, 16, and 22%Si compositions, respectively. Similarly, the K_{IC} values were 16.0, 15.0, and 12.6 for the 12, 16, and 22%Si compositions, respectively. For the 27%Ti, the K_Q and K_{IC} values are in the range 9.8-13.8 with no apparent trend with Si concen-

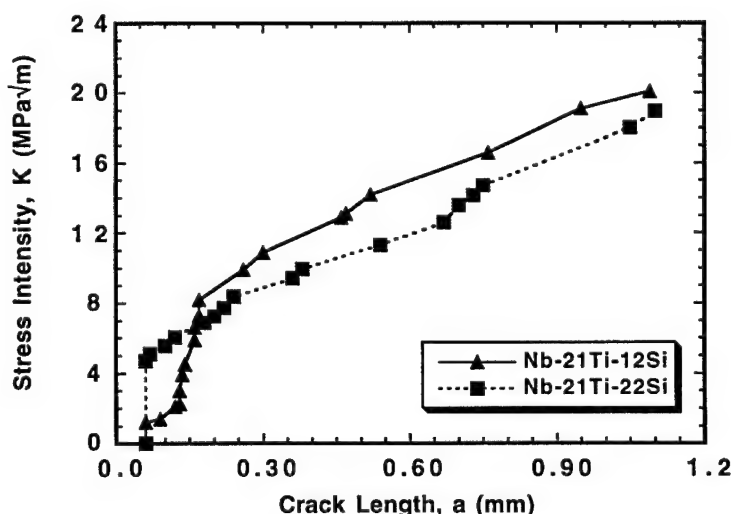


Figure 3.2.5 R-curves for DS Nb-21Ti-22Si and Nb-21Ti-12Si composites

tration. This apparent insensitivity of fracture toughness to Si concentration for the alloys discussed probably results from the inconsistent changes in the volume fraction of metallic phase, as shown in Table 3.2.1; for example, for the 21% Ti-containing composite, increasing the Si concentration from 12 to 16% reduces the metal volume fraction from 54 to 35, but for the 27%Ti-containing composite, the volume fraction of metal is only reduced from 49 to 41 for the same Si increase. In the case of the binary Nb-Si in-situ composites, the toughness increased with decreasing Si concentration and increasing volume fraction of (Nb); decreasing the Si concentration from 18 to 10% increased the (Nb) volume fraction from ~0.35 to ~0.75 and the fracture toughness values from 6 to 14 MPa√m, respectively. In the ternary alloys, the lower than expected reduction in volume fraction of metal with increasing Si concentration at high Ti concentrations is probably due to the form of the solvus surface since the (Nb,Ti)₃Si maintains the stoichiometric Si concentration, and the locus of the eutectic trough probably leads to only a small increase in the volume fraction of Nb(Ti,Si) with decreasing Si concentration. Thus, at constant Ti concentration (rather than constant and equal Nb:Ti ratio), changing the Si concentration does not necessarily change the volume fraction of metal, as in the case of binary alloys, because the starting compositions do not necessarily move along a tie line between the phases. Consequently, the effect of Si concentration at constant and equal Nb:Ti ratio concentrations was investi-

gated because these compositions are close to being on the same tie-line.

In order to address this difficulty the effect of Si was examined at equal Nb and Ti concentrations. Four compositions were selected at concentrations of 10, 15, 20, and 25%Si. The toughness measurements, also shown in Table 3.2.2, indicate an increase in K_{IC} from 10.4 MPa√m at Nb-37.5Ti-25Si to 16.0 MPa√m at Nb-45Ti-10Si. This suggests a similar sensitivity of K_{IC} to the volume fraction of metal in the ternary alloy composites to the binary Nb-Si alloys composites. However, K_{IC} does not appear to reach a minimum at the eutectic trough (~15%Si), as is the case for the binary Nb-18.2%Si eutectic. A possible explanation for the absence of the minimum is the microstructural scale of the metallic phases. In the binary eutectic, the majority of the toughening is provided only by the fine-scale eutectic Nb, but in the ternary alloys, there is a larger volume fraction of the large-scale Nb(Ti,Si) to provide toughening.

Figure 3.2.6 shows the fracture surface of a Nb-27Ti-12Si composite after monotonic loading at room temperature. A large fraction of the Nb(Ti, Si) dendrites failed in a ductile manner, and the (Nb,Ti)₃Si matrix failed by cleavage. Microvoid coalescence in the Nb(Ti, Si) dendrites can be seen in Figure 3.2.6. Generally, dendrite arms with dimensions as large as 50 μm failed in a ductile manner; there was extensive microcracking of the (Nb,Ti)₃Si silicide matrix around the ruptured

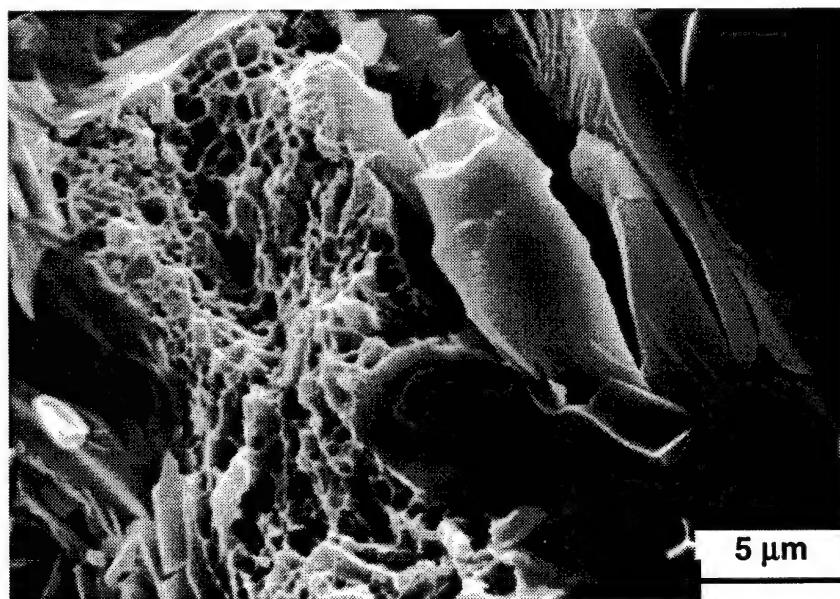
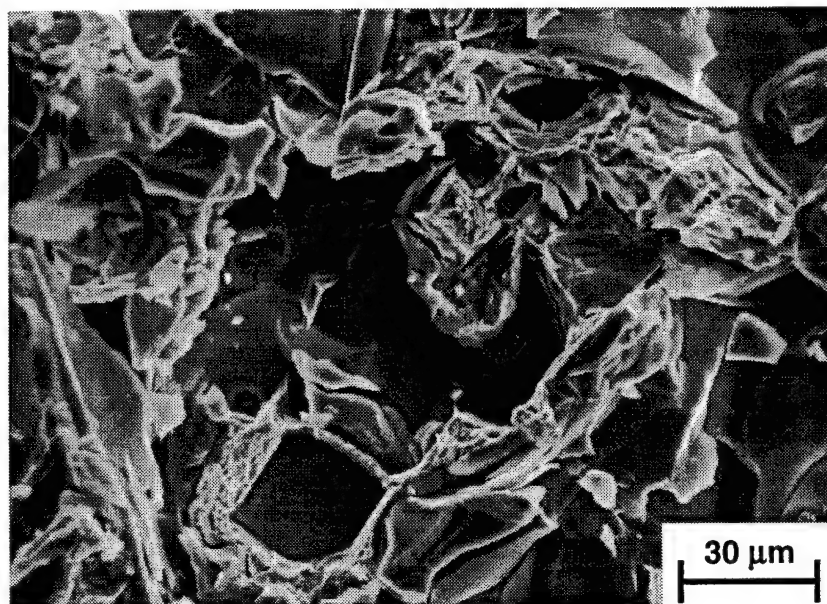


Figure 3.2.6 Fracture surfaces of DS Nb-27Ti-12Si composite.

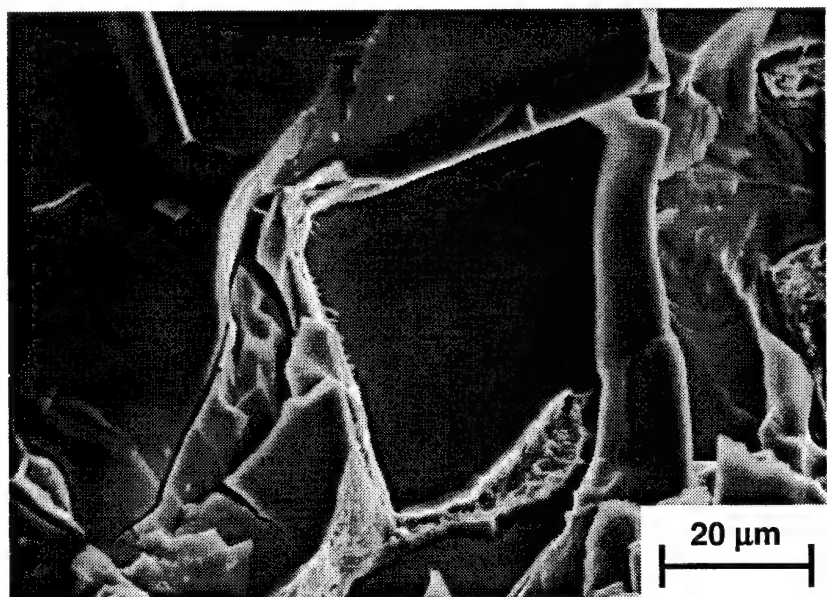
dendrites. The apparent increase in the proportion of primary metallic dendrites that failed by microvoid coalescence in comparison with that observed in the binary alloys is probably related to the higher ductility of the Nb(Ti, Si) dendrites as compared to Nb(Si) dendrites, as well as their slightly smaller size (Table 3.2.1). Ti may also affect the nature of the constraint of the metallic dendrites by the silicide. This could be related

to both the scale of the metallic phase and the morphologies of both phases in the composite.

The fracture surfaces of a hypereutectic DS Nb-40Ti-20Si composite after an R-curve experiment at room temperature are shown at high and low magnifications in Figure 3.2.7(a) and (b). The fracture surfaces are similar to those of the hypoeutectic alloys. The fracture surfaces show extensive ductile failure of the me-



(a)



(b)

Figure 3.2.7 Fracture surfaces of the DS Nb-40Ti-20Si composite.

tallic phase and cleavage of the faceted (Nb,Ti)₃Si dendrites. Ductile failure of the fine-scale metallic phase between the (Nb,Ti)₃Si dendrites is shown in Figure 3.2.7(b).

Examination of the crack path during crack propagation through the ternary composites, which were unloaded prior to unstable crack growth, revealed crack deflection and crack multiplication. The intermetallic dendrites appeared to cause crack deflection; this probably also provided toughening of the composite. Plastic deformation of the metallic dendrites which were intersected by the crack was also observed. Bridging events and crack blunting by metallic dendrites were also observed during the R-curve tests of the ternary alloy composites.

Effect of Temperature on Fracture Toughness

Table 3.2.3 shows fracture toughness measurements for several ternary Nb-Ti-Si alloy composites at temperatures of -196 °C, 25 °C, and 500 °C. Fracture toughness measurements at -196 °C and 500 °C were performed using three-point bending [7]. The room temperature fracture toughness measurements, K_{IQ} , included in Table 3.2.3 for comparison are from four-point bending monotonic loading experiments, as shown previously in Table 3.2.2.

There appears to be very little effect of test temperature on the toughness of these ternary Nb-Ti-Si composites for temperatures up to 500 °C. Although the fracture toughness values were similar at test temperatures of -196 °C and 500 °C, the crack propagation was unstable at -196 °C and the samples failed catastrophically. However, at room temperature and 500 °C the cracks propagated in a stable manner and R-curve

behavior was observed. In the hypereutectic compositions, the fracture toughness measurements were lower for test temperatures of -196 °C and 500 °C than were the room temperature measurements; this may be an artifact of the different testing schemes. Thus, although the test temperature appears to have little effect on the fracture toughness, it has a large effect on the stability of crack propagation. Further examination of the fracture behavior of the composites is required to determine the origin of the unstable nature of crack propagation.

Fractography indicated that at test temperatures of -196 °C and above, the primary (Nb,Ti) dendrites failed by microvoid coalescence [5, 7]. Microvoid coalescence has been observed in binary Nb(Si) phases of Nb-Nb₅Si₃ composites, but only at higher temperatures [1,7]. Typically at room temperature and below, the primary Nb(Si) dendrites of binary composites fail by a combination of cleavage in some areas and microvoid coalescence in other areas. However, in the case of the ternary alloy composites, the occurrence of microvoid coalescence and the fracture behavior are less sensitive to temperature. This suggests that the test temperature of -196 °C is above the ductile-brittle transition temperature (DBTT) of the Nb(Ti,Si) in the ternary composites, but below that of the Nb(Si) in the binary alloy composites. The implication is that Ti additions reduce the DBTT of the binary Nb(Si). However, the DBTT of the Nb(Ti,Si) may still be above that of pure Nb, which is reported to be less than -200 °C [8].

3.2.4 Conclusions

The ternary Nb-Ti-Si composites investigated contained dendritic Nb(Ti,Si) and (Nb,Ti)₃Si. In the case of the

Table 3.2.3. The effect of test temperatures of -196 and 500 °C on the fracture toughness of DS ternary Nb-Ti-Si composites.

Composition		Nb(Ti, Si) (Vol.%)	Fracture Toughness (MPa√m)		
at.% Si	at.% Ti		-196 °C	25 °C	500 °C
12	21	54.3	11.3	10.6	11.0
12	27	41.3	9.7	9.8	—
16	21	34.5	11.1	11.6	10.8
16	27	27.3	9.2	11.7	10.7
16	33	37.4	10.7	11.1	10.1
15	42.5	36.6	10.3	12.3	9.9
20	33	27.3	10.0	10.8	9.9
22	21	23.3	7.8	12.1	6.8

hypereutectic alloys, a small volume fraction of $\text{Nb}(\text{Ti})_5\text{Si}_3$ was also observed. Fracture toughness values greater than $10 \text{ MPa}\sqrt{\text{m}}$ were consistently measured using monotonic loading. R-curve measurements provided K_{IC} values of $>17 \text{ MPa}\sqrt{\text{m}}$. Ti additions can increase in-situ composite fracture toughness values as much as $6 \text{ MPa}\sqrt{\text{m}}$ in comparison with binary alloys with the same Si concentration. This is probably due to a larger volume fraction of the metallic phase existing as large-scale dendrites, and possibly also greater ductility of the metallic phase. Some sensitivity of the fracture toughness to the volume fraction of metallic phase was observed in the Nb-Ti-Si composites, but no minimum of the form observed in binary Nb-Si eutectic composites was detected. All the ternary Nb-Ti-Si alloy composites exhibited R-curve behavior at room temperature. Fractography indicated that substantially more complex fracture behavior occurred in the ternary Nb-Ti-Si composites than in the Nb-Si binaries; ductile failure of the metal dendrites and multiple plane cleavage of the silicide were generally observed. Test temperatures in the range -196 to 500°C had little effect on the fracture toughness of these composites. However, the test temperature had a large effect on the stability of crack propagation; below room temperature the cracks propagated in an unstable manner.

3.2.5 References for Section 3.2

- [1] P.R. Subramanian, M.G. Mendiratta, and D.M. Dimiduk, *Mat. Res. Soc. Symp. Proc.*, 322 (1994), pp. 491-502.
- [2] M.R. Jackson, R.G. Rowe, and D.W. Skelly, Annual Report, *WRDC Contract # F33615-91-C-5613*, (1994).
- [3] B.P. Bewlay, M.R. Jackson, W.J. Reeder, and H.A. Lipsitt, *MRS Proceedings on High Temperature Ordered Intermetallic Alloys VI*, 1995, Vol. 364, pp. 943-948.
- [4] M.R. Jackson and K.D. Jones, in *Refractory Metals Extraction, Processing and Applications*, Eds. K.C. Liddell, D.R. Sadoway and R.G. Bautista (TMS Publications, Warrendale, PA, 1991) pp. 310-320.
- [5] P.R. Subramanian, M.G. Mendiratta, and D.M. Dimiduk, *J. of Metals* 48 (1), (1996), p. 33.
- [6] M.R. Jackson, B.P. Bewlay, R.G. Rowe, D.W. Skelly, and H.A. Lipsitt, *J. of Metals* 48 (1), (1996), p. 33.
- [7] J.D. Rigney, P.R. Singh, and J.J. Lewandowski, *Mat. Res. Soc. Symp. Proc.* 322 (1994), pp. 502-509.
- [8] A.G. Imgram, E.S. Bartlett and H.R. Ogden, *Trans. Met. Soc. AIME* 227 (1963), p. 131.

3.3 Orientation Imaging of a Nb-33Ti-16Si DS In-Situ Composite

3.3.1 Introduction

In this section the microtexture of a directionally solidified (DS) Nb-Ti-Si alloy is described. Evaluation of both microstructure and microtexture is needed to interpret the orientation-dependent mechanical behavior of these composites. The directionally solidified ingot had a composition of Nb-33%Ti-16at%Si and was prepared with a growth rate of 5 mm/min. The microstructure was examined using backscattered electron imaging, and the microtexture of each of the phases was determined using the Electron BackScattering Pattern (EBSP) technique for electron diffraction in the scanning electron microscope [1]. The details of the investigations were similar to those reported previously in Nb-Nb₃Si-Nb₅Si₃ composites generated from binary Nb-Si alloys [2]. Automated EBSP scans were acquired in order to map the local texture (microtexture) over most of a transverse cross-section of the ingot. The findings of this study will be presented at the 1996 Microscopy Society of America (MSA) conference.

3.3.2 Results and Discussion

Figure 3.3.1 is a scanning electron micrograph, taken using backscattered electron imaging (BSE), of a transverse section of the as-DS microstructure. In this micrograph, the bcc-Nb phase was the lighter gray phase, and it had a dendritic structure. The dark gray phase was (Nb,Ti)₃Si; it had a Ti₃P-type crystal structure. The (Nb,Ti)₃Si silicide phase appeared as both multiply faceted dendrites and irregularly bounded grains. The irregular dendrites were generally at the intercellular regions. No fine-scale interdendritic eutectic was observed in this composite. Shadowing was observed at the edges of the (Nb,Ti)₃Si dendrites. Crystallographic measurements and electron beam microanalysis indicated that this was caused by Ti segregation.

Figure 3.3.1 also shows an exact region that was analyzed by automated-EBSP, the results of which are shown in Figure 3.3.2(a) and (b). Figure 3.3.2 contains orientation images generated from the automated-EBSP data set. In Figure 3.3.2(a), the color black designates areas for which no Nb diffraction patterns could be indexed and other shades of gray signify specific Nb orientations, as described by a set of Euler angles. A similarly generated orientation image for the silicide phase is shown in Figure 3.3.2(b). Macrottexture data

are also presented in Figure 3.3.3 and show strong crystallographic texture in both phases. Figure 3.3.3(a) shows an inverse pole figure of the (Nb) dendrites in the composite. It shows broad alignment of the [113] with the growth direction. A {100} pole figure of (Nb,Ti) is shown in Figure 3.3.3(b), indicating the evenly distributed fiber texture. A (100) pole figure of (Nb₃Ti)Si is shown in Figure 3.3.3(c), indicating strong alignment of the [001] with the growth direction of the composite, as well as orientation clustering in the radial direction. This was also observed in additional measurements extending over many cells. This suggests that there are very few (Nb₃Ti)Si grains in the composite.

3.3.3 Conclusions

Two principal conclusions can be drawn from the EBSP data. First, the orientation images showed distinct regions in which the silicide and metallic grains had a single orientation. These regions corresponded to the large-scale solidification cells that were suggested by the scanning electron micrographs. Second, both phases in this composite exhibited strong texture. The silicide phase had a very strong alignment of the [001] with the growth direction and significant orientation clustering in a radial direction, giving an appearance more like a single crystal than a fiber texture oriented polycrystal. The metallic phase had a less intense, broader alignment of the [113] with the growth direction and had a more evenly distributed fiber texture. Further analyses of the automated-EBSP data to determine additional information, such as intra- and inter-cellular misorientation distributions, are in process. These results are significant with respect to the anisotropic mechanical properties of this material and may help to explain the improved creep performance of DS composites with respect to similar extruded composites.

3.3.4 References for Section 3.3

- [1] J.A. Venables and C.J. Harland, *Philosophical Magazine*, **27** (1973) 1193.
- [2] J. A. Sutliff, B.P. Bewlay and M.R. Jackson, *Proceedings of the 53rd Annual Meeting of the Microscopy Society of America*, Eds., G.W. Bailey and A.J. Garret-Reed, San Francisco Press, 1995, p. 123.

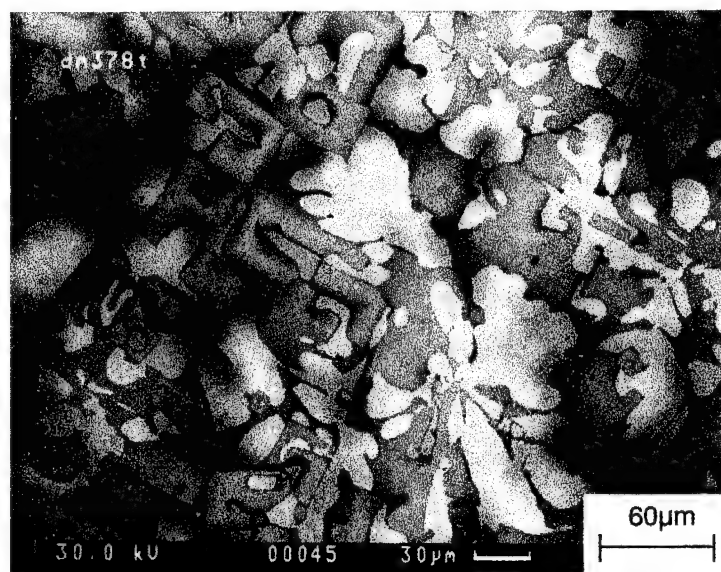
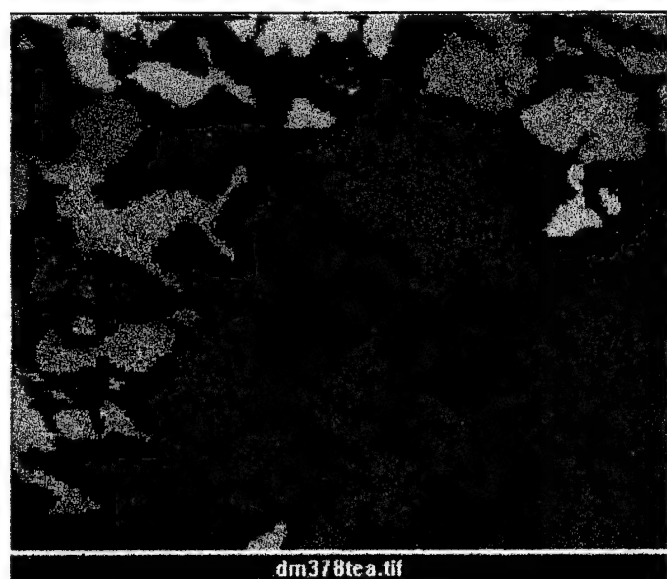
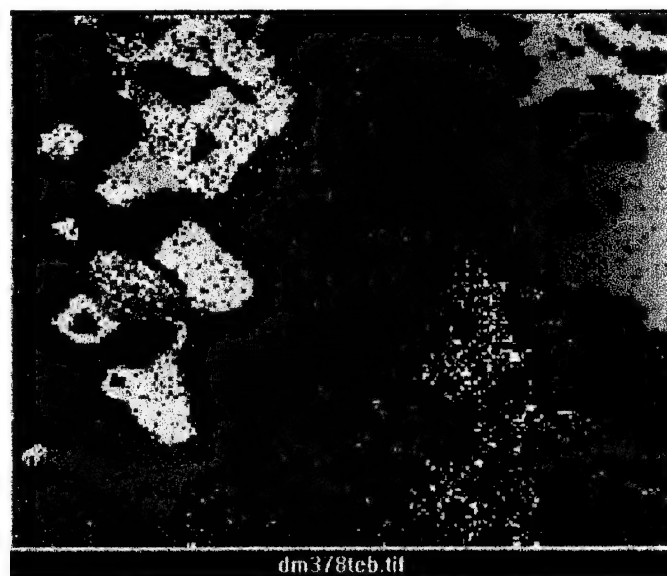


Figure 3.3.1. Scanning electron micrograph (BSE) of DS Nb-Ti-Si alloy, showing the sub-region analyzed using automated-EBSP.

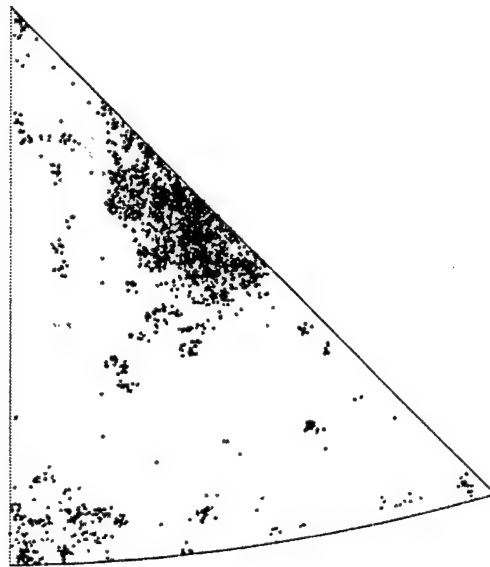


(a)

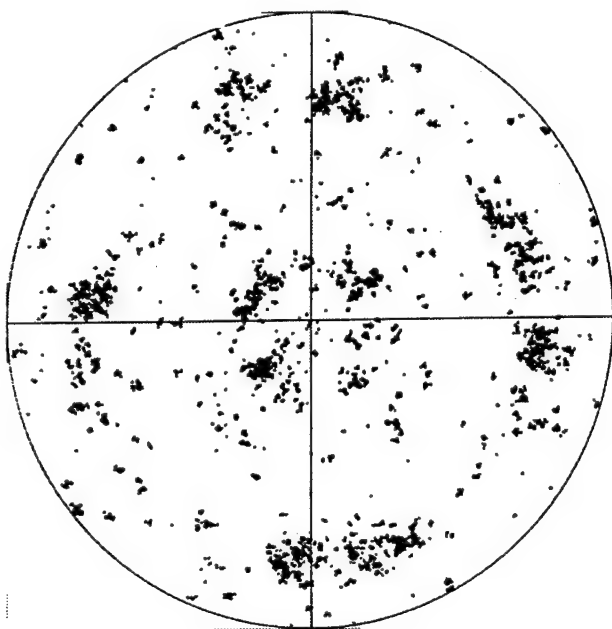


(b)

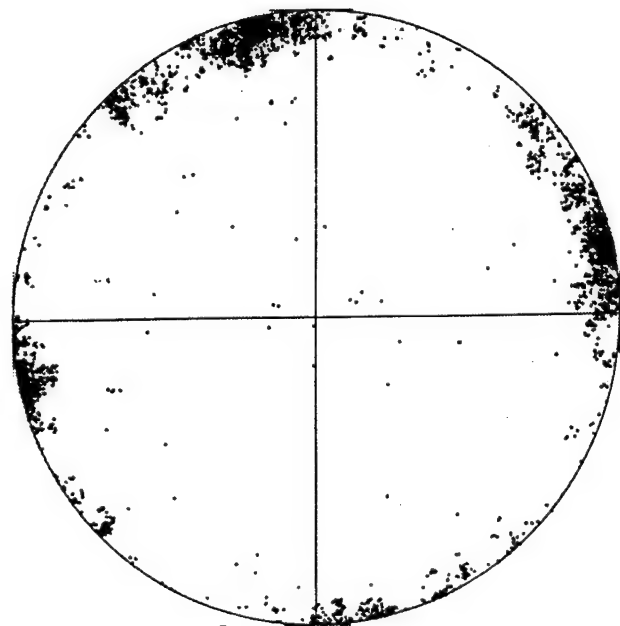
Figure 3.3.2. Orientation images for (a) the (Nb,Ti) phase and (b) the $(\text{Nb,Ti})_3\text{Si}$ phase



(a)



(b)



(c)

Figure 3.3.3. Macrotexture data as (a) Nb inverse pole figure of growth direction, (b) Nb {100} pole figure, and (c) (Nb,Ti)₃Si pole figure.

3.4 Ternary Phase Equilibria in the Nb-Ti-Si Ternary System

3.4.1 Introduction

There has been limited previous work on the Nb-Ti-Si ternary phase equilibria [1, 2], and almost no previous work on the liquidus surface. A projection of the metal-rich region (up to 37.5%Si) of the Nb-Ti-Si phase diagram is shown in Figure 3.4.1. A projection of the proposed liquidus surface is shown in Figure 3.4.2(a) [2]. The liquidus surface is the focus of the present section, because it influences the constituent phases and the structure of DS composites. The phase equilibria evidence substantiating these projections will be described. Four phases are considered in the present section: a Nb-Ti-Si solid solution, Nb_3Si , Nb_5Si_3 , and Ti_5Si_3 . Nb_5Si_3 and Ti_5Si_3 are not isomorphous and have tI32 and hP16 crystal structures, respectively [3]. The solvus

surfaces for $\text{Nb}(\text{Ti})_5\text{Si}_3$ and $\text{Ti}(\text{Nb})_5\text{Si}_3$ shown in Figure 3.4.1 were determined by Jackson, et al. [4] in alloys which also contained small Hf, Cr, and Al additions.

In the present section the Nb_5Si_3 with Ti in solid solution is referred to as $\text{Nb}(\text{Ti})_5\text{Si}_3$, and the Ti_5Si_3 with Nb in solid solution is referred to as $\text{Ti}(\text{Nb})_5\text{Si}_3$. The Nb_3Si with Ti in solid solution is referred to as $(\text{Nb},\text{Ti})_3\text{Si}$, because Nb_3Si and Ti_3Si are isomorphous. Similarly, the Nb with Ti and Si in solution is referred to as $\text{Nb}(\text{Ti},\text{Si})$, there being a continuous bcc solid solution between Nb and Ti at the metal-rich end of the phase diagram. These individual phases can be clearly distinguished in the DS microstructures. In addition, the Nb_5Si_3 , Ti_5Si_3 , Nb_3Si , and metallic phases (dendritic

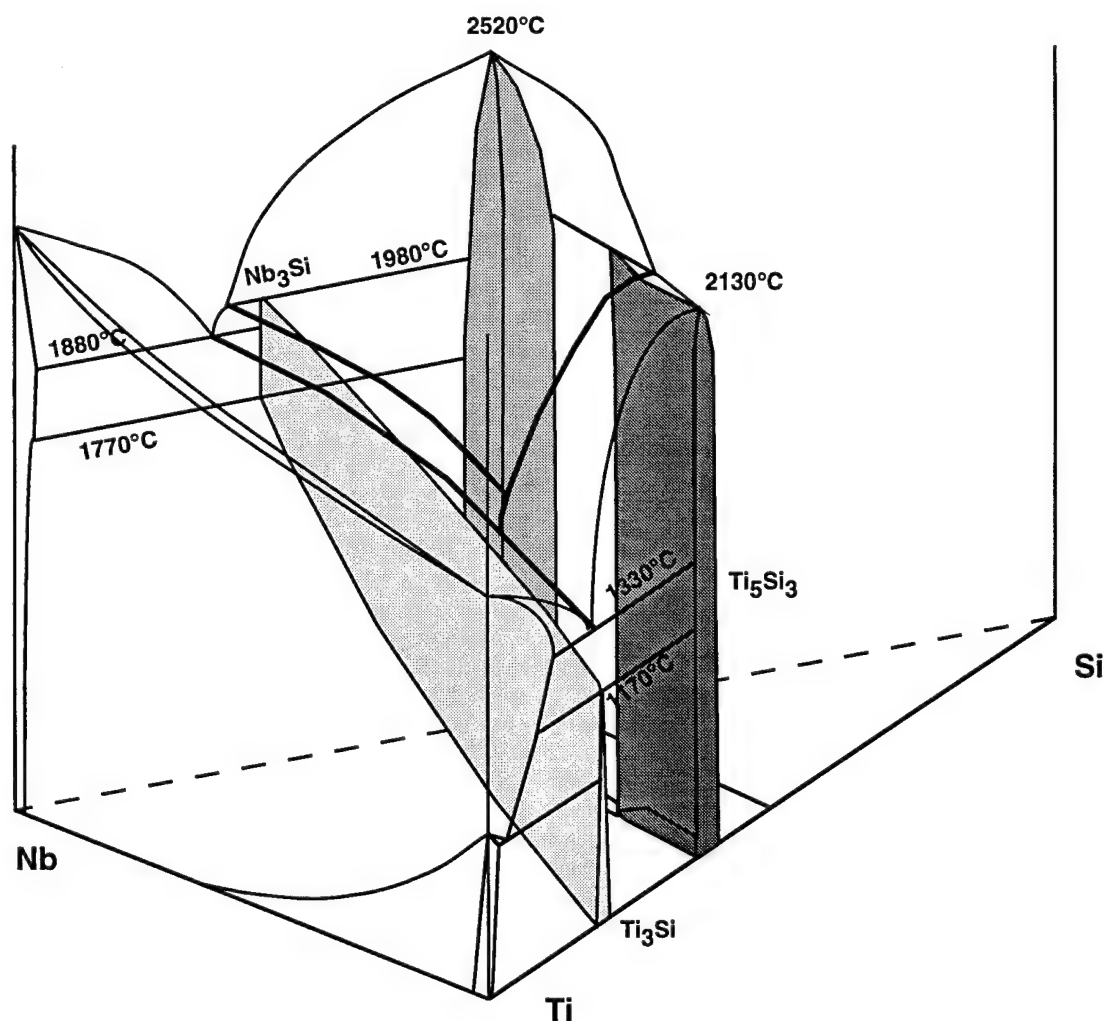


Figure 3.4.1. Schematic diagram of the proposed Nb-Ti-Si ternary phase diagram for compositions between 0 and 37.5%Si.

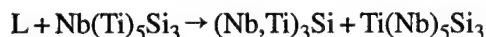
and eutectic) can also be easily distinguished by their morphology, scale, and contrast when examined using BSE imaging in the scanning electron microscope.

3.4.2 Background on Nb-Ti-Si Phase Equilibria

The binary Ti-Si phase diagram [3] possesses a eutectic of the form $L \rightarrow \text{Ti}_5\text{Si}_3 + \text{Ti}(\text{Si})$ at 1330 °C. The binary Nb-Si phase diagram has a eutectic of the form $L \rightarrow \text{Nb}_3\text{Si} + \text{Nb}(\text{Si})$ at 1880 °C and a peritectic of the form $L + \text{Nb}_5\text{Si}_3 \rightarrow \text{Nb}_3\text{Si}$ at 1980 °C. In the ternary phase diagram a eutectic trough extends between the two binary eutectics, but because of the different binary eutectic reactions there is a change in the nature of the liquidus surface and the eutectic trough with decreasing Nb and increasing Ti concentration. The binary phase diagram has been studied by several researchers [2, 3]. The eutectic occurs at a composition of Nb-18.2Si and a temperature of 1880 °C. The eutectic microstructure typically consists of Nb rods and ribbons with a width of ~2 µm in a Nb₃Si matrix. Although Ti₃Si and Nb₃Si are isomorphous, Nb₃Si is only stable over the temperature range 1880 to 1770 °C, and Ti₃Si is only stable below 1170 °C. Ti₃Si forms by a peritectoid reaction between Ti₅Si₃ and Ti.

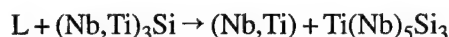
The details of the Nb-Ti-Si ternary are described here, and the substantiating data are presented in the following Results and Discussion section. The regions close to the Nb-Si and Ti-Si binary eutectics are straightforward. The loci of the peritectic ridge from the $L + \text{Nb}_5\text{Si}_3 \rightarrow \text{Nb}_3\text{Si}$ peritectic, the Ti-Ti₅Si₃ eutectic trough, and the locations of the two class II reactions that occur are more complex, and particular emphasis is placed on these features in the present section. For the purpose of the present discussion, a peritectic ($L + \text{Nb}_5\text{Si}_3 \rightarrow \text{Ti}_5\text{Si}_3$) is assumed between Nb₅Si₃ and Ti₅Si₃; a eutectic is also possible, but the evidence that will be discussed subsequently suggests a peritectic. However, either a eutectic or a peritectic reaction between Nb(Ti)₅Si₃ and Ti(Nb)₅Si₃ provides a groove towards the valley between the binary eutectics, as shown in Figure 3.4.1.

There are two options for the liquidus surface. In option 1 shown in Figure 3.4.2 (a), the first Class II reaction is described by:



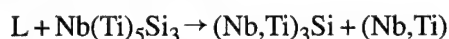
Thus, there is a peritectic groove ($L + \text{Nb}_5\text{Si}_3 \rightarrow (\text{Nb},\text{Ti})_3\text{Si}$) which extends from the Nb-rich side of the phase diagram and joins the peritectic groove of the reaction between Nb₅Si₃ and Ti₅Si₃ at ~1850 °C.

The second Class II reaction in option 1 is described by

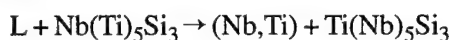


The above reaction occurs at the intersection between the peritectic ridge that descends from the first class II reaction and the (Nb,Ti)₃Si-(Nb,Ti) eutectic trough, as shown in the projection of the liquidus surface in Figure 3.4.1 at a temperature of ~1500 °C. The data that will be discussed subsequently indicate that this is the correct version of the liquidus surface. The steep nature of this peritectic ridge and the narrow composition range make it very difficult to determine unequivocally that option 1 is indeed correct.

The second option for the liquidus surface has the following first class II reaction:



In option 2 the peritectic ridge intersects the (Nb,Ti)₃Si + (Nb,Ti) eutectic trough leading to the above reaction, as shown in Figure 3.4.2(b). The trough continues to fall in temperature with increasing Ti until it meets the ridge from the peritectic reaction between Nb(Ti)₅Si₃ and Ti(Nb)₅Si₃, leading to the second Class II reaction:

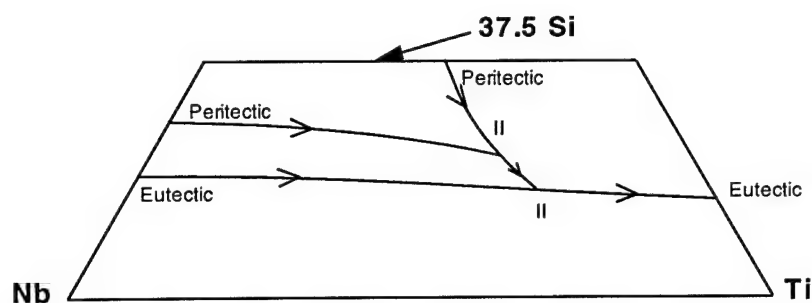


However, there was no evidence for this second class II reaction, as will subsequently be described.

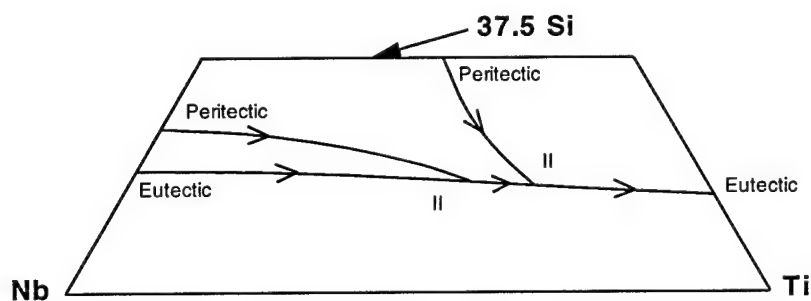
There are two other possible options in addition to the two described so far, with the second class II reaction being a ternary eutectic. However, there was no evidence for the formation of a ternary eutectic in any of the structures that were examined. There are no previous data on the compositions or temperatures at which the above Class II reactions occur. The aim of the present section is to describe the results of the phase equilibrium studies. These results are summarized in Figure 3.4.2(c) and indicate that the first of these two options is the correct version.

3.4.3 Experimental

The samples for phase equilibrium studies were directionally solidified by cold crucible directional solidification [2] after triple melting the starting charges from high purity elements (>99.9%). The directional solidification procedure used has been described previously [2]. In specific cases, samples were also prepared by cold crucible induction levitation melting followed by solidification in the cold crucible. The samples were examined using scanning electron microscopy (BSE) and energy dispersive spectrometry (EDS). In



(a)



(b)

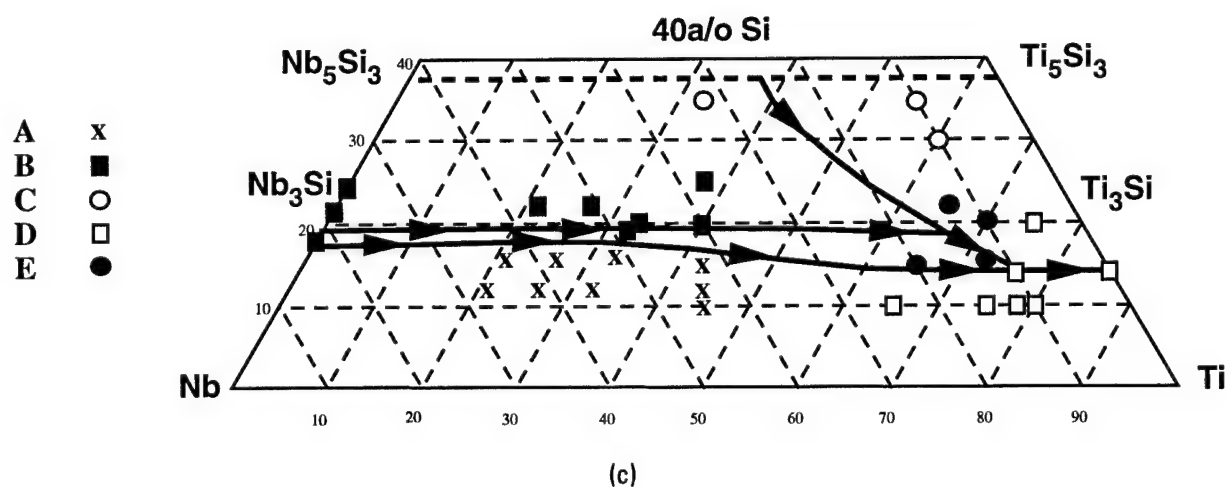


Figure 3.4.2. (a) Schematic diagram showing the projection of the liquidus surface for Option 1, (b) schematic diagram showing the projection of the liquidus surface for Option 2, and (c) actual compositions and constituent phases of the ternary phase diagram (the binary points are from previous studies [2,3]).

the case of selected alloys, electron beam microprobe analysis and X-ray diffraction (XRD) were also performed to differentiate the chemistry and crystal structure of the individual phases. Only compositions with Si concentrations less than 37.5% were considered.

The melt temperature was measured using a two wavelength optical pyrometer. The pyrometer was calibrated against both the melting temperature of 99.9% pure Ti (1670 °C) and the temperature of the Ti-Ti₅Si₃ eutectic (1330 °C). Errors in the temperature measurements were estimated as <20 °C. These temperatures were only approximate; liquidus and solidus temperatures were not measured because the melt temperatures were too high for conventional differential thermal analysis.

The compositions which were investigated are listed in Table 3.4.1. These compositions are those of the starting charges and not as analyzed after directional solidification. Mass losses were measured for each experiment and were found to be less than 0.1% weight percent.

3.4.4 Results and Discussion

Microstructures of Ternary Alloys

Microstructural evidence for the solidification paths will be discussed in the following order:

1. Nb-rich alloys
2. Nb₅Si₃ rich alloys
3. Nb₅Si₃-Ti₅Si₃
4. Ti-Ti₅Si₃ rich compositions
5. Compositions near the class II reactions.

These compositions are listed as A-E in Table 3.4.1 and the following sections.

Nb-Rich Nb-Ti-Si Compositions: Group A

Ternary Nb-Ti-Si alloys (Group A in Table 3.4.1) with Ti concentrations of 21-44% and Si concentrations of 12-16% were all on the metal-rich side of the Nb(Ti, Si)-(Nb,Ti)₃Si eutectic valley, so that the primary solidification phase was Nb(Ti, Si) dendrites. Typical microstructures of the longitudinal and transverse sections are shown in Figure 3.4.3 for the Nb-27%Ti-16%Si composition. The microstructure consisted of non-faceted Nb(Ti, Si) dendrites, which are the lighter phase in these BSE micrographs, together with large scale (~50 µm) faceted (Nb,Ti)₃Si dendrites; the microstructure of the longitudinal section shown in Fig-

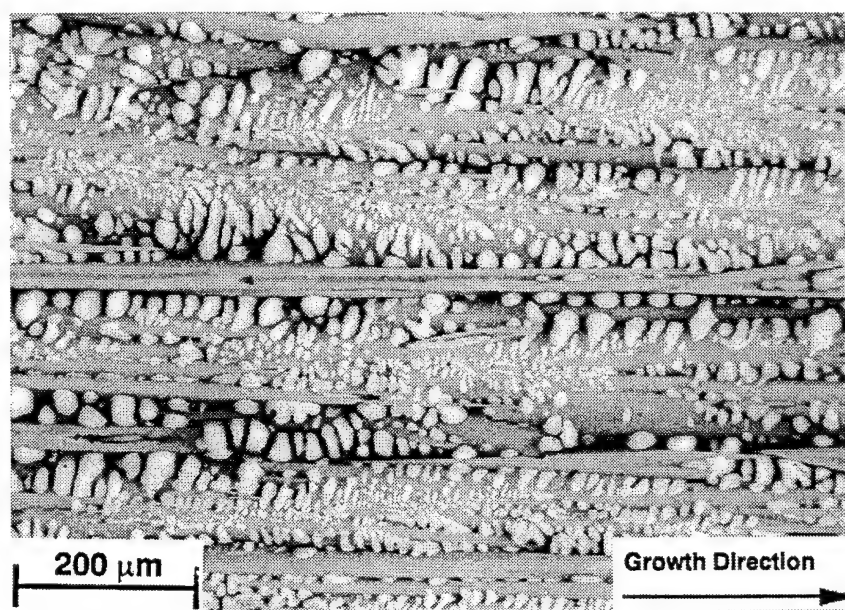
ure 3.4.3(a) indicates reasonable alignment of both non-faceted metal dendrites and faceted (Nb,Ti)₃Si dendrites with the growth direction. This composition was close to the eutectic trough. The BSE contrast indicates strong Ti segregation between the (Nb,Ti)₃Si cells. Typically, several samples were prepared from the individual compositions and the microstructures were observed to be very consistent. The phases present in the DS alloys are summarized in Table 3.4.1.

The microstructure of the transverse section of the DS composition Nb-21Ti-12Si is shown in Figure 3.4.4. The (Nb,Ti) dendrites are larger than in the case of the Nb-27Ti-16Si alloy, possibly because of the greater volume of metallic phase and the larger freezing range of the alloy (solidification begins at a higher point on the liquidus surface of the eutectic valley); this could have allowed some coarsening of the metal dendrites during directional solidification.

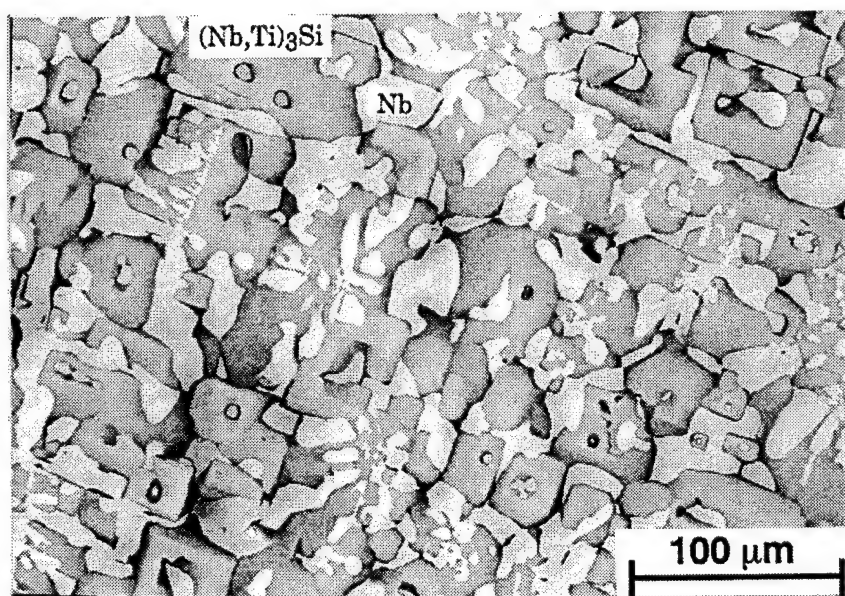
The final Nb-rich composition examined in this regime was Nb-44Ti-12Si. The microstructure of the transverse section of the DS composition is shown in Figure 3.4.5. This microstructure possessed a large volume fraction of non-faceted (Nb,Ti) dendrites. The interdendritic regions contained (Nb,Ti)₃Si and fine-scale (Nb,Ti). No Nb(Ti)₅Si₃ was observed in this microstructure, which suggested that the final composition of the inter-dendritic liquid was in the (Nb,Ti)-(Nb,Ti)₃Si eutectic trough and that it never reached a class II reaction. The eutectic trough temperature has fallen from ~1880 °C at the Nb-Si binary eutectic to ~1700 °C at Nb-42.5Ti-15Si. There is also a larger volume fraction of metal dendrites in the Nb-21Ti-12Si alloy than in the Nb-27Ti-16Si alloy; the volume fractions of metal dendrites for the Nb-27Ti-16Si and Nb-21Ti-12Si compositions were 41% and 54%, respectively. The lower volume fraction of metal was from the composition closer to the eutectic trough. This suggests that up to the 27Ti composition, the eutectic trough and the solvus surface are approximately parallel to the planes of constant Si composition, because the (Nb,Ti)₃Si essentially maintains the stoichiometric Si concentration. This is to be expected because there is only a small difference in the Si concentrations of the Nb-Nb₃Si and Ti-Ti₅Si₃ eutectics (Nb-18.2Si and Ti-13.5Si, respectively). However, the Nb-44Ti-12Si composition appears to have a larger volume fraction of metal dendrites. This could be because the eutectic trough is moving to Si-rich compositions with increasing Ti concentration, or because the solidus is moving towards the metal side of the ternary phase diagram

Table 3.4.1. Alloy compositions and constituent phases of the ternary Nb-Ti-Si alloys investigated.

Group	Composition	Constituent Phases	Melting Temperature (°C)
A	Nb-21Ti-12Si	Primary (Nb,Ti), Eutectic (Nb,Ti) ₃ Si+(Nb)	—
A	Nb-21Ti-16Si	Primary (Nb,Ti), Eutectic (Nb,Ti) ₃ Si+(Nb)	—
A	Nb-27Ti-12Si	Primary (Nb,Ti), Eutectic (Nb,Ti) ₃ Si+(Nb)	—
A	Nb-27Ti-16Si	Primary (Nb,Ti), Eutectic (Nb,Ti) ₃ Si+(Nb)	—
A	Nb-33Ti-12Si	Primary (Nb,Ti), Eutectic (Nb,Ti) ₃ Si+(Nb)	—
A	Nb-33Ti-16Si	Primary (Nb,Ti), Eutectic (Nb,Ti) ₃ Si+(Nb)	—
A	Nb-44Ti-12Si	Primary (Nb,Ti), Eutectic (Nb,Ti) ₃ Si+(Nb)	1712
A	Nb-45Ti-10Si	Primary (Nb,Ti), Eutectic (Nb,Ti) ₃ Si+(Nb)	1680
A	Nb-42.5Ti-15Si	Primary (Nb,Ti), Eutectic (Nb,Ti) ₃ Si+(Nb)	1704
B	Nb-21Ti-22Si	Primary Nb ₅ Si ₃ , Peritectic (Nb,Ti) ₃ Si, Eutectic (Nb,Ti) ₃ Si+ (Nb)	2030
B	Nb-27Ti-22Si	Primary Nb ₅ Si ₃ , Peritectic (Nb,Ti) ₃ Si, Eutectic (Nb,Ti) ₃ Si+(Nb)	2002
B	Nb-33Ti-20Si	Primary Nb ₅ Si ₃ , Peritectic (Nb,Ti) ₃ Si, Eutectic (Nb,Ti) ₃ Si+(Nb)	1870
B	Nb-40Ti-20Si	Primary Nb ₅ Si ₃ , Peritectic (Nb,Ti) ₃ Si, Eutectic (Nb,Ti) ₃ Si+ (Nb)	—
B	Nb-32Ti-19Si	Primary Nb ₅ Si ₃ , Peritectic (Nb,Ti) ₃ Si, Eutectic (Nb,Ti) ₃ Si+(Nb)	—
B	Nb-37.5Ti-25Si	Primary Nb ₅ Si ₃ , Peritectic (Nb,Ti) ₃ Si, Eutectic (Nb,Ti) ₃ Si+ (Nb)	—
C	Nb-32.5Ti-35Si	Primary Nb ₅ Si ₃ , Interdendritic (Nb,Ti) ₃ Si <i>No Metal</i>	2170
C	Nb-55Ti-35Si	Primary Ti ₅ Si ₃ , Eutectic Ti+Ti ₅ Si ₃	2020
C	Nb-60Ti-30Si	Primary Ti ₅ Si ₃ , Eutectic Ti+Ti ₅ Si ₃	1950
D	Si-86.5Ti	Eutectic Ti+Ti ₅ Si ₃	1328
D	Nb-76.5Ti-13.5Si	Eutectic Ti+Ti ₅ Si ₃	1355
D	Nb-65Ti-10Si	Primary (Nb,Ti), Eutectic Ti+Ti ₅ Si ₃	—
D	Nb-75Ti-10Si	Primary (Nb,Ti), Eutectic Ti+ Ti ₅ Si ₃	1550
D	Nb-78Ti-10Si	Primary (Nb,Ti), Eutectic Ti+Ti ₅ Si ₃	1513
D	Nb-80Ti-10Si	Primary (Nb,Ti), Eutectic Ti+Ti ₅ Si ₃	1480
D	Nb-75Ti-20Si	Primary Ti ₅ Si ₃ , Eutectic Ti+Ti ₅ Si ₃	—
E	Nb-65Ti-15Si	Primary (Nb, Ti) ₃ Si, Eutectic Nb ₃ Si+(Nb)	—
E	Nb-75Ti-15Si	Primary (Nb, Ti) ₃ Si, Eutectic Nb ₃ Si+(Nb), Eutectic Ti+ Ti ₅ Si ₃	1488
E	Nb-65Ti-22Si	Primary Ti ₅ Si ₃ , Peritectic Nb ₃ Si, Eutectic Nb ₃ Si+Nb, Eutectic Ti+ Ti ₅ Si ₃	1675
E	Nb-70Ti-20Si	Primary Ti ₅ Si ₃ , Peritectic Nb ₃ Si, Eutectic Nb ₃ Si+Nb, Eutectic Ti+ Ti ₅ Si ₃	1520



(a)



(b)

Figure 3.4.3. Typical microstructures of the (a) longitudinal and (b) transverse sections of a DS Nb-27Ti-16Si alloy.

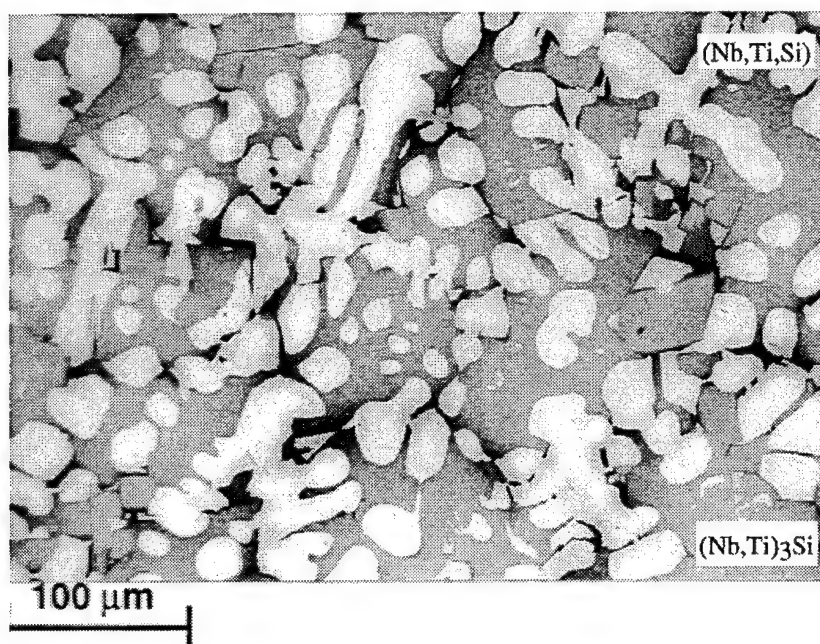


Figure 3.4.4. Typical microstructures of the transverse section of a DS Nb-21Ti-12Si alloy.

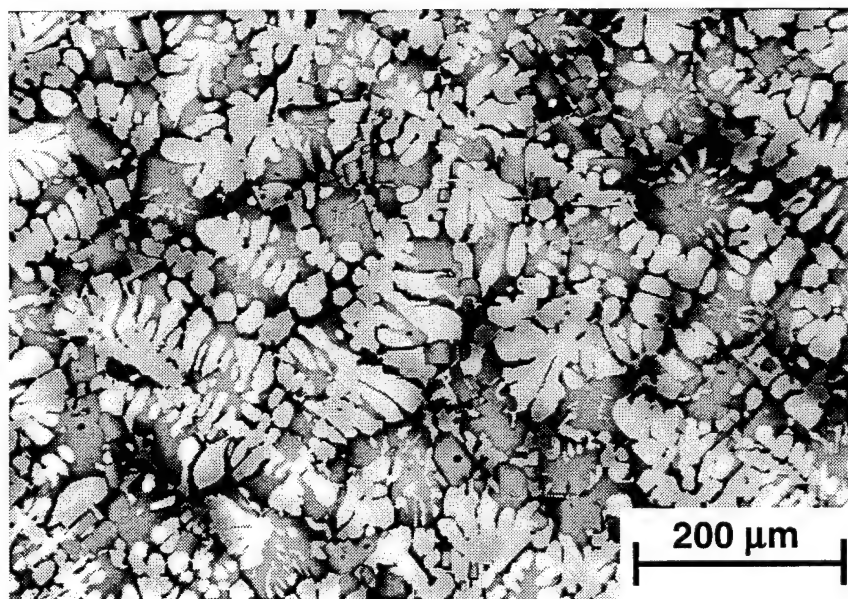


Figure 3.4.5. Typical microstructures of the transverse section of a DS Nb-44Ti-12Si alloy.

with increasing Ti concentration. The latter seems more likely, because the Ti-Ti₅Si₃ eutectic occurs at lower Si concentrations than the Nb-Nb₃Si eutectic. Thus, the locus of the eutectic trough shown in Figure 3.4.2(c) is consistent with the microstructures for compositions as low as 12%Si and as high as 44%Ti.

Nb(Ti)₅Si₃ Rich Compositions: Group B

A range of compositions was examined from the Nb(Ti)₅Si₃ and (Nb, Ti)₃Si rich side of the eutectic valley. In the binary Nb-Nb₃Si eutectic, the eutectic composition and the liquid composition of the L + Nb₅Si₃ → Nb₃Si peritectic are very close to each other (18.2 vs 19.5 Si). This is also the situation in the case of the Nb-Ti-Si ternary phase diagram. Therefore, it is very hard to define the region between the peritectic ridge and the eutectic groove. Nevertheless, there is clear evidence for the existence of such a region. The purpose of the present section is to describe the evidence for the range of Nb-Ti-Si compositions over which the peritectic ridge and the eutectic valley exist. It appears as though these two lines are within several per cent Si of each other and almost parallel to each other over a wide Ti composition, from 0 up to ~70Ti.

Ternary alloys with Ti concentrations of 21-40% and Si concentrations of 19-25% (group B in Table 3.4.1) were from the Si-rich side of the eutectic valley and were observed to have experienced the peritectic reaction, L + Nb(Ti)₅Si₃ → (Nb, Ti)₃Si. Microstructures of longitudinal and transverse sections of the DS Nb-27%Ti-22%Si composite are shown in Figure 3.4.6; these micrographs show the three phases expected for the hypereutectic compositions. First, there were metal-rich Nb(Ti, Si) dendrites; these were the lightest phase in the BSE images. Second, there were faceted (Nb, Ti)₃Si dendrites; these were the grey phase in the BSE images. Third, there was a small volume fraction of a dark phase, primary Nb(Ti)₅Si₃ dendrites. The longitudinal section showed aligned Nb(Ti, Si) and (Nb, Ti)₃Si dendrites, with primary Nb(Ti)₅Si₃ at the cores of the (Nb, Ti)₃Si dendrites. The presence of these phases was confirmed using electron probe microanalysis and EDS. The volume fraction of Nb(Ti)₅Si₃ was increased in alloys of higher Si concentrations. These structures are analogous to those which have been observed in hypereutectic binary DS Nb-Si composites [2]. In addition, BSE imaging showed strong dark contrast in the inter-dendritic regions of the Nb-Ti-Si alloys. This could have been due to the presence of a silicide or segregation of either Ti or Si to the inter-dendritic regions. EDS and microprobe analyses, as well

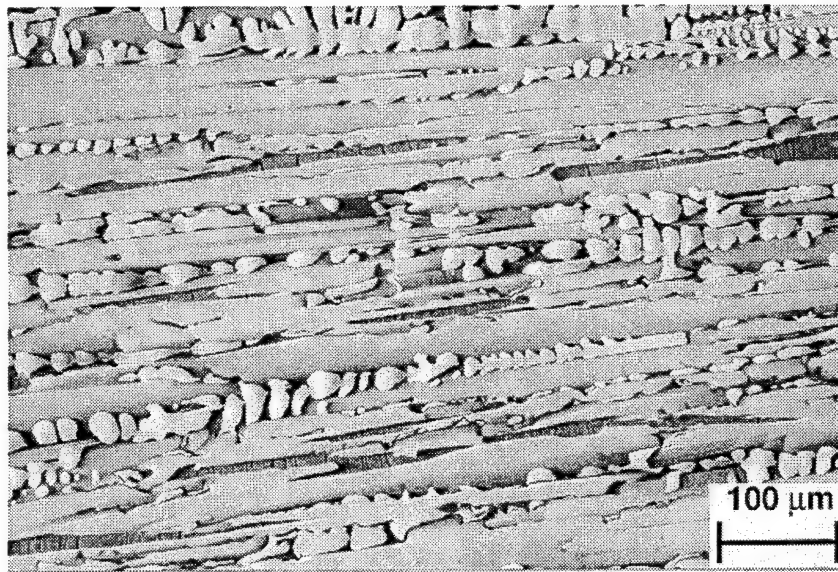
as crystallographic analyses using EBSP, indicated that this contrast was due to local Ti enrichment of (Nb, Ti)₃Si.

The longitudinal sections showed microcracks perpendicular to the growth direction in the Nb(Ti)₅Si₃ dendrites. These cracks probably occurred upon cooling as a result of an allotropic transformation of the Nb(Ti)₅Si₃ phase reported previously [2, 3]. Thus, for substitution of Nb by Ti for levels of up to 27%, the α to β Nb(Ti)₅Si₃ allotropic transformation still occurs. These cracks are very characteristic of the Nb₅Si₃ phase and help to distinguish it from other phases in the DS structure. No cracks were observed in the two-phase Nb(Ti, Si) and (Nb, Ti)₃Si composites.

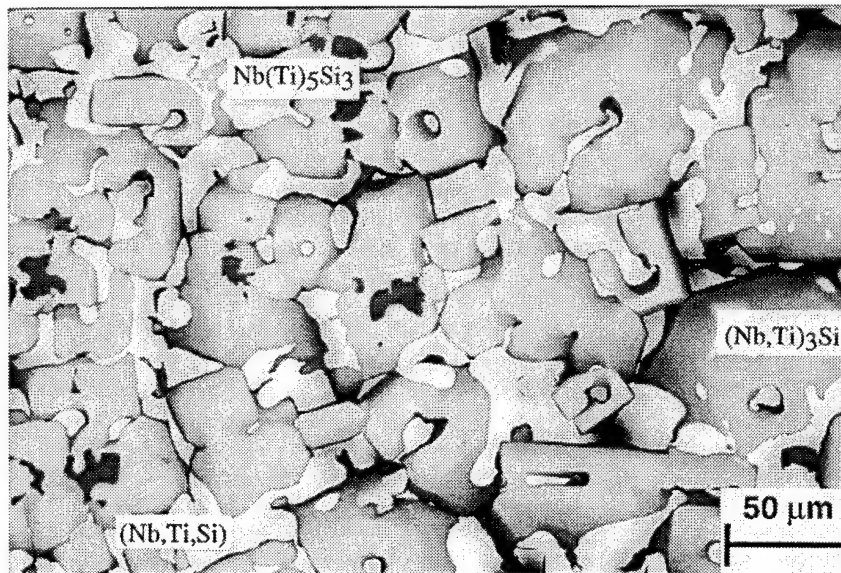
The highest Ti and Si containing alloys investigated in this regime were the Nb-40Ti-20Si and Nb-37.5Ti-25Si compositions. These both also contained primary Nb(Ti)₅Si₃, peritectic (Nb, Ti)₃Si, and inter-dendritic eutectic. In the Nb-37.5Ti-25Si there was a larger volume fraction of primary Nb(Ti)₅Si₃. This is evidence that the peritectic ridge extends to compositions as high as 40Ti; i.e., this composition is still richer in Nb than the Class II reaction, and the peritectic ridge is very close to the 20Si composition. At 33Ti, the peritectic temperature had fallen from ~1980 °C for the binary to ~1850 °C.

Compositions as low as 19%Si experienced the peritectic (i.e., were hyperperitectic) and compositions as high as 16% did not experience this reaction (i.e., they were hypoeutectic). This gives an indication of the narrow nature of the composition range between the Nb(Ti, Si)-(Nb, Ti)₃Si eutectic and the L + Nb(Ti)₅Si₃ → (Nb, Ti)₃Si peritectic.

A typical microprobe scan perpendicular to the dendrites of the DS Nb-27%Ti-22%Si composite is shown in Figure 3.4.6(c). The three phases can be differentiated chemically. The compositions of the three phases observed in the Nb(Ti, Si)-(Nb, Ti)₃Si-Nb(Ti)₅Si₃ composite are shown in Table 3.4.2. For the Nb(Ti, Si) solid solution, Nb, Ti and Si concentrations in the range 69 to 54, 29 to 44 and 1.6 to 2.4, respectively, were measured. A range of (Nb, Ti)₃Si chemistries was measured with different Nb and Ti ratios and a narrow range of Si concentrations. The centers of the faceted (Nb, Ti)₃Si dendrites were generally Nb rich and the shaded regions at the edges of these dendrites were Ti rich. The Si concentration of the (Nb, Ti)₃Si was slightly lean of the stoichiometric composition, which suggests that Ti substitutes principally for Nb and not Si. Nb(Ti)₅Si₃ was detected at the centers of the (Nb, Ti)₃Si dendrites and not in the inter-dendritic regions. The Si concen-



(a)



(b)

Figure 3.4.6. Typical microstructures of the (a) longitudinal and (b) transverse sections of a DS Nb-27Ti-22Si alloy.

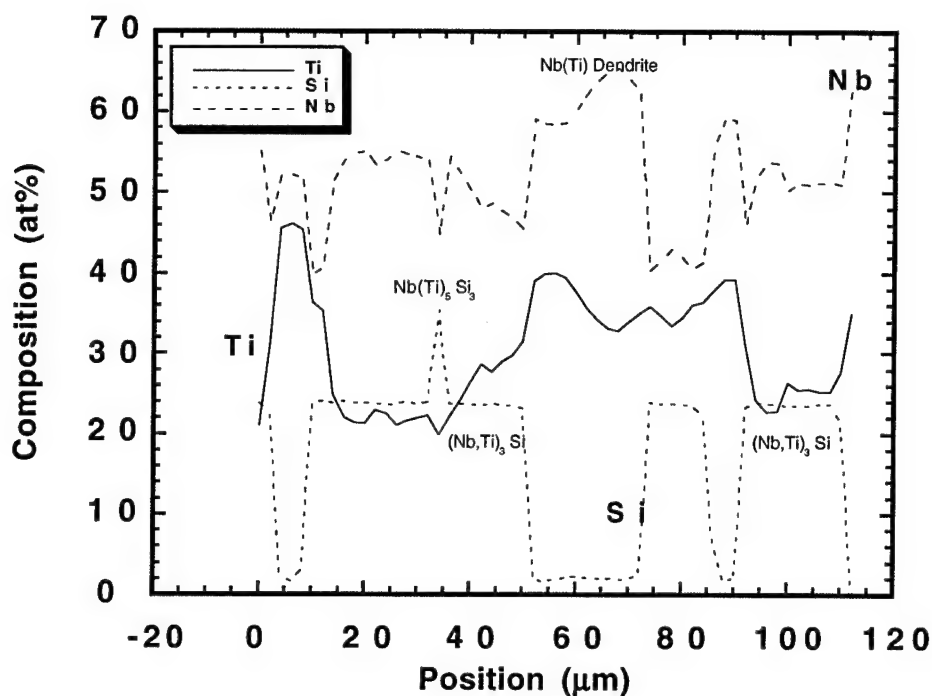


Figure 3.6.2 (c). Microprobe scans perpendicular to the growth direction showing the Nb, Ti, and Si concentration profiles perpendicular to the dendrites.

Table 3.4.2. Microprobe analyses of (Nb,Ti), (Nb,Ti)₃Si, and Nb(Ti)₅Si₃ phase composition ranges for the Nb-27Ti-22Si composite.

	Nb	Ti	Si	Comments
Nb (Ti, Si)	54-69	29-44	1.6-2.4	
(Nb,Ti) ₃ Si	38-40	37-38	23-24	Ti and Nb similar
	44-54	22-29	23-24	Nb-rich Ti-lean
	32-33	43-44	23.5	Ti-rich Nb-lean
Nb(Ti) ₅ Si ₃	44-45	19-20	35-36	

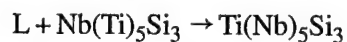
tration of the Nb(Ti)₅Si₃ was slightly lean of the stoichiometric composition.

Nb(Ti)₅Si₃ and Ti(Nb)₅Si₃ Rich Compositions: Group C

Nb-32.5Ti-35Si - Nb(Ti)₅Si₃ Rich Compositions

The microstructure of the Nb-32.5Ti-35Si is shown in Figure 3.4.7. This composition (part of group C in Table 3.4.1) was investigated in an attempt to identify the nature of the reaction between Nb(Ti)₅Si₃ and Ti(Nb)₅Si₃. The composition of 35%Si was selected in preference to 37.5%Si so that the solidification phases

formed would be metal-rich and not Si-rich. The microstructure consisted of primary Nb(Ti)₅Si₃ with inter-dendritic (Ti,Nb)₃Si (i.e., peritectic or eutectic). These phases were identified using EDS and XRD. The large gray blocky phase is Nb(Ti)₅Si₃ and the smaller inter-dendritic phase is (Ti,Nb)₃Si. This suggests that the reaction is a peritectic:



The evidence for the (Nb,Ti)₃Si phase is first, that it has the same morphology as Nb₃Si and second, that it provides lighter BSE contrast than the gray Nb(Ti)₅Si₃ phase; it therefore contains less Si or more Nb and Ti.

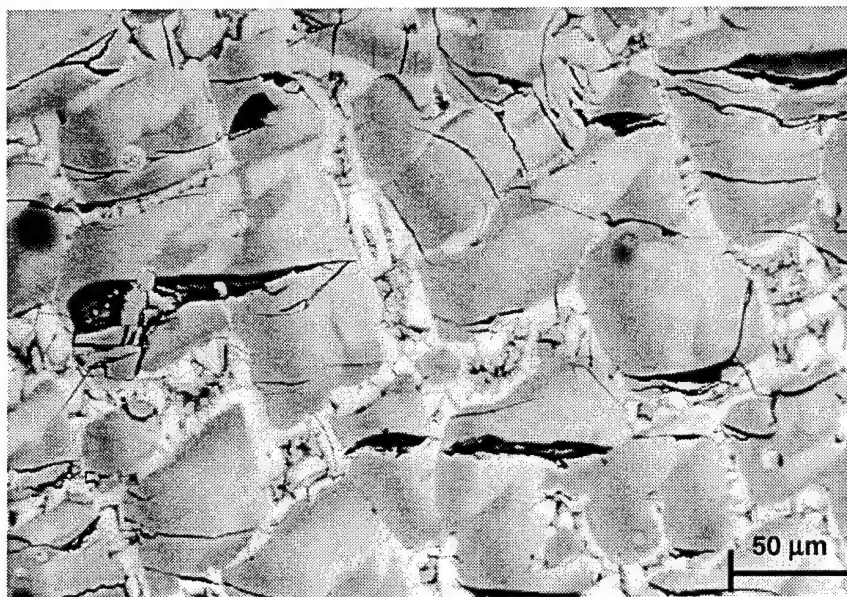


Figure 3.4.7. Typical microstructure of the induction melted Nb-32.5Ti-35Si alloy.

Given its faceted nature, it is almost certainly not a metallic phase, and it does not have either the appropriate morphology or BSE contrast to be a Ti_5Si_3 type phase; if it were a Ti_5Si_3 type phase, it would be darker than the gray phase and it would have a hexagonal rather than a tetragonal crystal structure. In addition, the poor contrast between the two phases is consistent with the phases being Nb_5Si_3 and Nb_3Si type phases rather than a silicide and metal, or niobium silicide and Ti_5Si_3 . However, the inter-dendritic regions are difficult to examine in detail. There may also be a very small volume fraction of a residual eutectic in the inter-dendritic regions. No metal dendrites were observed in this composition when it was examined using EDS and BSE.

The BSE contrast indicates that the $\text{Nb}(\text{Ti})_5\text{Si}_3$ -type dendrites are brightest in the center and there is segregation towards their periphery. These changes in contrast could be due to Nb depletion, Si enrichment, or Ti enrichment. The last is more likely, and the contrast gradation across the Nb_5Si_3 dendrites is consistent with the liquid composition moving away from the Nb_5Si_3 composition and towards the Ti corner, with the Si concentration probably remaining constant. EDS of the gray phase indicated that it is almost equiatomic in Nb, Ti, and Si; the evidence suggests that this phase is $\text{Nb}(\text{Ti})_5\text{Si}_3$.

Thus, the microstructure is consistent with $\text{Nb}(\text{Ti})_5\text{Si}_3$ being the primary solidification phase with the liquid composition shifting to the $\text{L} + \text{Nb}(\text{Ti})_5\text{Si}_3 \rightarrow (\text{Nb}, \text{Ti})_3\text{Si}$ peritectic ridge during solidification. This is a reason-

able explanation of the microstructure, but it does not prove that the reaction between $\text{Nb}(\text{Ti})_5\text{Si}_3$ and $\text{Ti}(\text{Nb})_5\text{Si}_3$ is a peritectic. However, if there were a eutectic reaction rather than a peritectic reaction between these two phases, it is more likely that a eutectic microstructure would have formed. The melting temperatures are 2520 °C for binary Nb_5Si_3 and 2130 °C for binary Ti_5Si_3 . The melting temperature of 2170 °C for the Nb-32.5Ti-35Si is consistent with a very flat peritectic liquidus. If there were a eutectic between these two phases, a lower melting temperature would be expected, below the melting temperature of Ti_5Si_3 . The trough would be steeper if the reaction was a eutectic and the liquid composition would shift into the eutectic valley.

Ti_5Si_3 -Rich Compositions

Nb-60Ti-30Si

The aim of examining this composition was first to try to solidify primary $\text{Ti}(\text{Nb})_5\text{Si}_3$ dendrites in order to determine their morphology and chemistry, and second, to attempt to examine the nature of the reaction between $\text{Nb}(\text{Ti})_5\text{Si}_3$ and $\text{Ti}(\text{Nb})_5\text{Si}_3$. The microstructure of the Nb-60Ti-30Si composition is shown in Figure 3.4.8. This sample was induction-melted and cast in the segmented cold crucible. The microstructure consisted of large-scale ($>100 \mu\text{m}$) primary Ti_5Si_3 dendrites in a $\text{Ti} - \text{Ti}_5\text{Si}_3$ eutectic. The microstructures of the Nb-60Ti-30Si and the Nb-75Ti-20Si compositions were similar. In these compositions the faceted hex-

agonal hP16 dendrites are clearly visible. The morphology and contrast are clear evidence that the silicide is $\text{Ti}(\text{Nb})_5\text{Si}_3$ and not $\text{Nb}(\text{Ti})_5\text{Si}_3$. Some cracks were observed in the $\text{Ti}(\text{Nb})_5\text{Si}_3$ dendrites of the induction cast samples; this was probably due to differential thermal contraction during solidification and post-solidification cooling.

The microstructure of the Nb-55Ti-35Si alloy was similar to that of the Nb-60Ti-30Si alloy in that it contained primary $\text{Ti}(\text{Nb})_5\text{Si}_3$ dendrites with an inter-dendritic eutectic of $\text{Ti}-\text{Ti}_5\text{Si}_3$. However, the volume fraction of primary $\text{Ti}(\text{Nb})_5\text{Si}_3$ was very large (>85%), and thus it was difficult to identify the faceted nature of the dendrites. At high magnifications the typical $\text{Ti}-\text{Ti}_5\text{Si}_3$ eutectic could be observed in the inter-dendritic regions. This suggests that on solidification the liquid composition moved over into the $\text{Ti}-\text{Ti}_5\text{Si}_3$ eutectic trough. The measured liquidus temperatures (1950 °C at 30Si and 2020 °C at 35Si) were lower than the melting temperature of binary Ti_5Si_3 .

Ti-Rich Compositions: Group D

The results from the Ti-rich corner of the ternary phase diagram are now discussed in the context of the results from the following compositions:

Ti-13.5%Si: Ti - Ti_5Si_3 Eutectic

The binary $\text{Ti}-\text{Ti}_5\text{Si}_3$ eutectic was examined and was confirmed as being at a composition of Ti-13.5% Si.

When grown at a rate of 2 mm/min, the eutectic consisted of very fine ($\sim 1 \mu\text{m}$) faceted needles in a Ti matrix. No primary Ti or Ti_5Si_3 dendrites were observed in the microstructure, and the eutectic grew with a cellular front. The eutectic was of a similar morphology to the inter-dendritic eutectic shown in Figure 3.4.8. These observations are consistent with previous reports of the binary $\text{Ti}-\text{Ti}_5\text{Si}_3$ eutectic by Crossman and Yue [5] and Wagner, et al. [6].

The $\text{Ti}-\text{Ti}_5\text{Si}_3$ can be distinguished from the $\text{Nb}-\text{Nb}_3\text{Si}$ eutectic by two characteristics. First, in the binary $\text{Ti}-\text{Ti}_5\text{Si}_3$ eutectic the Ti is the matrix, whereas in the binary $\text{Nb}-\text{Nb}_3\text{Si}$ the Nb_3Si is the matrix. Second, in the $\text{Ti}-\text{Ti}_5\text{Si}_3$ eutectic the Ti_5Si_3 rods are faceted, whereas in the $\text{Nb}-\text{Nb}_3\text{Si}$ eutectic the Nb rods are not faceted.

Nb-76.5Ti-13.5Si

In an attempt to identify the locus of the trough between the $(\text{Nb},\text{Ti})-(\text{Ti},\text{Nb})_3\text{Si}$ and $(\text{Ti},\text{Nb})-\text{Ti}(\text{Nb})_5\text{Si}_3$ eutectics more precisely, the Nb-76.5Ti-13.5Si composition was directionally solidified. This alloy had a melting temperature of 1355 °C. When grown at a rate of 2 mm/min, the microstructure consisted of very fine faceted needles ($\sim 2 \mu\text{m}$) of $\text{Ti}(\text{Nb})_5\text{Si}_3$ in a Ti matrix, the needles being aligned with the growth direction. No primary (Nb,Ti) , $\text{Ti}(\text{Nb})_5\text{Si}_3$, or $(\text{Ti},\text{Nb})_3\text{Si}$ dendrites were observed; this suggests that this composition was on the eutectic trough. We can, therefore, define three points on the eutectic trough: Nb-18.2% Si, Ti-13.5%

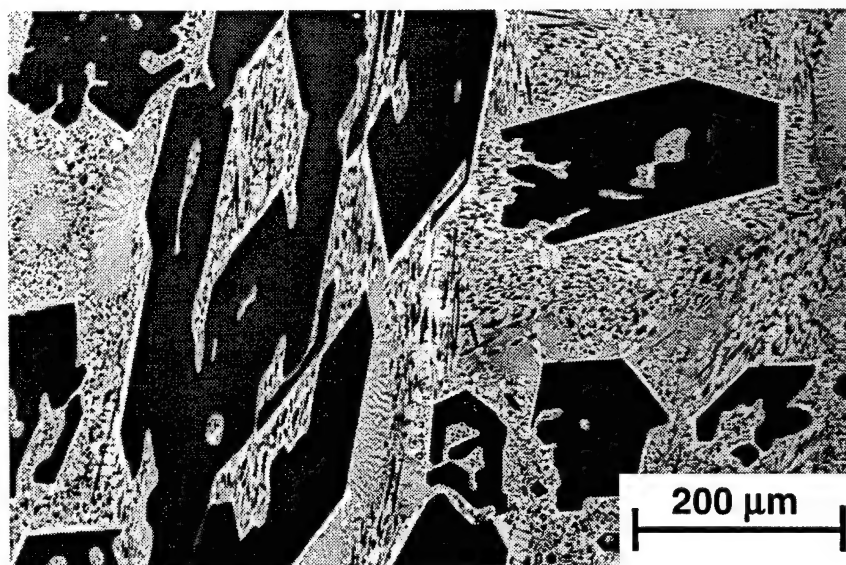


Figure 3.4.8. Typical microstructure of the induction melted Nb-60Ti-30Si alloy.

Si, and the Nb-76.5Ti-13.5Si. This also indicates that the second class II reaction occurs at a Ti composition of less than 76.5 and a Si concentration close to 13.5.

Nb-75Ti-10Si

The microstructure of the Nb-75Ti-10Si, shown in Figure 3.4.9, consists of primary (Nb,Ti) dendrites in a (Ti, Nb)- $\text{Ti}(\text{Nb})_5\text{Si}_3$ eutectic. In Figure 3.4.9 the large white dendrites are the (Ti,Nb), and the fine-scale ($\sim 1\ \mu\text{m}$) black needles are the $\text{Ti}(\text{Nb})_5\text{Si}_3$ of the eutectic. No (Nb, Ti) $_3\text{Si}$ was observed in these compositions. Figure 3.4.9 is the transverse section of a sample that was grown at 5 mm/min. Compositions of Nb-80Ti-10Si, Nb-78Ti-10Si, and Nb-75Ti-10Si were also examined, and the microstructures observed were similar. These compositions were directionally solidified in order to generate primary (Ti, Nb) dendrites with inter-dendritic Ti-Ti $_5\text{Si}_3$ eutectic to confirm the existence of the Ti-Ti $_5\text{Si}_3$ eutectic and identify the locus of the eutectic trough. One can therefore infer that in this region the primary solidification phase was (Nb,Ti) dendrites, the liquid composition moves away from the Nb-rich corner towards the eutectic trough where the Ti-Ti $_5\text{Si}_3$ eutectic is formed, and then the liquid composition moves down the eutectic trough. No ternary eutectic was observed. In some areas the Ti-Ti $_5\text{Si}_3$ looked lamellar and in others it looked like individual "sheafs" with a fine Ti $_5\text{Si}_3$ rod at the center of the "sheafs." The Nb-75Ti-10Si, Nb-80Ti-10Si, and Nb-78Ti-10Si compositions were self consistent. The Nb-75Ti-10Si was directionally solidified three times and the microstructure was consistent in each case.

In order to check the nature of the eutectic, the Nb-75-10Si composition was grown with a Nb-27Ti-16Si seed; this seed possessed (Nb,Ti) dendrites and (Nb,Ti) $_3\text{Si}$, as described previously. The metal dendrites grew from the Nb-75Ti-10Si melt epitaxially off the seed, but the $\text{Ti}(\text{Nb})_5\text{Si}_3$ did not grow epitaxially. The (Nb,Ti)-Ti $_5\text{Si}_3$ eutectic also clearly possessed a different chemistry and provided a much darker BSE contrast than the (Nb,Ti) $_3\text{Si}$ (in the seed) at the seed:Nb-75Ti-10Si interface. If it were at all possible to grow (Nb,Ti) $_3\text{Si}$ from this composition, it would have nucleated and grown easily on the seed.

Nb-75Ti-20Si

The aim of examining this composition (from group D in Table 3.4.1) was first to try to directionally solidify primary $\text{Ti}(\text{Nb})_5\text{Si}_3$ dendrites under controlled conditions in order to determine their morphology and chemistry, second, to attempt to examine characteristics of the Ti-Ti $_5\text{Si}_3$ eutectic, and third to examine the nature of the phase equilibria between the two class II reactions.

The microstructure of the transverse section of the DS Nb-75Ti-20Si alloy, shown Figure 3.4.10, consisted of only two phases, $\text{Ti}(\text{Nb})_5\text{Si}_3$ and (Ti, Nb). It was of the hypereutectic composition giving rise to primary large-scale black primary Ti $_5\text{Si}_3$ dendrites and a (Ti, Nb)- $\text{Ti}(\text{Nb})_5\text{Si}_3$ eutectic. The faceted, hexagonal black $\text{Ti}(\text{Nb})_5\text{Si}_3$ dendrites are clearly visible. The eutectic consisted of very fine ($\sim 1\ \mu\text{m}$) faceted hexagonal black $\text{Ti}(\text{Nb})_5\text{Si}_3$ rods in a (Ti, Nb) matrix; this can be seen

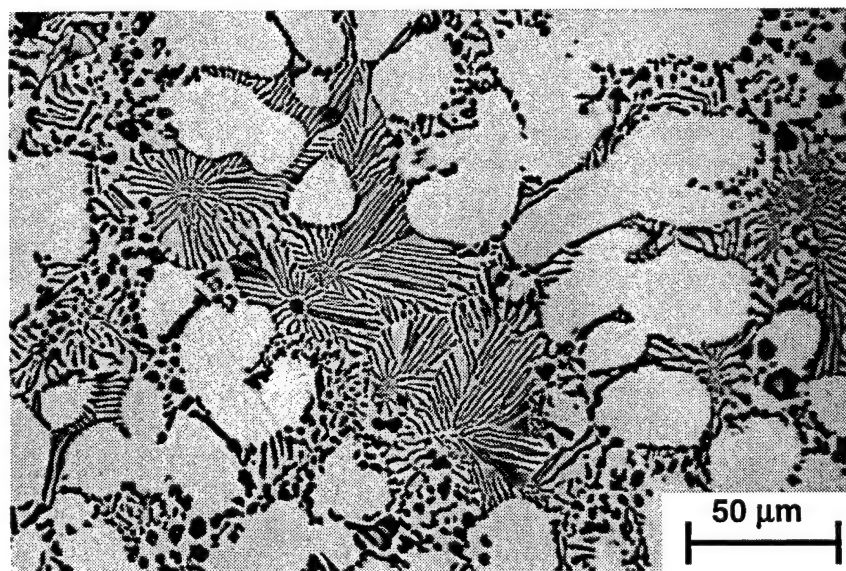
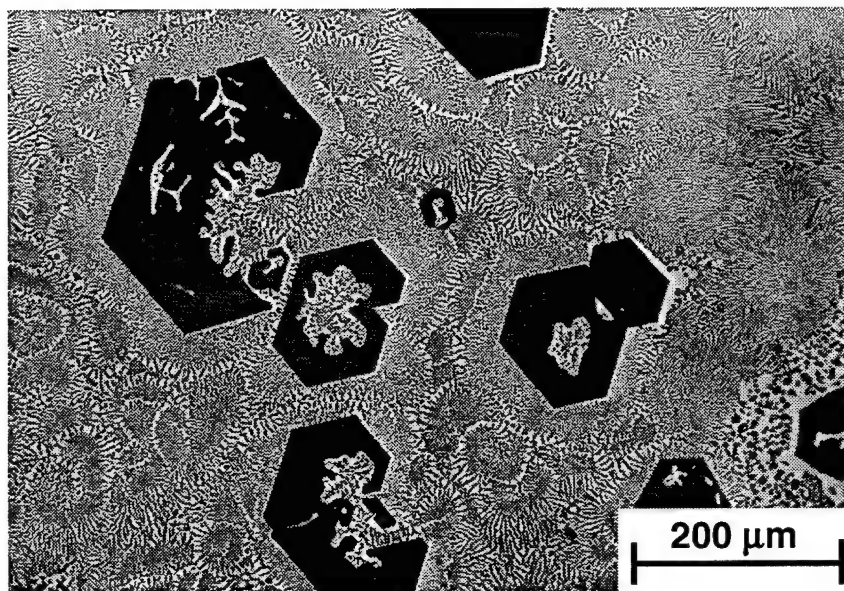
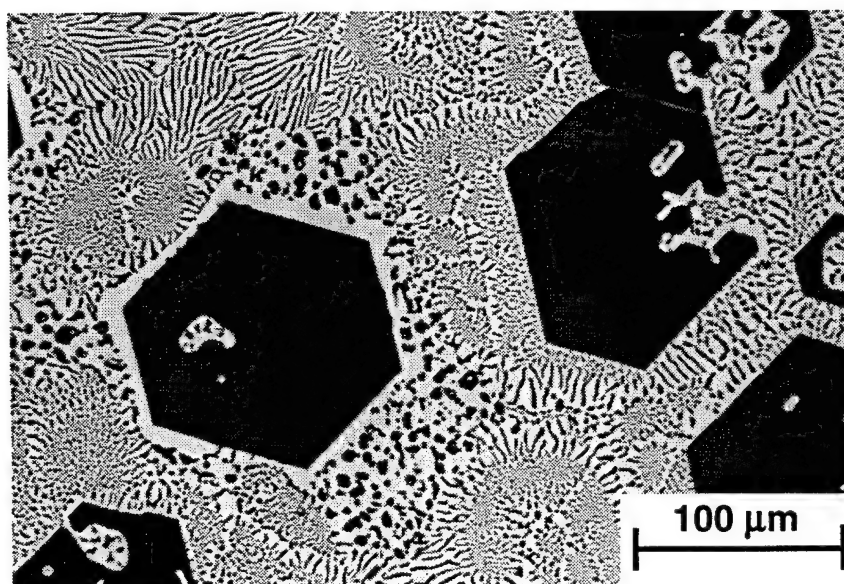


Figure 3.4.9. Typical microstructure of the transverse section of a DS Nb-75Ti-10Si alloy.



(a)

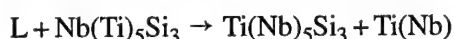


(b)

Figure 3.4.10. Typical microstructures of the transverse section of a DS Nb-75Ti-20Si alloy, at low (a) and high (b) magnifications, showing the primary $\text{Ti(Nb)}_5\text{Si}_3$ faceted dendrites, and inter-dendritic eutectic $(\text{Ti,Nb})\text{-Ti(Nb)}_5\text{Si}_3$.

more clearly in Figure 3.4.10(b). The morphology of the eutectic did not appear to have been modified by the Nb additions. Eutectic cells are also clearly visible in the inter-dendritic regions. This behavior is quite distinct from the Nb-rich compositions of the same Si concentration where a peritectic reaction occurs. Thus, the microstructure of the Nb-70Ti-20Si indicates that the peritectic ridge had terminated at Ti compositions between 40 and 70Ti. The Nb-75Ti-20Si composition is sufficiently far away from the class II reaction that the solidification path can take the liquid composition to the (Ti, Nb)-Ti(Nb)₅Si₃ eutectic trough, whereas in the case of the Nb-70Ti-20Si composition, discussed subsequently, the composition is close to the peritectic ridge between the two class II reactions and the microstructure is dramatically different.

There was no evidence of a ternary eutectic in any of the alloys examined. The Ti-rich compositions are also consistent with the second class II reaction being of the form :



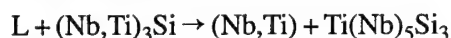
Compositions Near Class II Reactions: Group E

Nb-75Ti-15Si

The microstructure of the transverse section of the DS Nb-75Ti-15Si composition (group E in Table 3.4.1) is shown in Figure 3.4.11. There are three distinct features of this microstructure. First, there are large blocky

gray (Nb, Ti)₃Si dendrites; these generally are of the typical faceted form and they have a width of ~30 μm. Second, the majority of the microstructure consists of eutectic cells with distinct cell boundaries. These cells contain a two-phase microstructure of gray (Nb, Ti)₃Si and white (Nb, Ti). It appears as though the metallic phase is continuous. Third, at the intercellular boundaries there is a very small volume fraction of a two-phase, fine-scale eutectic of Ti(Nb)₅Si₃ and (Nb, Ti); this was probably generated from the final liquid to solidify. The (Ti,Nb)-Ti(Nb)₅Si₃ can be clearly distinguished from the (Nb, Ti)-(Nb, Ti)₃Si by its morphology, scale, and contrast. In regions where there was a large volume fraction of Ti-Ti₅Si₃ eutectic it possessed a lamellar morphology.

This microstructure suggests that the Nb-75Ti-15Si composition lies in between the $L + \text{Nb}(\text{Ti})_5\text{Si}_3 \rightarrow (\text{Nb}, \text{Ti})_3\text{Si}$ peritectic ridge and the Nb-Nb₃Si eutectic trough; this explains the presence of the primary Nb₃Si dendrites. The presence of the intercellular (Ti,Nb)-Ti(Nb)₅Si₃ eutectic is evidence for the existence of the second class II reaction:



It also suggests that a ternary eutectic is not present. This composition is very close to the second class II reaction and the eutectic trough. It is from the hypereutectic side rather than the hypoeutectic side; no primary metal dendrites were observed.

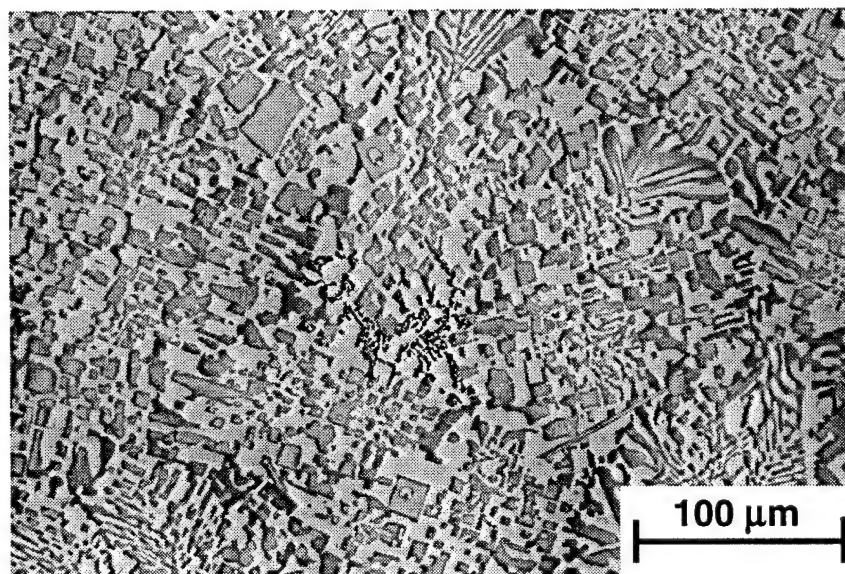


Figure 3.4.11. Typical microstructure of the transverse section of a DS Nb-75Ti-15Si alloy.

Nb-65Ti-15Si

The microstructure of the Nb-65Ti-15Si was similar to that of the Nb-75Ti-15Si with the exception of the following features: First, it contained a slightly larger volume fraction of primary (Nb, Ti)₃Si dendrites, and second, there was no evidence of any Ti-Ti₅Si₃ eutectic. Again the (Nb,Ti) was the continuous phase of the eutectic cells. It is somewhat unusual that the primary (Nb, Ti)₃Si dendrites are generally at the intercellular boundaries. This may be just an artifact of the large volume fraction of cellular eutectic. The dendrites were much more evident in this alloy; the longitudinal section showed some alignment of the primary (Nb, Ti)₃Si dendrites, but not the inter-dendritic cellular eutectic. The eutectic grew within distinct cells which had a diameter of ~250 μ m. This evidence suggests that the Nb-65Ti-15Si composition is in the two-phase L + (Nb, Ti)₃Si regime on the hypereutectic side of the eutectic valley, but the composition is very close to the eutectic trough. The implication is that this composition is further up the (Nb, Ti)₃Si-(Nb, Ti) eutectic valley than the Nb-75Ti-15Si composition and that the composition of the residual intercellular liquid never reached the composition of the second class II reaction.

Nb-70Ti-20Si

The purpose of examining this composition was to determine the position and nature of the peritectic (L + Ti(Nb)₅Si₃ \rightarrow Nb₃Si) ridge between the two class II reactions. A micrograph of the transverse section of

the DS Nb-70Ti-20Si is shown in Figure 3.4.12. Although there were only three phases present in this composition, five distinct morphologies were observed. First, there were hexagonal, black, faceted Ti(Nb)₅Si₃ dendrites. These were identified using EDS as being the Ti(Nb)₅Si₃ rather than the Nb(Ti)₅Si₃ type. The second phase is peritectic (Nb,Ti)₃Si, which can be seen growing in a peritectic-type manner from the Ti(Nb)₅Si₃ dendrites. Again, the (Nb,Ti)₃Si was identified by both its faceted morphology and its chemistry. The third feature was the grey eutectic (Nb,Ti)₃Si phase, which existed as eutectic-type cells together with the fourth feature, the white (Nb,Ti) metallic phase. Fifth, there was a fine-scale (Nb,Ti)-Ti(Nb)₅Si₃ eutectic within the intercellular regions generated by the (Nb,Ti)₃Si-(Nb,Ti) eutectic cells. EDS indicated that the chemistry of the eutectic Ti(Nb)₅Si₃ was similar to that of the larger scale primary Ti(Nb)₅Si₃.

Thus, the first phase to solidify was primary Ti(Nb)₅Si₃. This suggests that this composition is from the Ti₅Si₃ rich region, as shown in Figure 3.4.2(c). It is also evidence for the second class II reaction. No ternary eutectic was observed in this composition. The microstructure also suggests that the Nb-70Ti-20Si composition is very close to the L + Ti(Nb)₅Si₃ \rightarrow (Nb,Ti)₃Si peritectic ridge. Thus, the liquid composition shifted during solidification and met the peritectic ridge just below the first class II reaction and led to the solidification of peritectic (Nb,Ti)₃Si on the primary Ti(Nb)₅Si₃. However, the liquid composition only followed the

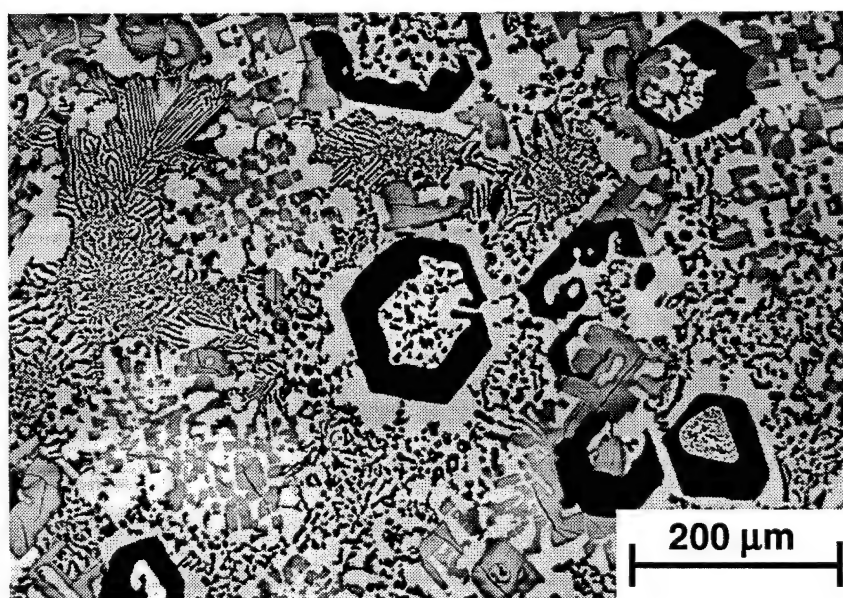


Figure 3.4.12. Typical microstructure of the transverse section of a DS Nb-70Ti-20Si alloy.

peritectic ridge for a short distance and it dropped off this ridge into the lower hypereutectic corner of the eutectic (Nb,Ti)-(Nb,Ti)₃Si valley. This led to solidification of cells of the latter eutectic. The liquid composition continued to move down the eutectic (Nb,Ti)-(Nb,Ti)₃Si valley and it eventually reached the second class II reaction where the remaining liquid in the intercellular regions solidified as Ti(Nb)₅Si₃-(Nb,Ti) eutectic. The microstructures also suggest that the reaction between Nb(Ti)₅Si₃ and Ti(Nb)₅Si₃ is not a eutectic; if it were, it seems likely that at least some Nb(Ti)₅Si₃ and Ti(Nb)₅Si₃ eutectic would be observed in between the primary Ti(Nb)₅Si₃ dendrites.

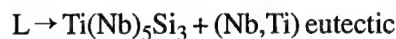
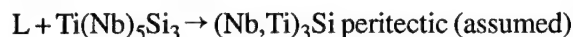
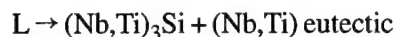
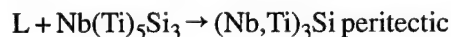
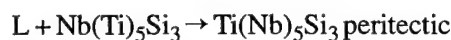
Nb-65Ti-22Si

This composition was from a similar region to the Nb-70Ti-20Si, but it was further from the peritectic ridge and therefore possessed a higher melting temperature (1675 vs. 1520 °C); the melting temperature of the binary Ti₅Si₃ is 2130 °C. Again, there were five distinct features of the microstructure: primary Ti(Nb)₅Si₃ dendrites, peritectic (Nb,Ti)₃Si, (Nb,Ti), (Nb,Ti)₃Si-(Nb,Ti) eutectic cells, and Ti(Nb)₅Si₃-(Nb,Ti) eutectic. However, there was a much smaller volume fraction of Ti(Nb)₅Si₃-(Nb,Ti) eutectic in the Nb-65Ti-22Si than in the Nb-70Ti-20Si. This composition probably met the $L + \text{Ti(Nb)}_5\text{Si}_3 \rightarrow (\text{Nb,Ti})_3\text{Si}$ peritectic ridge below the first class II reaction, and followed a similar solidification path to that of the Nb-70Ti-20Si. In some regions the large scale (Nb,Ti)₃Si peritectic can be seen to have consumed the primary Ti(Nb)₅Si₃.

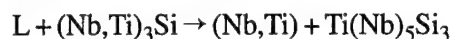
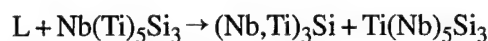
3.4.5 Conclusions

The microstructures generated in the ternary Nb-Ti-Si alloys investigated contained four phases: (Nb,Ti), Nb(Ti)₅Si₃, (Nb,Ti)₃Si, and Ti(Nb)₅Si₃. The phases that were observed were either dendritic, peritectic, or eutectic in their scale and morphology, depending on the composition and solidification path. These phases can be clearly distinguished in the microstructures by their scale, morphology, and chemistry.

Microstructural and chemical evidence indicates that the liquidus surface of the Nb-Ti-Si ternary phase diagram possesses the following reactions:



These reactions give rise to the following class II reactions:



The first of these class II reactions occurs at a composition of approximately Nb-66Ti-19Si, and probably at a temperature between 1600 and 1650 °C. The second of these class II reactions occurs at a composition of approximately Nb-76Ti-13.5Si and a temperature of ~1350 °C. No ternary eutectic was observed in the compositions that were investigated. Further studies of the solid-state phase equilibria are planned.

3.4.6 References for Section 3.4

- [1] P.R. Subramanian, M.G. Mendiratta, and D.M. Dimiduk, *Mat. Res. Soc. Symp. Proc.*, 322 (1994), pp. 491-502.
- [2] B.P. Bewlay, M.R. Jackson, W.J. Reeder, and H.A. Lipsitt, *MRS Proceedings on High Temperature Ordered Intermetallic Alloys VI*, Vol. 364, 1995, pp. 943-948.
- [3] T.B. Massalski, *Binary Alloy Phase Diagrams*, ASM Metals Park, Ohio (1991).
- [4] M.R. Jackson, R.G. Rowe, and D.W. Skelly, Annual Report, *WRDC Contract # F33615-91-C-5613* (1994).
- [5] F.W. Crossman and A.S. Yue, *Metall. Trans.* 2, 1971, pp. 1545-1555.
- [6] R. Wagner, M. Es-Souni, D. Chen, B. Dogan, J. Seeger and P.A. Beaven, *Mat. Res. Soc. Symp. Proc.*, 213 (1991), pp. 1007-1012.

4. Future Work

This program has investigated toughening mechanisms in high-strength DS composites with melting temperatures above 1600 °C, and has successfully demonstrated methods for toughness enhancement in this class of materials. This work has included studies of a range of composites from binary Nb-Si alloys, ternary Nb-Ti-Si alloys, and also higher order alloys containing Nb, Si, Ti, Hf, Cr, and Al. Composites of these chemistries have displayed an attractive balance of high- and low-temperature mechanical properties with promising oxidation resistance.

In addition to fracture toughness, other properties, such as creep and oxidation resistance, need to be investigated in this class of high-temperature materials, since

these properties are critical for high-temperature applications; implementation of intermetallic-based composites depends on developing an improved fundamental understanding of these properties. Although this study has developed several silicide-based composites with promising creep behavior, further studies of the mechanisms controlling creep behavior are required. Possible areas for further study of creep mechanisms in this class of materials include the effect of the metallic phase strength, the role of the volume fraction of intermetallic, the role of the intermetallic strength, and the effect of the texture and grain size of both the metallic and intermetallic phases. These contributions will lead to the scientific bases needed for further enhancement of the property balance in this class of materials.

5.0 Publications and Presentations

5.1 1996 Publications

The following is a list of articles published in the contract period April 1995 to March 1996:

1. B.P. Bewlay, H.A. Lipsitt, M.R. Jackson, W.J. Reeder, and J.A. Sutliff, "Solidification Processing of High Temperature Intermetallic-Based Eutectic Alloys," *Materials Science and Engineering*, A192/193 (1995), pp. 534-543.
2. J. A. Sutliff, B.P. Bewlay, and M.R. Jackson, "Microstructure and Microtexture of Directionally Solidified or Extruded Nb-Nb₅Si₃ In-Situ Composites," *Proceedings of the 53rd Annual Meeting of the Microscopy Society of America*, Ed. G.W. Bailey and A.J. Garret-Reed, San Francisco Press, 1995, p. 123.
3. "On the Nature of Faults in MoSi₂," B. K. Kad, K. S. Vecchio, R. J. Asaro, and B. P. Bewlay, *Phil. Mag.* A72 (1), July 1995, pp. 1-19.
4. B.P. Bewlay and M.R. Jackson, "The Effect of Hf and Ti Additions on Microstructure and Properties of Cr₂Nb-Nb In-Situ Composites," accepted for *Journal of Materials Research*, April 1996.
5. B.P. Bewlay, W.J. Reeder, H.A. Lipsitt, M.R. Jackson, and J.A. Sutliff, "Toughness Enhancements In Intermetallic-Based Composites: Processing and Properties," to be published in *Processing and Fabrication of Advanced Materials for High Temperature Applications V*, Ed. T.S. Srivatsan and J.J. Moore, TMS Publications, 1996.
6. M.R. Jackson, B.P. Bewlay, R.G. Rowe, D.W. Skelly, and H.A. Lipsitt, *Journal of Metals* 46 (1), pp. 39-44, January 1996.
7. G. A. Henshall, M. J. Strum, B. P. Bewlay, and J. A. Sutliff, "The Influence of Chemistry and Microstructure on the Fracture Toughness of V-V₃Si In-Situ Composites," in *Processing and Fabrication of Advanced Materials for High Temperature Applications IV*, Eds. V.A. Ravi, T.S. Srivatsan, and J.J. Moore, TMS Publications, 1995.
8. J. A. Sutliff and B. P. Bewlay, "Orientation Imaging of a Nb-Ti-Si DS In-Situ Composite," to be published in the *Proceedings of the 54rd Annual Meeting of the Microscopy Society of America*, Ed. G.W. Bailey and A.J. Garret-Reed, San Francisco Press, 1995.

ing of the Microscopy Society of America," Ed. G.W. Bailey and A.J. Garret-Reed, San Francisco Press, 1995.

5.2 1995 Publications

The following is a list of articles published in the contract period April 1994 to March 1995:

1. B.P. Bewlay, J.A. Sutliff, M.R. Jackson, and H.A. Lipsitt, "Microstructural and Crystallographic Relationships in Directionally Solidified Nb-Cr₂Nb and Cr-Cr₂Nb Eutectics," *Acta Metall. Mater.* Vol. 42 (8), 1994, pp. 2869-2878.
2. B.P. Bewlay, M.R. Jackson, W.J. Reeder, and H.A. Lipsitt, "Microstructures and Properties of DS In-Situ Composites of Nb-Ti-Si Alloys," *MRS Proceedings on High Temperature Ordered Intermetallic Alloys VI*, Vol. 364, 1995, pp. 943-948.
3. B.P. Bewlay, H.A. Lipsitt, W.J. Reeder, M.R. Jackson, and J.A. Sutliff, "Toughening Mechanisms in Directionally Solidified Nb-Si In-Situ Composites," in *Processing and Fabrication of Advanced Materials for High Temperature Applications III*, Ed. V.A. Ravi, T.S. Srivatsan, and J.J. Moore (Warrendale, Pa: TMS Publications, 1994), pp. 547-565.
4. J. A. Sutliff, B.P. Bewlay, G. A. Henshall, and M. J. Strum, "Facet Crystallography of Fractured V (2.7%Si) Solid Solution," *Proceedings of the 52nd Annual Meeting of the Microscopy Society of America*, Ed. G.W. Bailey and A.J. Garret-Reed, San Francisco Press, 1994, p. 622.
5. M.R. Jackson, R. G. Rowe, and D. W. Skelly, "Oxidation of Some Intermetallic Compounds and Intermetallic Matrix Composites," *MRS Proceedings on High Temperature Ordered Intermetallic Alloys VI*, Vol. 364, 1995, pp. 1339-1344.

5.3 1994 Publications

The following is a list of articles published in the contract period March 1993 to April 1994:

1. B.P. Bewlay, J.A. Sutliff, K-M Chang, M.R. Jackson, "Microstructure, Phase Equilibria and Proper-

ties of Cr-Si, Nb-Si and V-Si Binary Eutectics," in *Processing and Fabrication of Advanced Materials for High Temperature Applications*, Ed. V.A. Ravi and T.S. Srivatsan (Warrendale, Pa: TMS Publications, 1993), 209-222.

2. J.A. Sutliff, B.P. Bewlay, and H.A. Lipsitt, "High Temperature Phase Equilibria in Cr-Cr₃Si Two Phase Alloys," *Journal of Phase Equilibria*, Oct. 1993, Vol. 14 (5), 1993, pp. 89-110.
3. B.P. Bewlay, J.A. Sutliff, K-M. Chang, M.R. Jackson, "Processing, Microstructures and Properties of Cr-Cr₃Si, Nb-Nb₃Si and V-V₃Si Eutectics," *Materials and Manufacturing Processes*, Vol. 8 (3), 1993, pp. 583-587.
4. M. J. Strum, B. P. Bewlay, G. A. Henshall, J. A. Sutliff, and M. R. Jackson, "The Effects of In-Situ Processing Methods on the Microstructure and Fracture Toughness of V-V₃Si Composites," *MRS Proceedings*, Vol. 322, 1993, pp. 511-516.
5. B. K. Kad, K. S. Vecchio, B. P. Bewlay, and R. J. Asaro, "C11_B-C40 Transformation-Induced 1/4<111> Faults in MoSi₂," *MRS Proceedings*, Vol. 322, pp. 49-55.
6. C.L. Briant, J.J. Petrovic, B.P. Bewlay, A.K. Vasudevan, and H.A. Lipsitt, "High Temperature Silicides and Refractory Alloys," *MRS Proceedings*, Vol. 322, 1994.

5.4 Presentations

During the course of this contract a large number of presentations of invited and contributed papers have been given at international conferences and workshops. The most recent of these presentations are listed below:

1. "Toughness Enhancements In Intermetallic-Based Composites: Processing and Properties," B.P. Bewlay, W.J. Reeder, H.A. Lipsitt, M.R. Jackson, and J.A. Sutliff, presented at the TMS meeting on "Processing and Fabrication of Advanced Materials for High Temperature Applications V," October 1995.
2. "Directionally Solidified High Temperature in-Situ Composites," B.P. Bewlay, H.A. Lipsitt, M.R. Jackson, Engineering Foundation Conference on "Processing and Design Issues in High Temperature Materials," Davos, Switzerland, May 1996 (Invited talk).
3. "Orientation Imaging of a Nb-Ti-Si DS In-Situ Composite," J.A. Sutliff and B.P. Bewlay, to be presented at the *54rd Annual Meeting of the Microscopy Society of America*, 1995.
4. "Microstructures and Properties of DS Intermetallic-Based Composites," MRS Conference on High Temperature Ordered Intermetallic Alloys VII, December 1996 (Invited talk).

6. Personnel Qualifications

6.1 Program Organization

The principal investigator is Dr. Bernard P. Bewlay, CRD; contributing investigators are Dr. Harry A. Lipsitt, WSU, and Dr. Melvin R. Jackson and Dr. John A. Sutliff, CRD.

6.2 Personnel Qualifications

Bernard P. Bewlay

GE Corporate Research and Development

Education: BA, MA, and DPhil, Metallurgy and Materials Science, Oxford University.

Experience: Prior to joining GE Corporate Research and Development in 1989, Dr. Bewlay worked as a principal research scientist with Rolls Royce plc, United Kingdom. He is currently a metallurgist in the Physical Metallurgy Laboratory. He is the principal investigator on the program, "High Temperature Eutectic Microcomposites," presently sponsored by AFOSR. He has specialized in processing of high-temperature reactive materials, including both conventional refractory metals, such as tungsten, and advanced intermetallic-based composites. His most recent publications are on directional solidification of high-temperature in-situ composites and the fundamentals of the manufacture and application of tungsten lamp wire.

Dr. Bewlay is a member of the American Society for Materials, the Materials Research Society, and the Institute of Materials. He is the author or co-author of 42 published papers and articles, and holds 4 U.S. patents. He was the recipient of the 1991 ASM Alfred H. Geisler award.

Harry A. Lipsitt

Wright State University

Education: BS, Metallurgical Engineering, Michigan State College; MS and PhD, Metallurgical Engineering, Carnegie Institute of Technology (now Carnegie Mellon University).

Experience: Dr. Lipsitt joined Wright State University in 1986 as Professor of Materials Science and Engineering. From 1956-75 he was with the Aerospace Research Laboratories at Wright-Patterson AFB, ex-

cept for periods as Visiting Scientist at the University of Cambridge, UK (1963-64), and as Liaison Scientist at the Office of Naval Research, London, UK (1967-69). From 1975-86 he served as a Group Leader/Senior Scientist for High Temperature Materials at the AFWAL Materials Laboratory, WPAFB.

Dr. Lipsitt is a member of the Materials Research Society and American Institute of Mining, Metallurgical, and Petroleum Engineers. He has authored more than 90 publications on structure-property relations in metals and ceramics. His current research interests focus on high-temperature intermetallics as a class of structural materials.

Melvin R. Jackson

GE Corporate Research and Development

Education: BS, MS, and PhD Metallurgy and Materials Science, Lehigh University.

Experience: Dr. Jackson joined GE Research and Development in 1972. Prior to this he worked as a research metallurgist with the International Nickel Company. He is currently a materials scientist in the Physical Metallurgy Laboratory. He is the principal investigator of a program with Wright Laboratory entitled, "Alloy Development of In-Situ Intermetallic Composites." He is also the principal investigator on a project entitled, "Functionally Gradient Materials," currently sponsored by AFOSR. His research has concentrated on processing and properties in high-temperature systems, including phase equilibria and interdiffusion. His most heavily cited work deals with coating/substrate interdiffusion in Ni base materials, and the reactions between Ni systems and SiC. His current areas of research include behavior of refractory metals, intermetallic composites, functionally graded materials, and coatings.

Dr. Jackson is a member of the American Institute of Mining, Metallurgical, and Petroleum Engineers, the Materials Research Society, and the Microbeam Analysis Society. He is the author or co-author of 77 published papers and articles, and holds 48 U.S. patents. He was co-editor of the book *Alloying*, which was published in 1988 by ASM International.

John A. Sutliff

GE Corporate Research and Development

Education: BS and MEng., Cornell University; PhD, Materials Science and Engineering, Lehigh University.

Experience: Dr. Sutliff joined GE Corporate Research and Development in 1990 and is currently a materials scientist with the Materials Characterization Laboratory. His research interests include the study of structure-processing-property relations using electron microscopy, diffraction, and microchemical analysis. He has been heavily involved in the development of the EBSP technique for local texture measurement. His

most heavily cited work deals with phase stability, texture, and processing effects in Ti-based materials. His current research interests include texture-property relationships in Ti alloys and high-temperature composites.

Dr. Sutliff is a member of the American Institute of Mining, Metallurgical, and Petroleum Engineers, and the Electron Microscopy Society of America. He is the author or co-author of 40 published papers and articles. He was the recipient of the 1994 GE Aircraft Engines Badger award for his work on the relationship between texture and fatigue failures in Ti-6242.

7. Acknowledgments

This research was funded by AFOSR under contract #F49620-93-C-0007. The contract was monitored by Dr. Alan H. Rosenstein and Capt. Charles H. Ward. The authors are very grateful to AFOSR for this support. The authors would like to thank D.J. Dalpe for the directional solidification, C. Canestraro for the tensile testing, W.J. Reeder and P. McDermott for the fracture toughness measurements, and L.A. Peluso for the microprobe analyses. The authors

are also grateful to Drs. M.G. Mendiratta and P.R. Subramanian, UES, Dayton, OH, Dr. D.M. Dimiduk, AFWL, and Dr. D.L. Davidson, SouthWest Research Institute, for their very helpful discussion of the results. The authors would also like to acknowledge the collaboration of Dr. J.D. Rigney in the examination of the effect of test temperature on the fracture behavior of binary Nb-Si and ternary Nb-Ti-Si in-situ composites.